INFORMATION TO USERS

This manuscript has been reproduced from the microfilm master. UMI films the text directly from the original or copy submitted. Thus, some thesis and dissertation copies are in typewriter face, while others may be from any type of computer printer.

The quality of this reproduction is dependent upon the quality of the copy submitted. Broken or indistinct print, colored or poor quality illustrations and photographs, print bleedthrough, substandard margins, and improper alignment can adversely affect reproduction.

In the unlikely event that the author did not send UMI a complete manuscript and there are missing pages, these will be noted. Also, if unauthorized copyright material had to be removed, a note will indicate the deletion.

Oversize materials (e.g., maps, drawings, charts) are reproduced by sectioning the original, beginning at the upper left-hand corner and continuing from left to right in equal sections with small overlaps.

Photographs included in the original manuscript have been reproduced xerographically in this copy. Higher quality 6" x 9" black and white photographic prints are available for any photographs or illustrations appearing in this copy for an additional charge. Contact UMI directly to order.

Bell & Howell Information and Learning
300 North Zeeb Road, Ann Arbor, MI 48106-1346 USA

UMI®
800-521-0600

Fast All-Digital Carrier Synchronization Techniques for Linear Modulation Formats

Nestor Caouras

A thesis
in
The Department
of
Electrical and Computer Engineering

Presented in Partial Fulfillment of the Requirements
For the Degree of Master of Applied Science at
Concordia University
Montréal, Québec, Canada

April 2000

Abstract

Fast All-Digital Carrier Synchronization Techniques for Linear Modulation Formats

Nestor Caouras

This thesis studies fast, independent, low complexity, all-digital data-aided (DA) feedforward (FF) and decision-directed (DD) feedback (FB) carrier recovery (CR) techniques based on oversampling, suitable for linear modulation schemes (M-ary phase-shift-keying (M-PSK) and M-ary quadrature amplitude modulation (M-QAM)). Carrier synchronization is studied because, in passband communications, carrier phase and frequency offsets, due to modem oscillator discrepancies and distances between the users, corrupt the received data and must be removed for proper data decisions. The proposed techniques are evaluated in an additive white Gaussian noise (AWGN), non-multipath, point-to-multipoint burst-mode system.

Oversampling of a short preamble is introduced to reduce the required overhead for the FF techniques while still maintaining low hardware complexity, modularity, and a minimal number of different system clocks.

The DA FF phase estimation technique is unbiased and shown to perform as well as an equivalent efficient single-sample-per-symbol estimator achieving the Cramér-Rao lower bound (CRLB). The bit-error-rate (BER) degradation agrees with the

predicted one with, at most, an extra $0.1dB$ loss for a practical implementation in field programmable gate array (FPGA) technology.

The autocorrelation-based DA FF frequency estimator, although unbiased, does not achieve the CRLB for large window sizes. Nonetheless, it is able to produce coarse estimates with low hardware resource utilization. Increasing the correlation distance can produce at least a decade improvement in the variance.

The DD FB algorithm studied is an all-digital phase-locked loop (ADPLL). When oversampled, it performs just as well as an equivalent analog phase-locked loop (PLL) relative to BER degradation, variance, and transfer function characteristic. The ADPLL is stable and displays a wide tracking range, up to half of the sampling rate.

Key words: carrier recovery, feedforward and feedback synchronization, ADPLL.

I dedicate this work to my parents.

«γνῶθι σαὐτόν» - *Σωκράτης*
("know thyself" - *Socrates*)

Acknowledgements

I would like to express my deepest and most sincere gratitude toward my supervisor, Dr. Tho Le-Ngoc, for proposing this research topic to me and always providing useful feedback.

I would also like to acknowledge the financial support offered by the Canadian Institute for Telecommunications Research (CITR) and S.R.Telecom. Inc. (Montréal). A special thanks goes to S.R.Telecom. Inc., for lending us some of their equipment and also designing the FPGA test bed for the practical measurements.

My family deserves a great deal of thanks for their intangible and undying support throughout the course of my studies, graduate and other. I have but the utmost respect for them, and am forever indebted to them. I owe them my sanity.

Contents

List of Figures

List of Symbols

k, m, n, p	integer dummy variables
M-ary or M	modulation order
U	number of users in communication system architecture
R	number of data symbols in a burst
W	number of synchronization preamble symbols in a burst
K	oversampling factor
N	number of preamble samples
L	correlation distance in number of samples
I	in-phase channel
Q	quadrature channel
ℓ	start point of the ℓ^{th} burst
T_{sym}	symbol interval
f_{sym}	symbol rate
T_{sa}	sampling interval
f_{sa}	sampling rate
$G_T(\omega)$	frequency response of transmitter pulse-shaping filter
$g_T(t)$	time-domain impulse response of transmitter pulse-shaping filter
$G_R(\omega)$	frequency response of receiver pulse-shaping filter
$g_R(t)$	time-domain impulse response of receiver pulse-shaping filter
$G_N(\omega)$	combined frequency response of $G_T(\omega)$ and $G_R(\omega)$
$g_N(t)$	combined time-domain impulse response of $g_T(t)$ and $g_R(t)$
α	raised-cosine pulse roll-off factor (system model)or arbitrary function variable (ADPLL)
β	arbitrary function variable (ADPLL)
ω_c	passband carrier frequency
$\theta_T(t)$	transmitter oscillator initial phase
$\theta_R(t)$	receiver oscillator initial phase

$\theta_{off}(t)$	time-varying carrier phase error
θ_{off}	constant carrier phase error
$\widehat{\theta_{off}}$	estimate of θ_{off}
θ'_{off}	redefinition of θ_{off}
$\widehat{\theta'_{off}}$	estimate of θ'_{off}
θ_n	instantaneous phase offset
δ	degradation of phase estimation
ω_{off}	constant carrier frequency offset
$\widehat{\omega_{off}}$	estimate of ω_{off}
Δf	constant carrier frequency offset
$\widehat{\Delta f}$	estimate of Δf
a_k	complex symbol k (from arbitrary signal set
$\{a_k\}$	complex symbol sequence
$u(t)$	band-limited complex waveform at output of transmitter pulse-shaping filter
$w(t)$	AWGN complex stochastic process
$w_I(t)$	real part of $w(t)$
$w_Q(t)$	imaginary part of $w(t)$
$v(t)$	filtered noise $w(t)$ at the output of $g_R(t)$
$v_I(t)$	real part of $v(t)$
$v_Q(t)$	imaginary part of $v(t)$
$r(t)$	received signal (complex envelope) at the demodulator
$y(t)$	received signal at the output of $G_R(\omega)$
$v(nT_{sa})$	sampled version of $v(t)$
$y(nT_{sa})$	sampled version of $y(t)$
$z(nT_{sa})$	$y(nT_{sa})$ multiplied by the complex conjugate of preamble symbols
$b(nT_{sa})$	noise-free component of $z(nT_{sa})$
$\gamma(nT_{sa})$	noise component of $z(nT_{sa})$
z_n	shorthand notation for $z(nT_{sa})$
z'_n	redefinition of z_n
x_n	real part of z_n
y_n	imaginary part of z_n
s_n	signal sample
γ_n	shorthand notation for $\gamma(nT_{sa})$
γ_{In}	real part of $\gamma(nT_{sa})$

γ_{Qn}	imaginary part of $\gamma(nT_{sa})$
$S_{w_I}(\omega)$	power spectral density of $w_I(t)$
$S_{w_Q}(\omega)$	power spectral density of $w_Q(t)$
$S_{v_I}(\omega)$	power spectral density of $v_I(t)$
$S_{v_Q}(\omega)$	power spectral density of $v_Q(t)$
$R_{v_I}(\tau)$	autocorrelation function of $v_I(t)$
$R_{v_Q}(\tau)$	autocorrelation function of $v_Q(t)$
$R_{\gamma_Q}(n)$	autocorrelation function of γ_{Q_n}
E_s	average symbol energy
E_s/N_0	symbol-energy-to-noise ratio
E_b/N_0	bit-energy-to-noise ratio
σ_w^2	variance of $w_I(t)$ and $w_Q(t)$
σ_Q^2	variance of quadrature channel
$\sigma_{channel}^2$	variance of $w_I(t)$ and $w_Q(t)$
$N_0/2$	double-sided power spectral density of AWGN
$H_N(n)$	cumulative pulse-shaping impulse response at sample n within a burst's preamble
B	real constant, approximation for $H_N(n)$
χ_n	sub-term under summation of N_ρ'
C_n	random variable for magnitude of z_n
ϵ_n	random variable for phasee of z_n
BER_0	theoretical bit-error-rate for QPSK, 4QAM
D	bit-error-rate degradation
$P(w;\sigma^2)$	conditional BER associated with synchronization error w
w	synchronization error
σ^2	variance associated with $P(w;\sigma^2)$
σ_0^2	variance of noise for theoretical BER_0
$\phi_i(\cdot)$	input phase to PLL or ADPLL
$\phi_o(\cdot)$	VCO/NCO output phase
$\phi_e(\cdot)$	phase error at PLL or ADPLL phase detector output
K_d	phase error detector gain
K_v	open-loop dc gain
$F(s)$	Laplace-transform of analog loop filter transfer function
$F(z)$	z-transform of digital loop filter transfer function
$G(s)$	Laplace-transform of VCO transfer function

$G(z)$	z-transform of NCO transfer function
$H_c(s)$	Laplace-domain transfer function of analog PLL
$H(z)$	z-domain transfer function of ADPLL
$H_c(s)$	Laplace-domain transfer function of analog PLL
$H(z)$	z-domain transfer function of ADPLL
$H_c(j\omega)$	frequency response of analog PLL
$H(exp(j\omega T_{sym}))$	frequency response of ADPLLtransfer function
$N(z)$	z-domain numerator polynomial of $H(z)$
$D(z)$	z-domain denominator polynomial of $H(z)$
$N_e(z)$	z-domain numerator polynomial of $1 - H(z)$
γ_d	direct-path gain of loop filter
γ_f	integrator-path gain of loop filter
$\sigma^2_{\phi_e}$	ADPLL steady-state phase error variance
	(loop noise variance or tracking error variance)
B_L	loop bandwidth of ADPLL
$B_L(analog)$	loop bandwidth of analog PLL
ζ	damping factor
λ_ℓ	generic sample statistic
λ'_ℓ	redefined sample statistic for phase estimator
ξ	dummy random variable
$\hat{\xi}$	estimate of ξ
$A,\ F,\ J$	arbitrary constants
Y	dummy variable
τ	generic autocorrelation distance variable
ω	frequency variable
z	z-transform variable
z^{-1}	unit delay
z^{-L}	L-unit delay
$E[\cdot]$	expectation operator
$E_{\underline{a}}[\cdot]$	expectation operator over sequence $\underline{a}$
$\Re$	takes the real part of a complex quantity
$\Im$	takes the imaginary part of a complex quantity
$Q(x)$	Marcum's Q function
$*$	conjugation operator
$\star$	convolution operator

List of Acronyms

ADC	Analog-to-Digital Converter
ADPLL	All-Digital Phase-Locked Loop
ASIC	Application Specific Integrated Circuit
AWGN	Additive White Gaussian Noise
BWA	Broadband Wireless Access
Ch.	Chapter
CLB	Configurable Logic Block (Xilinx)
CORDIC	COordinate Rotation DIgital Computer
CR	Carrier Recovery
DA	Data-Aided
DAC	Digital-to-Analog Converter
DAVIC	Digital Audio VIdeo Council
dB	decibel
DD	Decision-Directed
DPLL	Digital Phase-Locked Loop
DSP	Digital Signal Processing
FB	FeedBack
FF	FeedForward
FPGA	Field-Programmable Gate-Array
GHz	Gigahertz
GSM	Global Standard for Mobile
Hz	Hertz
IF	Intermediate Frequency
IS-136	Interim Standard (EIA) 136
kHz	kilohertz
LMCS	Local Multipoint Communication System
LMDS	Local Multipoint Distribution System

LOS	Line-of-Sight
LUT	Look-Up Table
Mbps	Megabits per second
MHz	Megahertz
ML	Maximum Likelihood
modem	MOdulator/DEModulator
NCO	Numerically-Controlled Oscillator
NDA	Non-Data-Aided, Non-Decision-Directed
OQPSK	Offset Quadrature Phase-Shift-Keying
pdf	Probability Density Function
PLL	Phase-Locked Loop
PMP	Point-to-Multipoint
psd	Power Spectral Density
PSK	Phase-Shift-Keying
QAM	Quadrature-Amplitude Modulation
QPSK	Quadrature Phase-Shift-Keying
rad	radian
ROM	Read-Only Memory
Sec.	Section
TDMA	Time-Division Multiple Access
VCO	Voltage-Controlled Oscillator
VHDL	VHSIC Hardware Description Language
VHSIC	Very High-Speed Integrated Circuit
VLSI	Very Large Scale Integration
VSAT	Very Small Aperture Terminal
xDSL	different types of Digital Subscriber Lines

Chapter 1

Introduction

1.1 Motivation for Research

In modern digital communications, proper transceiver synchronization between the communicating parties is crucial for reliable data transfer. Applications, such as time division multiple access (TDMA) systems, cable modems (i.e. DAVIC), digital subscriber lines (xDSL), wireline and wireless line-of-sight (LOS) point-to-multipoint (PMP) architectures, and VSAT terminals, demand higher transmission rates while simultaneously facing bandwidth restrictions. Thus, they mandate the usage of higher-order passband modulation schemes in the upper frequency bands, e.g., 2 GHz to 42 GHz [1].

With passband modulation signaling arise new challenges: carrier phase and frequency offsets, which must be compensated for error-free data reception. Hence, the emerging applications prescribe the use of a burst-modem, whose different tasks include symbol-timing recovery (STR) and carrier recovery (CR), the latter being the sole interest of this work. STR must determine the optimal symbol sampling instants before performing any data decisions. Research of STR, however, is a subtopic in itself and is best left to a separate study [2]. On the other hand, CR must estimate

and remove from burst to burst the carrier offsets due to channel delays (translated in terms of a phase offset) and frequency errors.

The researcher must also balance the estimator's effectiveness with its complexity without severely compromising the system's efficiency or abuse hardware resource utilization. Coupled with today's ever growing low power consumption requirements and the need for system reconfigurability, the quest for simple, low complexity structures become as dominant an issue as the development of the techniques themselves.

To harmonize the trade-offs of CR, this research examines all-digital, low complexity coherent carrier phase estimation techniques, as well as frequency estimation algorithms, both of the data-aided (DA) feedforward (FF) type, which operate on a preamble of known symbols[1]. The proposed schemes are ideal for short burst systems (down to as low as one hundred symbols per burst) since the estimates are obtained in a single shot. The techniques in question marginally affect the system's efficiency by requiring only a short preamble. Coherent carrier phase recovery concerns itself with accurately estimating the carrier phase offset at the demodulator, a requirement for burst-mode systems for which the phase differs between received bursts. Coherent demodulation also provides a $1dB$ to $3dB$ power advantage over non-coherent methods, and is commonly employed in practice [3, Sec. 3.9 & Sec. 7.5].

Oversampling forms the basis of these techniques with the goal of reducing the burst's overhead to maximize the systems' capacity. At the same time, reducing the number of different clock domains in the transceivers minimizes the hardware complexity.

The proposed methods are independent of one another, making each technique

[1] Because of oversampling, the data-aided feedforward carrier recovery algorithms do not require perfect knowledge of the symbol-timing epoch during estimation. Chapters 2 and 3 detail these points further.

modular and easily integrable into present and future digital systems. Digital implementations offer many advantages over analog, notably

1. higher immunity to noise and voltage drifts,
2. insensitivity to component aging (of the transmit and receive oscillators, for instance),
3. higher processing speeds,
4. resource sharing,
5. implementation of complicated mathematical functions, including memory devices for storage of data intended for later processing.

For these reasons, the trend toward digital has dominated the past fifteen years of communication systems design, and has also propelled the study of the digital techniques presented in this thesis.

In addition to the FF schemes, an all-digital decision-directed (DD) feedback (FB) technique for tracking residual carrier frequency offsets is also considered[2]. The feedback algorithm also applies to long-burst and continuous-mode transmissions.

1.2 Survey and Classification of Carrier Recovery Algorithms

The vast number of carrier recovery estimators may be broadly categorized as either feedforward (FF) or feedback (FB) schemes. Figure 1.1 suggests one possible classification of existing techniques. Although each class can be implemented by

[2]The proposed DA FF frequency estimator is capable of providing only a coarse estimate of the frequency error. A supplemental algorithm is required to refine the frequency estimate and the DD FB satisfies this requirement.

analog or digital means, digital is the only interest here because of its advantages described in the previous section.

FF, or open-loop, estimators possess no feedback and, consequently, tend to be very well suited for short-burst operation (as low as one hundred symbols). They possess short and known acquisition times and avoid hangup complications faced by their closed-loop counterparts [4]. Hangup is a phenomenon innate in FB topologies causing them to drift aimlessly for significant periods of time before converging to a stable operating point. Occasionally, this equilibrium state differs from the true steady-state point, and subjects the system to the false lock phenomenon. The leading drawback of all FF estimators, however, lies in their inability to track time-varying offsets, seeing how each estimate remains fixed until the FF algorithm is engaged anew.

On the other hand, closed-loop systems generally experience long acquisition times and may suffer from hangup. Nevertheless, they extremely effective at tracking time-varying parameters since they continuously update and correct the error metric. Long-burst and continuous-mode systems employ feedback strategies, where the accumulated effects of time-varying phase and frequency offsets are intolerable. FB techniques are very well suited for analog and digital topologies [5, 6], whereas FF structures can only be implemented digitally owing to the complicated mathematical functions they encompass, for instance, an arctangent function [7].

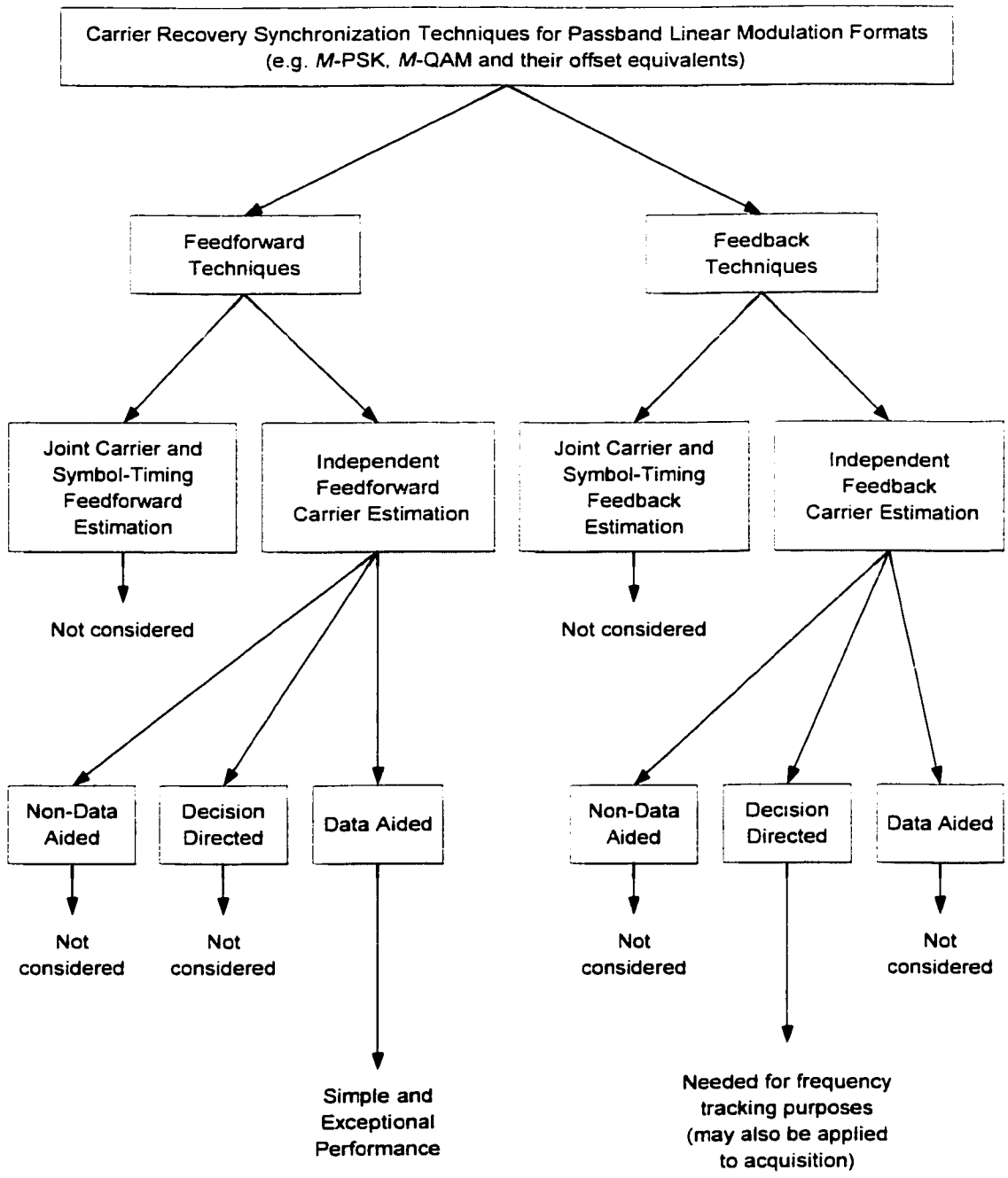

Figure 1.1: Classification of Estimation Techniques.

This thesis does not present an extensive survey of previous CR techniques since many authors have already covered this topic in great detail. The interested reader

is referred to the comprehensive texts by Gardner [7, 8] and the more recent book by Meyr, Moeneclaey, and Fechtel [9], both of which chronicle various techniques derived from maximum-likelihood (ML) theory and approximations thereof. They also discuss implementation structures from theoretical and practical viewpoints. Franks presents a tutorial review of carrier and symbol-timing synchronization in [10]. Going into the particulars, the recent paper by Morelli and Mengali surveys a vast collection of digital FF frequency estimators of the past fifteen years for M-ary phase-shift-keying (M-PSK) modulation, including autocorrelation and spectral-based techniques. Gardner's "bible" on phase-locked loops [4] presents substantial material in the analysis of analog FB techniques, with Lindsey's and Chie's paper [6] complementing Gardner's book for digital PLL's (DPLL's). An all-digital PLL is documented in [5]. A myriad of other techniques have been reported in the literature but their treatment is omitted here. The reader is encouraged to consult the additional references embodied within the indicated works.

Pursuing the classification of figure 1.1, under the groups of FF and FB estimators stem joint and independent FF and FB strategies. Joint estimation involves the optimization of the ML or maximum a posteriori (MAP) rules with respect to two or more parameters [11, 12]. For carrier recovery, maximization is performed simultaneously over phase and frequency offsets, while other scenarios may require the symbol timing as a third variable. Optimization of joint estimation is generally more difficult and do not result in isolated structures. Nonetheless, they typically outperform independent estimators [13, Sec. 6.4]. This research, however, seeks independent estimators. Therefore, joint estimation is ruled out. STR also lies outside the scope of this work.

In contrast to joint estimation, independent ones maximize the decision criterion over one parameter while treating the others as unwanted. These techniques

introduce added performance degradation, but warrant more modular synchronization structures independent of each other. This is very desirable for reconfigurable systems where system components may be changed on the fly, depending on the operating environment.

Three types of joint and independent estimation exist:

1. Data-aided (DA) techniques exploit the knowledge of a known data pattern (called a preamble) to aid data recovery. Because preambles contain no useful user information, they decrease the overall system capacity and, as a result, should be kept as short possible. In modern systems, a unique frame synchronization pattern is almost always necessary for proper detection of the burst's start position. With appropriate encoding, the same frame synchronization preamble may also be employed for CR, which, in turn, maximizes the burst's efficiency [14, 15]. In addition to maximizing the data throughput, burst-mode systems must rapidly acquire good offset estimates. DA techniques exploit prior knowledge of the preamble symbols at the receiver, and thus, provide exceptional performance even at low signal-to-noise ratios (less than $8dB$). For these reasons, DA FF techniques are studied.

2. Decision-directed (DD) methods resemble DA techniques except that symbol decisions are substituted in place of the known preamble at the receiver. Under moderate ($8dB$ to $15dB$) and high signal-to-noise ratios (greater than $15dB$) decision errors are rare and DD techniques perform just as well as DA schemes. Low signal-to-noise ratios (less than $8dB$), however, engender more frequent decision errors and DD performance might deviate significantly from the DA case. Nevertheless, DD techniques operate without a preamble and, hence, do not reduce system efficiency.

3. Non-data-aided or non-decision aided (NDA) methods require no preamble and

use the data itself instead of decisions for estimation. Hence, system capacity is always maximized for these techniques. NDA methods average the effects of the modulation sequence in order to maximize the ML function. The received signal must be processed by a non-linear function to remove the effect of modulation, so they result in more complex structures. At high signal-to-noise ratios (greater than $15dB$), NDA schemes perform similar to DA and DD structures, but avoid the use of a preamble and symbol decisions. However, at lower signal-to-noise ratios (approximately less than $8dB$), they suffer from threshold effects. The threshold represents the signal-to-noise ratio below which large estimation errors start to occur.

The present study examines independent, low complexity, all-digital DA FF carrier phase and frequency recovery techniques suitable for linear modulation schemes such as M-ary phase-shift-keying (M-PSK), M-ary quadrature amplitude modulation (M-QAM) and their offset equivalents. Their short acquisition times make them ideal for short-burst operation, where the overhead must be minimal. NDA techniques are not examined because they do not offer low complexity solutions, while the preamble-less nature of their bursts cause them to be less easily detected in practical setups. DD FF algorithms are not considered either since we would like to use techniques that can provide accurate enough initial estimates at virtually all signal-to-noise ratios. Hence, DA FF techniques are the only FF techniques of interest.

NDA FB and DA FB techniques are not examined since the former results in high complexity structures, whereas the latter further increases the preamble. A digital DD FB algorithm is, therefore, the optimal choice. Even if its performance is less satisfactory at low signal-to-noise ratios compared to DA techniques, it results in simple architectures, and does not increase the preamble, thus maintaining the overall system efficiency. The sought after FB technique is introduced to counter the effects

of a residual frequency offset leftover from a coarse feedforward offset correction[3]. The FB technique is independent of the FF algorithms so that we remain in line with our independence requirement. The closed-loop technique is also applicable to longer-burst and continuous-mode systems.

All techniques are suitable for digital implementation in field-programmable gate-arrays (FPGAs) or very-large-scale-integration (VLSI) application specific integrated circuits (ASICs).

1.3 Communication System Topology, Requirements and Assumptions

The considered communication system is similar to a time-division-multiplexing/time-division multiple-access (TDM/TDMA) topology, as depicted in figure 1.2. U users are allocated a continuous connection to a central station over a common channel, on which each user is permitted to transmit during prescribed time slots (bursts) using a bandwidth which is much higher than what is normally required by an individual user[4]. The intervals during which a user is allowed to transmit depend on the chosen capacity allocation scheme, but it is not necessary to have a fixed or ordered amount of slots between a given user's transmissions (thus the term dynamic capacity allocation). Capacity allocation techniques are not described here since they reside outside the scope of carrier recovery.

[3]The DA FF frequency offset that is presented is shown to provide coarse one-shot estimates of the frequency offset.

[4]The bandwidth is derived from the required link bit-rate (or symbol-rate) plus the anticipated frequency offset.

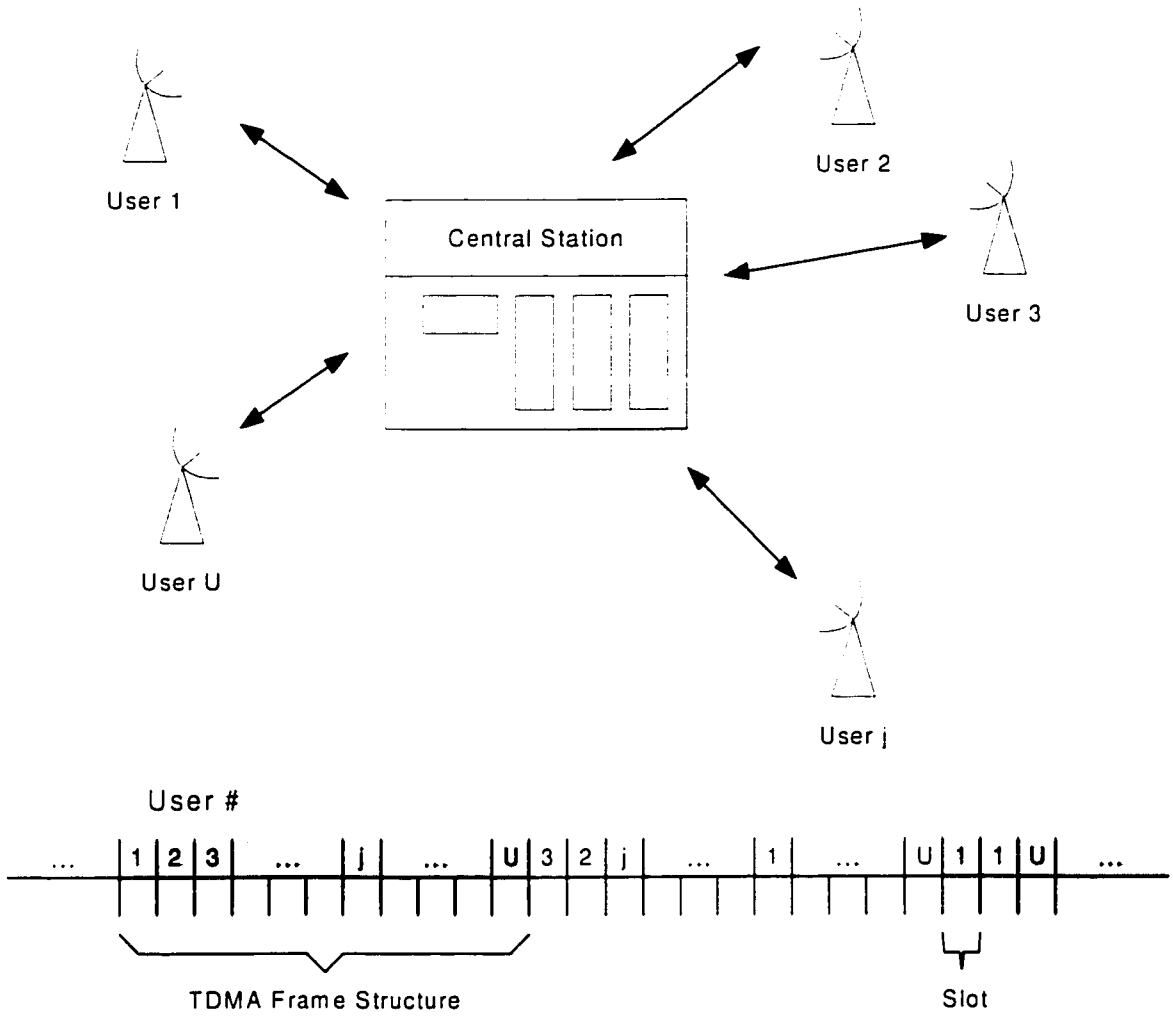

Figure 1.2: Burst-Mode Point-to-Multipoint Communication System.

The detailed description of a single communication link between two users (any user and the base station) is detailed in chapter 2. For now, the assumptions and requirements governing the communication model of figure 1.2 are stated next and justified where needed:

1. An additive white Gaussian noise (AWGN) linear channel with double-sided noise power spectral density (*psd*) of $N_0/2$ is assumed. There is no cross-channel interference, i.e., the in-phase and quadrature channels are independent and

possess identical stochastic properties (they are AWGN).

2. A non-multipath PMP burst-mode system is considered. In multipath fading, time-delayed multiple copies of a transmitted signal arrive at a given station, in addition to the direct transmission. This condition afflicts some types of fixed-user systems (such as BWA, LMCS/LMDS [1]) and mobile systems (such as digital mobile cellular, e.g., GSM, IS-95, IS-136 [14]) Multipath fading engenders severe amplitude dips in the frequency spectrum of the resulting received signal. It is not studied since it requires equalization or other solutions [13, Ch. 14]. It is left as a suggestion for future study. Instead, the burst-mode system of interest is modeled as TDM/TDMA with fixed central and user stations. This category includes most wireline topologies as well as wireless LOS architectures.

3. Linear modulation formats (M-PSK, M-QAM and their offset equivalents) are studied because their behavior through a linear channel is very well understood. Quadrature phase-shift keying (QPSK), equivalent to 4-level quadrature amplitude modulation (4QAM), and offset-QPSK (OQPSK) serve as case studies[5].

4. The carrier phase and frequency offsets are deterministic, unknown parameters. They are assumed slowly time-varying so that they may be considered constant throughout the entire duration of a short burst, or constant over a window of symbols in the case of longer bursts or continuous-mode transmission. Under this assumption, multipath fading and Doppler frequency shifts (due to relative motion between users) are immediately excluded since they produce time-varying offsets within the same burst.

[5]QPSK and 4QAM represent the same constellation even though they result from different modulation formats. The four possible symbols are located at the corners of the square constellation in the $\Re\Im$-plane. Throughout the text, QPSK and 4QAM are used but the reader should understand that they represent exactly the same information. They are denoted by QPSK/4QAM throughout the text.

5. The phase offsets arise solely because of the different geographic locations between the users, as well as the different startup phases of the up- and down-conversion oscillators.

6. The frequency offsets arise from oscillator imperfections (not Doppler frequency shifts).

7. The proposed estimation techniques are based on oversampling with the purpose of minimizing the preamble.

8. A free running oscillator is used as the sampling frequency, and is chosen as an integer multiple of the symbol frequency.

9. The techniques sought after should offer low complexity for minimal hardware utilization, and easy integration with other components of the digital system.

10. Perfect symbol timing is assumed or recovered a priori (using techniques derived from the maximum-likelihood (ML) principle [2, 7, 9], or more traditional ones, e.g., the Costas loop or the phase-locked loop [13, Ch. 6]).

11. The signal is band-limited and satisfies Nyquist's criterion for zero inter-symbol interference (ISI) (chapter 2 details this topic further). Band-limiting is required since all practical systems must restrict the amount of bandwidth they intend to use (square pulse shaping (infinite bandwidth) is not possible in practice).

12. Study of quantization effects on the proposed estimators is omitted since it represents a topic in itself and falls outside the scope of this dissertation.

1.4 Scope of Thesis

So far, the current chapter has established the importance of researching carrier synchronization techniques. This section previews the chapters to follow.

Chapters 2 through 4 present the carrier recovery techniques investigated for linear modulation schemes (M-PSK and M-QAM) and exemplified with quadrature phase-shift-keying (QPSK), offset-QPSK (OQPSK) and 4QAM. The first section of chapter 2 forms the theoretical substrate upon which the subsequent analysis is based. It describes the complex baseband signal model. The remainder of that chapter examines the proposed DA FF phase offset estimator and assesses its performance analytically, through simulations and practical measurements.

Chapter 3 focuses on a DA FF frequency offset estimator and reveals that the proposed technique performs poorly in environments with moderate to high noise. To counter this complication without increasing the preamble, a digital DD FB tracking loop is introduced in chapter 4, where it is analyzed using the z-transform technique.

The fifth chapter summarizes the global findings of this project and suggests future routes to extend the topics discussed herein.

Appendix A presents the details of the approximate analysis leading to the frequency offset estimator's second moment.

1.5 Contributions of Thesis

The following list describes the contributions of this thesis:

1. *Study of low complexity, all-digital, data-aided feedforward carrier phase and frequency offset estimation techniques based on oversampling.* Two DA FF techniques are presented, one for carrier phase error recovery based on averaging[6].

[6]The proposed phase recovery algorithm resembles an oversampled version of the Viterbi and Viterbi (V&V) technique [16].

and another for carrier frequency offset estimation based on the autocorrelation principle with adjustable correlation distance. It is demonstrated that both techniques can result in low complexity structures while providing acceptable performance.

2. *Study of oversampling on carrier estimation.* Due to the apparent absence in today's literature, the effect of oversampling on carrier recovery is examined in this thesis by means of theoretical, simulation and practical means of the FF algorithms.

3. *Presentation of an approximate variance analysis for small offsets and high signal-to-noise ratios.* In general, the carrier phase offsets are embedded non-linearly in the transmitted and received data. Band-limiting and oversampling introduce dependence in the received random observations, so that a closed-form solution of the estimators' moments is not possible. The thesis presents approximations under high signal-to-noise ratios and small offsets to simplify the performance analysis. The analysis techniques may also be applicable to other case studies not covered by this dissertation.

4. *Presentation and analysis of an all-digital DD FB loop using z-transform analysis.* The dissertation studies a second-order, all-digital phase-locked loop (ADPLL), a simple DD FB scheme, using the z-transform technique since much of the literature using this technique to analyze the loop is scattered or scarce. The chapter devoted to this topic attempts to unify the information pertaining to the ADPLL.

Chapter 2

Data-Aided Feedforward Phase Estimation Technique Employing Oversampling

The signal model referenced by all subsequent chapters of this thesis is presented in the first section of this chapter. Section 2.2 then presents the DA FF phase estimator algorithm, while section 2.3 assesses the technique's performance analytically. Section 2.4 employs simulations to the same end, and compares the results to the theory. BER simulations and measurements are also included. Finally, section 2.5 examines the estimator's implementation.

2.1 Background

2.1.1 Equivalent Complex Baseband Signal Model

This section details the theoretical background used throughout the thesis. Figure 2.1 illustrates the equivalent complex baseband signal model.

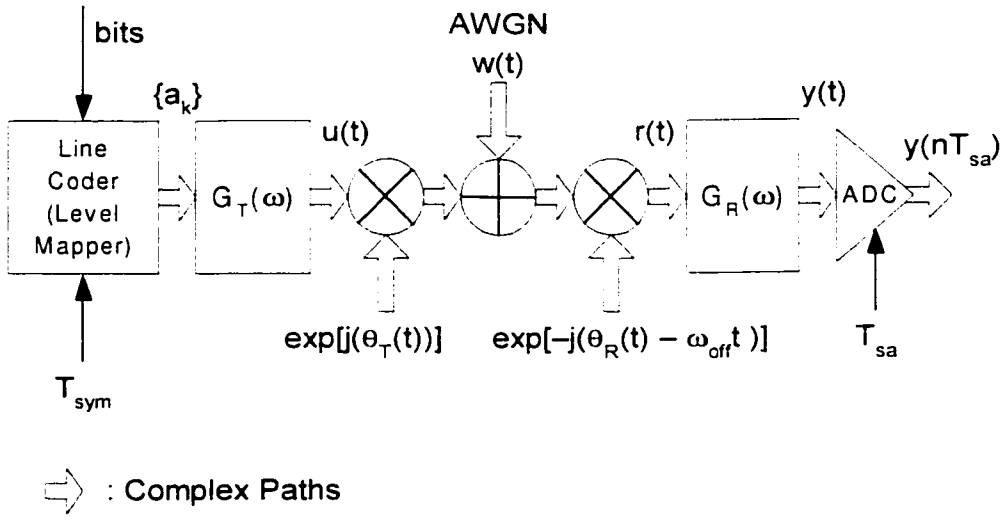

Figure 2.1: Equivalent Complex Baseband Signal Model.

The line coder maps a stream of user data bits into a sequence $\{a_k\}$ of R independent data symbols chosen from a complex signal set. To facilitate synchronization at the receiver, a known pattern W-symbols long is inserted at the start of the burst. To maximize system efficiency, W should be kept as small as possible [17]. The average symbol energy, E_s, is normalized to unity for convenience. The band-limited waveform $u(t)$ at the output of the transmitter pulse-shaping filter $G_T(\omega)$ is expressed as

$$u(t) = \sum_{k=\ell}^{\ell+W+R-1} a_k g_T(t - kT_{sym}) \tag{2.1}$$

where ℓ denotes the beginning of the ℓ^{th} burst in the TDMA frame, T_{sym} the symbol interval, and $g_T(t)$ the time-domain impulse response of $G_T(\omega)$. The band-limited signal $u(t)$ modulates a carrier centered at frequency ω_C before being transmitted over the communication link. In the receiver's down-conversion process, a residual frequency error, ω_{off}, perhaps a significant fraction of the symbol rate, creeps into

the received baseband signal and continuously rotates the demodulated data, engendering cycle slips, a situation where the "corrected" data falls in the wrong decision regions and, consequently, increases the BER. Frequency errors arise mainly from manufacturing discrepancies in the up- and down-conversion oscillators. In addition, the modulator and demodulator oscillators are not phase-synchronized because of unequal initial oscillator phases, denoted by $\theta_T(t)$ and $\theta_R(t)$ respectively.

For simplicity, the transmission link is assumed linear with a flat frequency response. The channel injects AWGN in the system, denoted by $w(t) = w_I(t) + jw_Q(t)$, whose in-phase ($w_I(t)$) and quadrature ($w_Q(t)$) components are independent, zero-mean, stationary random quantities with two-sided power spectral density (*psd*) given by

$$S_{w_I}(\omega) = S_{w_Q}(\omega) = \sigma_w^2 = N_0/2. \tag{2.2}$$

Accounting for the effects described in the previous paragraph, the complex envelope $r(t)$ presented to the receiver's pulse-shaping filter $G_R(\omega)$ may be expressed as

$$r(t) = u(t)\exp\{j\theta_T(t)\}\exp\{j[-\theta_R(t) + \omega_{off}t]\} + w(t) \tag{2.3}$$

where the signs are chosen arbitrarily.

In the equivalent baseband representation of figure 2.1 the carrier frequency ω_C does not appear due to the construction of the complex baseband model. Substituting the carrier phase error $\theta_{off}(t) = \theta_T(t) - \theta_R(t)$ into $r(t)$ yields

$$\begin{aligned} r(t) &= u(t)\exp\{j[\theta_T(t) - \theta_R(t) + \omega_{off}t]\} + w(t) && (2.4)\\ &= u(t)\exp\{j\theta_{off}(t) + j\omega_{off}t\} + w(t). && (2.5) \end{aligned}$$

For the present analysis, since the carrier errors are assumed slowly time-varying with respect to the symbol rate, they may be considered piecewise constant over

a window of symbols for long bursts (larger than one thousand symbols), or the entire burst if it is very short (as low as one hundred symbols). For this reason, $\theta_{off}(t) = \theta_{off}$, where θ_{off} is now an unknown but non-random constant phase error uniformly distributed in the interval $[-\pi, \pi]$.

The output of $G_R(\omega)$ is

$$\begin{aligned} y(t) &= [u(t)\exp\{j\theta_{off} + j\omega_{off}t\} + w(t)] \star g_R(t) && (2.6) \\ &= u(t)\exp\{j\theta_{off} + j\omega_{off}t\} \star g_R(t) + w(t) \star g_R(t) && (2.7) \end{aligned}$$

with $\star$ denoting the convolution operation, and $g_R(t)$, the time-domain impulse response of $G_R(\omega)$. Substituting $u(t)$ of (2.1) into (2.7) results in

$$y(t) = \sum_{k=\ell}^{\ell+W+R-1} a_k g_T(t - kT_{sym})\exp\{j(\theta_{off} + \omega_{off}t)\} \star g_R(t) + w(t) \star g_R(t). \quad (2.8)$$

If the phase error fluctuations occupy a small bandwidth with respect to the channel frequency response, i.e., the case of slowly time-varying carrier phase parameters, filtering and multiplication in (2.8) may be interchanged [9, Sec. 3.2]. Equation (2.8) then simplifies to

$$\begin{aligned} y(t) &= \sum_{k=\ell}^{\ell+W+R-1} a_k g_T(t - kT_{sym}) \star g_R(t)\exp\{j(\theta_{off} + \omega_{off}t)\} + w(t) \star g_R(t) \\ &= \sum_{k=\ell}^{\ell+W+R-1} a_k g_N(t - kT_{sym})\exp\{j(\theta_{off} + \omega_{off}t)\} + v(t). && (2.9) \end{aligned}$$

The expression $g_N(t) = g_T(t) \star g_R(t)$ defines the combined impulse response of the transmitter and receiver pulse-shaping filters, and $v(t) = v_I(t) + jv_Q(t)$ is simply the filtered noise at the output of $g_R(t)$. In band-limited systems it is customary to select pulse-shaping functions that satisfy Nyquist's first criterion to eliminate ISI at the optimum symbol sample, i.e., the maximum eye opening [13, Sec. 9.2.1]. The

most common type of zero-ISI filter is the raised-cosine pulse with a roll-off factor α ($0 \leq \alpha \leq 1$). Common expressions for the raised-cosine's impulse and frequency responses are given in (2.10) and (2.11), respectively, with $g_N(t)$ normalized to unity.

$$g_N(t) = \frac{\sin(\pi t/T_{sym})}{\pi t/T_{sym}} \frac{\cos(\alpha\pi t/T_{sym})}{1-(2\alpha\pi t/T_{sym})^2} \tag{2.10}$$

$$G_N(\omega) = \begin{cases} T_{sym}, & 0 \leq |\omega T_{sym}| < \pi(1-\alpha) \\ \dfrac{T_{sym}}{2}\left\{1-\sin\left[\dfrac{\omega T_{sym}-\pi}{2\alpha}\right]\right\}, & \pi(1-\alpha) \leq |\omega T_{sym}| < \pi(1+\alpha) \\ 0, & |\omega T_{sym}| \geq \pi(1+\alpha). \end{cases} \tag{2.11}$$

From matched filter theory, the pulse-shaping function is equally apportioned between the transmitter and the receiver, $G_T(\omega) = G_R^*(\omega)$ and $G_N(\omega) = G_T(\omega)G_R(\omega) = |G_T(\omega)|^2$ [17, Sec. 4.1.1]. We thus speak of root-raised-cosine filters. Under these provisions, the overall response remains Nyquist and signal detection is maximized for an AWGN channel.

By virtue of the previous discussion, the power spectral densities $S_{v_I}(\omega)$ and $S_{v_Q}(\omega)$ of the filtered noise components, with corresponding autocorrelation functions $R_{v_I}(\tau)$ and $R_{v_Q}(\tau)$, equal

$$S_{v_I}(\omega) = S_{v_Q}(\omega) = S_{w_I}(\omega)\,|G_R(\omega)|^2 = S_{w_Q}(\omega)\,|G_R(\omega)|^2 = \frac{N_0}{2}G_N(\omega) \tag{2.12}$$

$$R_{v_I}(\tau) = R_{v_Q}(\tau) = \frac{N_0}{2}\frac{\sin(\pi\tau/T_{sym})}{\pi\tau/T_{sym}}\frac{\cos(\alpha\pi\tau/T_{sym})}{1-(2\alpha\pi\tau/T_{sym})^2}. \tag{2.13}$$

The autocorrelation functions are real ($R_{v_I}^*(\tau) = R_{v_I}(\tau)$, $R_{v_Q}^*(\tau) = R_{v_Q}(\tau)$) and even-symmetric ($R_{v_I}(-\tau) = R_{v_I}(\tau)$, $R_{v_Q}(-\tau) = R_{v_Q}(\tau)$). Also, $\alpha = 0$ generates the famous "brick-wall" low-pass filter.

The previous discussion demonstrates that the filtered baseband noise is no longer delta-correlated, as noted in (2.12) and (2.13), except for sampling instants equal to

integer multiples p of the symbol period, i.e., $\tau = pT_{sym}$. However, the resulting noise, although colored, invariably remains Gaussian. In essence, any linear system preserves the Gaussian characteristic of the input random process as long as it was Gaussian to begin with [12, Sec. 3.3.3]. The estimation techniques presented later oversample the received baseband signal at rates higher than the symbol rate, so the effects of colored noise cannot be ignored in their performance evaluation.

In the last stage of the signal model (figure 2.1), an analog-to-digital converter (ADC) uniformly samples $y(t)$ at intervals nT_{sa}. Digital signal processing (DSP) techniques may be applied to the resulting samples in order to yield the parameter estimates. The uniform sampling rate, f_{sa}, is chosen as an integer multiple K of the symbol frequency, where $f_{sa} = 1/T_{sa} = Kf_{sym}$[1]. There is no need, however, to oversample the entire burst and obtain $(W+R)K$ samples since estimation considers but the preamble. Using the carrier estimates as its inputs, a complex rotator at the receiver corrects the payload symbols at rate f_{sym} without introducing ISI (since optimum timing is known, unless the matched filter mismatch due to the frequency offset it too great). The only prerequisite is a priori knowledge of the symbol-timing during correction, but only during data correction. The oversampled preamble at the matched filter output is given by

$$y(nT_{sa}) = \sum_{k=\ell}^{\ell+W+R-1} a_k g_N(nT_{sa} - kT_{sym}) \exp\{j(\theta_{off} + \omega_{off} nT_{sa})\} + v(nT_{sa})$$
$$n = \ell, \ell+1, \ldots, \ell+N-1; N = KW, W \ll R. \qquad (2.14)$$

Multiplying the first N samples associated with the preamble by the (sampled) complex conjugate of the known preamble sequence, $\{a_k^*\}$, $k = \ell, \ell+1, \cdots, \ell+W-1$,

[1] Under the equivalence condition between continuous and discrete-time systems, the matched filter and sampling processes may be interchanged without any loss of information, thus allowing the use of a digital matched filter. In fact, the samples $r(nT_{sa})$ represent sufficient statistics for estimation [9, Sec. 4.3].

removes the effect of the modulating sequence [18]. Letting $a_k a_k^* = 1$, where * denotes complex conjugation, the first N samples amount to

$$\begin{aligned} z(nT_{sa}) &= y(nT_{sa})a_k^* \\ & n = \ell, \ell+1, \ldots, \ell+N-1, N = KW, W \ll R \end{aligned} \tag{2.15}$$

or, in expanded form,

$$\begin{aligned} z(nT_{sa}) &= \sum_{k=\ell}^{\ell+W+R-1} g_N(nT_{sa} - kT_{sym}) \exp\{j(\theta_{off} + \omega_{off} nT_{sa})\} \\ &\quad + \gamma(nT_{sa}) \\ & n = \ell, \ell+1, \ldots, \ell+N-1, N = KW, W \ll R \end{aligned} \tag{2.16}$$

where each a_k^* is held constant for T_{sym} seconds, i.e., K sampling periods. The symbols $\{a_k\}$ may be chosen arbitrarily from the complex signal set, but the estimators at hand employ the same symbol. The resulting noise samples $\gamma(nT_{sa}) = v(nT_{sa})a_k^*$ are statistically equivalent to $v(nT_{sa})$ [18]. This result holds, for the a_k's represent known amplitude and phase variations, which affect all samples of $v(nT_{sa})$ in a known and similar fashion. Thus, their statistical properties are maintained. The noise-free component of (2.16) is given by

$$\begin{aligned} b(nT_{sa}) &= \sum_{k=\ell}^{\ell+W+R-1} g_N(nT_{sa} - kT_{sym}) \exp\{j(\theta_{off} + \omega_{off} nT_{sa})\} \\ & n = \ell, \ell+1, \ldots, \ell+N-1, W \ll R \end{aligned} \tag{2.17}$$

and depends on the carrier phase and frequency errors. Replacing $z(nT_{sa})$ by the shorthand notation z_n, and $\gamma(nT_{sa})$ by γ_n results in a more compact notation of

(2.16), i.e.,

$$z_n = \sum_{k=\ell}^{\ell+W+R-1} g_N(nT_{sa} - kT_{sym}) \exp\{j(\theta_{off} + \omega_{off} nT_{sa})\} + \gamma_n \qquad (2.18)$$
$$n = \ell, \ell+1, \ldots, \ell+N-1, N = KW, W \ll R.$$

From now on, the last line in (2.18) is omitted to alleviate the notation.

It is also important to note that the phase and frequency recovery preambles may be merged into a common one, that is, the same symbols may be simultaneously processed for phase and frequency offset estimation, seeing that the two techniques are independent of each other. This will become apparent when the FF techniques are studied.

2.1.2 Performance Measures

In order to judge an estimator's quality, two performance measures are examined [12, Sec. 2.4.2], namely,

- the mean, or expected value, of the estimate, and,
- the variance of the estimation error.

The Mean as a Performance Measure

When evaluating the mean, three cases are encountered:

1. The expected value equals the parameter being estimated, i.e.,

$$E\left[\hat{\xi}\right] = \xi \qquad (2.19)$$

for all ξ, where ξ is the non-random but unknown parameter, and $\hat{\xi}$ is its estimate. In this case, the estimate is unbiased.

2. The expected value differs from the parameter being estimated by a fixed and non-changing amount A, i.e.,

$$E\left[\hat{\xi}\right] = \xi + A. \tag{2.20}$$

In this case, the bias is known and equal to A. To transform $\hat{\xi}$ into an unbiased estimate, one simply subtracts the known bias from its expression, i.e.,

$$\hat{\xi}' = \hat{\xi} - A \tag{2.21}$$

so that the mean of the modified estimate equals

$$E\left[\hat{\xi}'\right] = \xi. \tag{2.22}$$

3. For the third case, the expected value of $\hat{\xi}$ differs from the true parameter by a variable quantity:

$$E\left[\hat{\xi}\right] = \xi + A(\xi). \tag{2.23}$$

$A(\xi)$ cannot be subtracted out as in the previous case since it depends on the parameter to be estimated. Therefore, it results in a variable bias.

The Variance as a Performance Measure

The second performance criterion is the variance of the estimation error, denoted by $\hat{\xi} - \xi$:

$$var\left[\hat{\xi}\right] = E\left[(\hat{\xi} - \xi)^2\right]. \tag{2.24}$$

The variance of $\hat{\xi}$ provides a measure of the estimate's spread about the parameter. If the estimator is unbiased, then the lower bound on its variance equals the Cramér-Rao lower bound (CRLB), which is an ideal performance reference for comparing the variance of any unbiased estimate. It represents the lower limit on the variance that cannot be outperformed by any unbiased estimator, and given by

$$var\left[\hat{\xi}\right] \geq \frac{-1}{E\left[\frac{\partial^2 \ln f_{\underline{z}}(\underline{z} \mid \xi)}{\partial \xi^2}\right]} \tag{2.25}$$

where $\frac{\partial^2 \ln f_{\underline{z}}(\underline{z} \mid \xi)}{\partial \xi^2}$ is the second order partial derivative of the conditional *pdf* of a sample observation vector $\underline{z}$, conditioned on the parameter ξ. It is assumed that the partial derivative exists and is absolutely integrable. An efficient estimate is one that satisfies the CRLB with equality [11, Sec. 5.5.1].

Clearly, an unbiased estimate does not guarantee a good estimate since its spread may be wide. Hence, a good estimate should exhibit both a small bias and a small variance, preferably achieving the CRLB. In this case, the estimate clusters closely about the parameter being estimated.

2.2 Presentation of Phase Offset Estimation Algorithm

In this section the phase offset estimator is derived from the complex preamble samples of (2.18). The proposed estimator averages N preamble observations with the intent of removing the influence of the noise. The argument of the resulting sum produces the sought after phase offset estimate. Let's define λ_ℓ as the sample mean

statistic:

$$\lambda_\ell = \frac{1}{N} \sum_{n=\ell}^{\ell+N-1} z_n. \tag{2.26}$$

Substituting (2.18) in λ_ℓ yields

$$\lambda_\ell = \frac{1}{N} \sum_{n=\ell}^{\ell+N-1} \left(\sum_{k=\ell}^{\ell+W+R-1} [g_N(nT_{sa} - kT_{sym}) \exp\{j(\theta_{off} + \omega_{off} nT_{sa})\}] + z_n \right). \tag{2.27}$$

Inspection of (2.27) in a noise-free environment reveals that θ_{off} is independent of the indices n and k and can be moved outside the summations. Further, the frequency offset is contained within a factor which depends on index n and can be moved outside the inner summation over k. λ_ℓ now reads as

$$\lambda_\ell = \exp\{j\theta_{off}\} \frac{1}{N} \sum_{n=\ell}^{\ell+N-1} \exp\{j\omega_{off} nT_{sa}\} \sum_{k=\ell}^{\ell+W+R-1} g_N(nT_{sa} - kT_{sym}). \tag{2.28}$$

The last summation in (2.28) depends purely on n since each burst is of fixed length. Defining $H_N(n)$ as

$$H_N(n) = \sum_{k=\ell}^{\ell+W+R-1} g_N(nT_{sa} - kT_{sym}) \tag{2.29}$$

conveniently simplifies the notation in (2.28) to

$$\lambda_\ell = \exp\{j\theta_{off}\} \frac{1}{N} \sum_{n=\ell}^{\ell+N-1} \exp\{j\omega_{off} nT_{sa}\} H_N(n) \tag{2.30}$$

The overhead sequence is composed entirely of a single symbol, hence, $H_N(n)$ is approximately constant over the estimation window of interest. With this type of preamble, the ISI fluctuations are minimal, although slightly more pronounced when the matched filter roll-off approaches zero. Under these premises,

$$H_N(n) \approx B \tag{2.31}$$

where B is a real constant close to unity, given that the overall pulse-shaping impulse response is normalized to unity. λ_ℓ degenerates to

$$\lambda_\ell = \exp\{j\theta_{off}\}\frac{1}{N}\sum_{n=\ell}^{\ell+N-1}\exp\{j\omega_{off}nT_{sa}\}B \tag{2.32}$$

$$= \frac{B}{N}\exp\{j\theta_{off}\}\left(\frac{\exp\{j\omega_{off}T_{sa}\ell\}-\exp\{j\omega_{off}T_{sa}(\ell+N)\}}{1-\exp\{j\omega_{off}T_{sa}\}}\right) \tag{2.33}$$

$$= \frac{B}{N}\exp\{j\theta_{off}\}\cdot \left(\frac{\exp\{j\omega_{off}T_{sa}\ell\}\left(\exp\{-j\omega_{off}T_{sa}N/2\}-\exp\{j\omega_{off}T_{sa}N/2\}\right)}{\exp\{j\omega_{off}T_{sa}/2\}\left(\exp(-j\omega_{off}T_{sa}/2)-\exp(j\omega_{off}T_{sa}/2)\right)}\right) \tag{2.34}$$

$$= \frac{B}{N}\exp\{j\theta_{off}\}\cdot \left(\frac{\exp\{j\omega_{off}T_{sa}(\ell+(N-1)/2)\}\{-\sin(\omega_{off}T_{sa}N/2)\}}{\exp\{j\omega_{off}T_{sa}/2\}(-\sin(\omega_{off}T_{sa}2))}\right). \tag{2.35}$$

Taking the argument of λ_ℓ, and realizing that only $exp\{j\theta_{off}\}$ exhibits a non-zero argument, leads to the phase offset estimate $\widehat{\theta_{off}}$, that is,

$$\widehat{\theta_{off}} = \arg\{\lambda_\ell\} \tag{2.36}$$

$$= \theta_{off} + \arg\left(\frac{\exp\{j\omega_{off}T_{sa}(\ell+(N-1)/2)\}\{-\sin(\omega_{off}T_{sa}N/2)\}}{\exp\{j\omega_{off}T_{sa}/2\}(-\sin(\omega_{off}T_{sa}2))}\right) \tag{2.37}$$

$$= \theta_{off} + \left(\frac{\ell+N-1}{2}\right)\omega_{off}T_{sa}. \tag{2.38}$$

Accordingly, in the absence of noise, $\widehat{\theta_{off}}$ of (2.38) returns the phase at the middle of the N-sample observation window, not the phase at the beginning. $\widehat{\theta_{off}}$ contains the contribution of θ_{off}, but also depends on ω_{off}, which is not desired since we seek independent estimators. Remapping $\widehat{\theta_{off}}$ to cancel its dependence on ω_{off} is now examined.

The instantaneous phase offset θ_n obeys the linear relationship defined by

$$\theta_n = \theta_{off} + \omega_{off} T_{sa} n. \tag{2.39}$$

The frequency offset is symmetrically distributed about the estimation window's center, the only point displaying a zero frequency error. Rife and Boorstyn reported this behavior when deriving the Cramér-Rao lower bound (CRLB) of the maximum-likelihood phase estimator for a discrete set of complex exponential observations embedded in AWGN [19]. They conjectured that because the estimate depends on the starting point ℓ of the estimation window, an optimum point must exist where the phase estimator's variance is minimum. Their optimization produced $-\ell-(N-1)/2$. The estimator proposed in this research is not in the form suggested by Rife and Boorstyn. Redefining n by

$$n - \ell - \frac{N-1}{2}, \tag{2.40}$$

the modified phase estimator, $\widehat{\theta'_{off}}$, now determines a new phase offset, θ'_{off}, defined as

$$\theta'_{off} = \theta_{off} + \left(\frac{\ell + N - 1}{2}\right) \omega_{off} T_{sa}. \tag{2.41}$$

Substituting (2.40) into (2.18) leads to a redefinition of z_n by z'_n, expressed as

$$\begin{aligned} z'_n &= z_{n-\ell-\frac{N-1}{2}} && (2.42) \\ &= \sum_{k=\ell}^{\ell+W+R-1} g_N\left(\left(n - \ell - \frac{N-1}{2}\right) T_{sa} - kT_{sym}\right) \cdot \\ &\qquad \exp\left\{j\left(\theta'_{off} + \left(n - \ell - \frac{N-1}{2}\right)\omega_{off} T_{sa}\right)\right\} + \gamma(nT_{sa}). && (2.43) \end{aligned}$$

Using (2.29) and (2.31) in (2.43) simplifies the redefined sample to

$$z'_n = \exp\{j\theta'_{off}\} \exp\left\{j\left(n - \ell - \frac{N-1}{2}\right)\omega_{off} T_{sa}\right\} \cdot$$

$$H_N\left(n-\ell-\frac{N-1}{2}\right)+\nu(nT_{sa}) \tag{2.44}$$

$$= B\exp\{j\theta'_{off}\}\exp\left\{j\left(n-\ell-\frac{N-1}{2}\right)\omega_{off}T_{sa}\right\}+\nu(nT_{sa}) \tag{2.45}$$

$$n=\ell,\ell+1,\ldots,\ell+N-1, N=KW, W\ll R.$$

The redefined noise-corrupted sample-statistic reads as

$$\lambda'_\ell = \sum_{n=\ell}^{\ell+N-1} z'_n \tag{2.46}$$

$$= B\exp\{j\theta'_{off}\}\cdot \frac{1}{N}\sum_{n=\ell}^{\ell+N-1}\left[\exp\left\{j\left(n-\ell-\frac{N-1}{2}\right)\omega_{off}T_{sa}\right\}+\nu_n\right]. \tag{2.47}$$

Neglecting noise in (2.47), the averaging statistic is easily shown to equal

$$\lambda'_\ell = B\exp\{j\theta'_{off}\}\frac{1}{N}\sum_{n=\ell}^{\ell+N-1}\exp\left\{j\left(n-\ell-\frac{N-1}{2}\right)\omega_{off}T_{sa}\right\} \tag{2.48}$$

$$= \frac{B}{N}\exp\{j\theta'_{off}\}\exp\left\{j\left(-\ell-\frac{N-1}{2}\right)\omega_{off}T_{sa}\right\}\cdot \sum_{n=\ell}^{\ell+N-1}\exp\{j\omega_{off}T_{sa}n\}. \tag{2.49}$$

Evaluating the sum and simplifying further yields

$$\lambda'_\ell = \frac{B}{N}\exp\{j\theta'_{off}\}\exp\left\{j\left(-\ell-\frac{N-1}{2}\right)\omega_{off}T_{sa}\right\}\cdot \frac{\exp\{j\omega_{off}T_{sa}\ell\}-\exp\{j\omega_{off}T_{sa}(\ell+N)\}}{1-\exp\{j\omega_{off}T_{sa}\}} \tag{2.50}$$

$$= \frac{B}{N}\exp\{j\theta'_{off}\}\cdot \frac{\exp\left(j\left(\frac{-N+1}{2}\right)\omega_{off}T_{sa}\right)-\exp\left(j\left(\frac{N-1}{2}+1\right)\omega_{off}T_{sa}\right)}{\exp(j\omega_{off}T_{sa}/2)[\exp(-j\omega_{off}T_{sa}/2)-\exp(j\omega_{off}T_{sa}/2)]} \tag{2.51}$$

$$= \frac{B}{N}\exp\{j\theta'_{off}\}\cdot \frac{\exp\left(j\left(\frac{-N+1}{2}\right)\omega_{off}T_{sa}\right)-\exp\left(j\left(\frac{N+1}{2}\right)\omega_{off}T_{sa}\right)}{\exp(j\omega_{off}T_{sa}/2)[-\sin(\omega_{off}T_{sa}/2)]} \tag{2.52}$$

$$= \frac{B}{N}\exp\{j\theta'_{off}\}\cdot \frac{\exp\left(j\left(\frac{-N}{2}\right)\omega_{off}T_{sa}\right)-\exp\left(j\left(\frac{N}{2}\right)\omega_{off}T_{sa}\right)}{-\sin(\omega_{off}T_{sa}/2)} \tag{2.53}$$

$$= \frac{B}{N}\exp\{j\theta'_{off}\}\left[\frac{-\sin(N\omega_{off}T_{sa}/2)}{-\sin(\omega_{off}T_{sa}/2)}\right]. \tag{2.54}$$

Taking the argument of λ'_ℓ, and noting that all factors but the exponential bear zero phase, produces the desired result, independent of ω_{off}.

$$\widehat{\theta'_{off}} = \arg\{\lambda'_\ell\} \tag{2.55}$$

$$= \theta'_{off}. \tag{2.56}$$

We now consider the effect of the γ_n noise terms on the averaging statistic, in which case a number of approximations are applied. The expression under the summation in (2.47) may be rearranged into the following equivalent form.

$$\chi_n = \exp\left\{j\left(n-\ell-\frac{N-1}{2}\right)\omega_{off}T_{sa}\right\}+\gamma_n \tag{2.57}$$

$$= \exp\left\{j\left(n-\ell-\frac{N-1}{2}\right)\omega_{off}T_{sa}\right\}+\gamma_{In}+j\gamma_{Qn} \tag{2.58}$$

$$= C_n\exp\left\{j\left[\left(n-\ell-\frac{N-1}{2}\right)\omega_{off}T_{sa}+\epsilon_n\right]\right\} \tag{2.59}$$

where

$$C_n = \sqrt{(\Re\{\chi_n\})^2+(\Im\{\chi_n\})^2} \tag{2.60}$$

$$= \sqrt{\left[\cos\left(\left(n-\ell-\frac{N-1}{2}\right)\omega_{off}T_{sa}\right)+\gamma_{In}\right]^2 + \left[\sin\left(\left(n-\ell-\frac{N-1}{2}\right)\omega_{off}T_{sa}\right)+\gamma_{Qn}\right]^2} \tag{2.61}$$

$$\epsilon_n = \arg\{\gamma_n\}. \tag{2.62}$$

When the signal-to-noise ratio is high, the variance of the in-phase and quadrature noise components is small compared to the signal portion, so the cosine and sine functions can be replaced by their small angle approximations ($\cos(Y) \approx 1$, $\sin(Y) \approx Y$ for $|Y| \ll 1$). C_n reduces to

$$C_n \approx \sqrt{(1+\gamma_{In})^2 + \left(\left(n-\ell-\frac{N-1}{2}\right)\omega_{off}T_{sa} + \gamma_{Qn}\right)^2} \quad (2.63)$$

$$\approx \sqrt{1 + \left(\left(n-\ell-\frac{N-1}{2}\right)\omega_{off}T_{sa} + \gamma_{Qn}\right)^2} \quad (2.64)$$

$$\approx 1. \quad (2.65)$$

The last approximation in (2.64) holds because the terms under the square operation are much smaller than unity, under the small ω_{off} assumption. The resulting averaging statistic simplifies to

$$\lambda'_\ell = \frac{B}{N}\exp\{j\theta'_{off}\}\sum_{n=\ell}^{\ell+N-1}\exp\left\{j\left[\left(n-\ell-\frac{N-1}{2}\right)\omega_{off}T_{sa} + \epsilon_n\right]\right\} \quad (2.66)$$

and the associated phase estimate is

$$\widehat{\theta'_{off}} = \arg\{\lambda'_\ell\} \quad (2.67)$$

$$= \theta'_{off} + \arctan\left\{\frac{\Im\left\{\frac{B}{N}\sum_{n=\ell}^{\ell+N-1}\exp\left\{j\left[\left(n-\ell-\frac{N-1}{2}\right)\omega_{off}T_{sa}+\epsilon_n\right]\right\}\right\}}{\Re\left\{\frac{B}{N}\sum_{n=\ell}^{\ell+N-1}\exp\left\{j\left[\left(n-\ell-\frac{N-1}{2}\right)\omega_{off}T_{sa}+\epsilon_n\right]\right\}\right\}}\right\} \quad (2.68)$$

$$= \theta'_{off} + degradation(\omega_{off}T_{sa}, noise). \quad (2.69)$$

Equation (2.69) indicates that, at large signal-to-noise-ratios, the channel noise corrupting the transmitted signal resembles a phase disturbance. A similar type of modeling, albeit simpler, has been employed by Tretter in [20] to derive phase and

frequency estimators for a discrete complex sinusoid in AWGN using linear regression (known also as least-squares estimation). His proposed phase estimator achieves the CRLB at high signal-to-noise ratios because of the AWGN assumption. Also, pulse-shaping is absent in his model, implying that the bandwidth is infinite. In Tretter's paper, the symbol rate is selected as the sampling rate. Any sampling frequency would not correlate the white Gaussian noise components simply because of the infinite bandwidth.

In the major texts on estimation theory, the performance of an estimator is evaluated in terms of its mean and variance, which in turn require the probability distribution function (*pdf*) of the estimate [21, Ch. 5]. Obtaining the *pdf* of ϵ_n in (2.68) is a formidable task for two major reasons.

Firstly, due to band-limiting and oversampling, the noise is colored and the sample observations become dependent Gaussian random variables. The joint *pdf* of the Gaussian observations is expressed in terms of the mean and covariance matrices, but a different *pdf* exists for each kind of noise considered (the mean and covariance matrices depend on the pulse shaping used). The simplest case, and the most often researched, occurs when the covariance matrix is diagonal. The samples in this case are taken at the symbol rate and, so, remain independent by satisfying the zero-ISI pulse-shaping condition. The other possibility includes a matched filter with a bandwidth equal to or higher than the sampling rate. This case is of little practical interest for high sampling rates as the bandwidth is restricted by the requirements of current and emerging technologies.

The second major difficulty lies in ϵ_n being expressed in a non-linear function (the exponential). The solution to this problem generally involves a non-linear procedure, but the effort associated with it is great and, occasionally, unsatisfactory [22].

2.3 Analytical Study of Phase Estimator Statistics

2.3.1 Cramér-Rao Lower Bound for Phase Offset Estimation

For phase estimation of a complex sinusoid embedded in AWGN, the CRLB is expressed as [19].

$$\sigma^2_{\widehat{\theta'_{off}}} \geq \frac{1}{2N(E_s/N_0)} \tag{2.70}$$

where N is the number of independent samples (usually selected at the symbol rate owing to the zero-ISI requirements of matched filtering), and E_s/N_0 is the average symbol-energy-to-noise ratio.

For QPSK/4QAM and OQPSK,

$$\sigma^2_{\widehat{\theta'_{off}}} \geq \frac{1}{4N(E_b/N_0)}. \tag{2.71}$$

E_b/N_0 is the average signal-to-noise ratio in terms of the average bit energy E_b (note: $E_s = 2E_b$ for QPSK/4QAM and OQPSK).

The derivation of the CRLB involved an unmodulated carrier since modulation is expected to introduce a degradation. Hence, the modulated CRLB could never outperform the unmodulated case [22]. This unmodulated CRLB assumption is generally accepted and adopted throughout the literature, as well as in this text.

2.3.2 Mean of Phase Offset Estimator by Analysis

This section focuses on an approximate expression for the mean of $\widehat{\theta'_{off}}$ in order to evaluate its bias.

It is more fitting to find the mean of the error between the estimate and the true phase value. Let $\delta = \widehat{\theta'_{off}} - \theta'_{off}$ be the new random variable in question. Notice

from (2.69) that δ corresponds to the degradation term due to frequency error and random noise. The moment we seek is exactly the mean of the degradation. Taking the expectation of δ.

$$E[\delta] = E[\widehat{\theta'_{off}} - \theta'_{off}] \tag{2.72}$$

$$= E[\widehat{\theta'_{off}}] - E[\theta'_{off}] \tag{2.73}$$

$$= E[\widehat{\theta'_{off}}] - \theta'_{off}. \tag{2.74}$$

θ'_{off} represents a deterministic but unknown quantity, on which the expectation operator $E[\cdot]$ has no effect. In general, θ'_{off} assumes values within $[-\pi, \pi]$, but for the sake of simplicity, let it be known. In fact, without loss of generality, let's equate it to zero. Simulations in a later section verify the validity of this assumption.

From a graphical point of view, δ may be interpreted as depicted in figure 2.2(a).

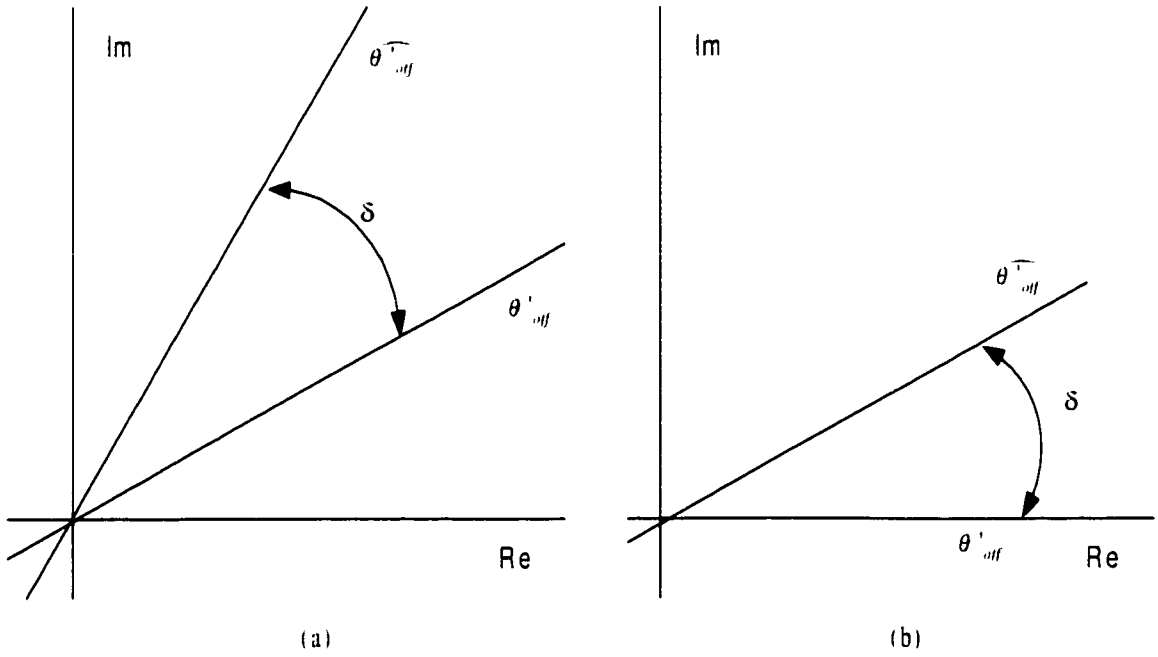

Figure 2.2: Phase Degradation of $\widehat{\theta'_{off}}$ with respect to θ'_{off}. (a) $\theta'_{off} \neq 0$: (b) $\theta'_{off} = 0$.

When the noise variance is small (occurring for high signal-to-noise ratios) and frequency errors assume insignificant values so that they are negligible, $\widehat{\theta'_{off}}$ is intuitively expected to closely approximate the true offset. With $\theta'_{off} = 0$, $\delta = \widehat{\theta'_{off}}$ and $E[\delta] = E[\widehat{\theta'_{off}}]$. Hence, the estimates cluster around the real axis (see figure 2.2(b)).

Moreover, a small θ'_{off} suggests a potential linearization of the argument function encountered in (2.67). Most commonly, an arctangent operation recovers the averaging statistic's phase value. For minor values of θ'_{off}, and consequently $\widehat{\theta'_{off}}$, $\arctan(\widehat{\lambda_\ell}) \approx \widehat{\lambda_\ell}$. Under this condition, the expectation can be moved inside the arctangent function[2].

$$E[\widehat{\theta'_{off}}] = E\left[Arg\left(\frac{1}{N}\sum_{n=\ell}^{\ell+N-1} z_n\right)\right] \tag{2.75}$$

$$= Arg\left(E\left[\frac{1}{N}\sum_{n=\ell}^{\ell+N-1} z_n\right]\right) \tag{2.76}$$

$$= Arg\left(\frac{1}{N}\sum_{n=\ell}^{\ell+N-1} E[z_n]\right). \tag{2.77}$$

Applying (2.29) and (2.31) to the noisy observations generates

$$z_n = B\exp\left\{j\theta'_{off}\right\}\exp\left\{j\left(n-\ell-\frac{N-1}{2}\right)\omega_{off}T_{sa}\right\} + \gamma_n. \tag{2.78}$$

The expectation of (2.78) may be expanded into the following expression:

$$E[z_n] = E\left[B\exp\left\{j\theta'_{off}\right\}\exp\left\{j\left(n-\ell-\frac{N-1}{2}\right)\omega_{off}T_{sa}\right\} + \gamma_n\right]. \tag{2.79}$$

We immediately observe that γ_n is the only random quantity in (2.79), i.e.,

$$E[z_n] = B\exp\left\{j\theta'_{off}\right\}\exp\left\{j\left(n-\ell-\frac{N-1}{2}\omega_{off}T_{sa}\right)\right\} + E[\gamma_n]. \tag{2.80}$$

[2]The $\approx$ signs are dropped to alleviate the notation.

The channel was assumed zero mean in both its real and imaginary components, a property that is evidently retained by the filtered noise process at the output of the linear operation of $G_R(\omega)$. Consequently, $E[z_n] = 0$. The expected value of z_n is merely reduced to its deterministic component, whereas the noise is averaged out, leading to

$$E[z_n] = B \exp\left\{j\theta'_{off}\right\} \exp\left\{j\left(n - \ell - \frac{N-1}{2}\right)\omega_{off}T_{sa}\right\}. \tag{2.81}$$

Substituting this result into (2.77) and rearranging some factors yields

$$E[\widehat{\theta'_{off}}] \approx Arg\left[\frac{B}{N}\exp\left\{\theta'_{off}\right\}\sum_{n=\ell}^{\ell+N-1}\exp\left\{j\left(n - \ell - \frac{N-1}{2}\right)\omega_{off}T_{sa}\right\}\right] \tag{2.82}$$

$$= Arg\left[\frac{B}{N}\exp\left\{j\theta'_{off}\right\}\left(\frac{-\sin(N\omega_{off}T_{sa}/2)}{-\sin(\omega_{off}T_{sa}/2)}\right)\right] \tag{2.83}$$

$$= \theta'_{off}. \tag{2.84}$$

In view of the previous assumptions and the fact that only the exponential factor retains a non-zero phase, $\widehat{\theta'_{off}}$ generates an unbiased estimate of the true offset, as desired. Also, note that the mean of $\widehat{\theta'_{off}}$ is independent of ω_{off}, since ω_{off} displays even symmetry about the center of the estimation window.

2.3.3 Variance of Phase Offset Estimator by Analysis

An analytical expression for the variance of $\widehat{\theta'_{off}}$ is derived in this section. The frequency offset is set to zero, but its effects on the variance of $\widehat{\theta'_{off}}$ are studied through simulations.

Under the same provisions of the previous section and application of (2.29) and

(2.31), the observations are expressed as

$$z'_n = \exp\left\{j\theta'_{off}\right\} \sum_{n=\ell}^{\ell+N-1} g_N\left(\left(n-\ell-\frac{N-1}{2}\right)T_{sa} - kT_{sym}\right) + \gamma_n \quad (2.85)$$

$$= B\exp\left\{j\theta'_{off}\right\} + \gamma_n \quad (2.86)$$

$$= x_n + jy_n. \quad (2.87)$$

The variance of $\widehat{\theta'_{off}}$ then equals

$$var\left(\widehat{\theta'_{off}}\right) = E\left[\left(\widehat{\theta'_{off}} - E\left[\widehat{\theta'_{off}}\right]\right)^2\right] \quad (2.88)$$

$$= E\left[\widehat{\theta'_{off}}^2\right] - \left(E\left[\theta'_{off}\right]\right)^2 \quad (2.89)$$

$$= E\left[\widehat{\theta'_{off}}^2\right] - \left(\theta'_{off}\right)^2 \quad (2.90)$$

where the squared mean is easily derived with the results of section 2.3.2. From (2.90), the first term on the right hand side needs to be evaluated in order to determine the variance. Substituting (2.47), (2.55) and (2.87) into the first term of (2.90) results in

$$E\left[\widehat{\theta'_{off}}^2\right] = E\left[\left(Arg\left(\frac{1}{N}\sum_{n=\ell}^{\ell+N-1} x_n + jy_n\right)\right)^2\right] \quad (2.91)$$

$$= E\left[\arctan^2\left(\frac{\frac{1}{N}\sum_{n=\ell}^{\ell+N-1} y_n}{\frac{1}{N}\sum_{n=\ell}^{\ell+N-1} x_n}\right)\right]. \quad (2.92)$$

For small phase offsets ($\theta'_{off} \approx 0$) and small noise variance (thus small estimation errors), $\sum_n y_n \ll \sum_n x_n$ because the summation over x_n is approximately constant, and the variances of both the real and imaginary parts are small compared to the squared real mean [9]. This allows the linearization of the argument function in (2.91) and

allows the expectation to be moved inside the summation. This simplifies (2.92) to

$$E\left[\widehat{\theta'_{off}}^{2}\right] = E\left[\arctan^{2}\left(\frac{1}{N}\sum_{n=\ell}^{\ell+N-1} y_n\right)\right] \tag{2.93}$$

$$= E\left[\left(\frac{1}{N}\sum_{n=\ell}^{\ell+N-1} y_n\right)^{2}\right] \tag{2.94}$$

$$= E\left[\left(\frac{B}{N}\sum_{n=\ell}^{\ell+N-1} \sin(\theta'_{off}) + \gamma_{Qn}\right)^{2}\right]. \tag{2.95}$$

Expanding the square and evaluating the expectation over appropriate terms yields

$$E\left[\widehat{\theta'_{off}}^{2}\right] = E\left[\frac{1}{N^2}\sum_{n=\ell}^{\ell+N-1}\sum_{p=\ell}^{\ell+N-1}\left(B\sin(\theta'_{off}) + \gamma_{Qn}\right)\left(B\sin(\theta'_{off}) + \gamma_{Qp}\right)\right] \tag{2.96}$$

$$= \frac{1}{N^2}\sum_{n=\ell}^{\ell+N-1}\sum_{p=\ell}^{\ell+N-1} E\left[B^2\sin^2(\theta'_{off})\right] + E\left[B\sin(\theta'_{off})\gamma_{Qp}\right] + E\left[B\sin(\theta'_{off})\gamma_{Qn}\right] + E\left[\gamma_{Qn}\gamma_{Qp}\right]. \tag{2.97}$$

The second and third expectations under the double summation in the above equation vanish since the $\sin(\cdot)$ and B factors are deterministic quantities, whereas γ_{Qn} and γ_{Qp} are zero mean random variables. Hence,

$$E\left[\widehat{\theta'_{off}}^{2}\right] = \frac{1}{N^2}\sum_{n=\ell}^{\ell+N-1}\sum_{p=\ell}^{\ell+N-1} E\left[B^2\sin^2(\theta'_{off})\right] + R_{\gamma_Q}(n-p)$$

$$= \frac{1}{N^2}\left[N^2B^2\sin^2(\theta'_{off}) + \sum_{n=\ell}^{\ell+N-1}\sum_{p=\ell}^{\ell+N-1} R_{\gamma_Q}(n-p)\right] \tag{2.98}$$

$$= B^2\sin^2(\theta'_{off}) + \frac{1}{N^2}\sum_{n=\ell}^{\ell+N-1}\sum_{p=\ell}^{\ell+N-1} R_{\gamma_Q}(n-p). \tag{2.99}$$

where the substitution $R_{\gamma_Q}(n-p) = E\left[\gamma_{Qn}\gamma_{Qp}\right]$ of the noise autocorrelation function

was performed. For convenience let $\theta'_{off} = 0$ so that

$$E\left[\widehat{\theta'_{off}}^{2}\right] = \frac{1}{N^2}\sum_{n=\ell}^{\ell+N-1}\sum_{p=\ell}^{\ell+N-1} R_{\sim_Q}(n-p). \tag{2.100}$$

If $R_{\sim_Q}(n-p)$ is even-symmetric and real, which is usually the case for raised-cosine pulse-shaping, then the associated covariance matrix constructed from $R_{\sim_Q}(n-p)$ is Toeplitz and real. Manipulating the terms under the double summation of (2.100) yields

$$E\left[\widehat{\theta'_{off}}^{2}\right] = \frac{1}{N^2}\left(NR_{\sim_Q}(0) + \sum_{m=1}^{N-1} 2(N-m)R_{\sim_Q}(m)\right) \tag{2.101}$$

$$= \frac{1}{N}R_{\sim_Q}(0) + \frac{1}{N^2}\sum_{m=1}^{N-1} 2(N-m)R_{\sim_Q}(m). \tag{2.102}$$

$R_{\sim_Q}(0)$ represents the noise variance of the quadrature channel, $\sigma_Q^2 = N_0/2$. Hence, the first term can be expressed in terms of the channel symbol-energy-to-noise ratio E_s/N_0. The noise power in one channel is half of the noise power in the total channel, i.e., $\sigma_Q^2 = \frac{1}{2}\sigma_{channel}^2$, where $\sigma_{channel}^2 = N_0$ [20]. Therefore,

$$\sigma_Q^2 = R_{\sim_Q}(0) \tag{2.103}$$

$$= \frac{1}{2(E_s/N_0)}. \tag{2.104}$$

In the case of uncorrelated Gaussian noise samples (for which independence holds), substituting (2.104) into (2.102), and noting that the summation term is zero under independence conditions, results in the CRLB for a complex sinusoid in AWGN (see (2.70)):

$$E\left[\widehat{\theta'_{off}}^{2}\right] = \frac{1}{2N(E_s/N_0)}. \tag{2.105}$$

If independence of the samples is not fulfilled, then the second term in (2.102) represents a weighted summation of the quadrature channel autocorrelation function. It is equivalent to an extra degradation component arising from the noise correlation. A stronger dependence between samples intensifies the degradation, suggesting that higher sampling rates be avoided. Simulations give an alternative interpretation so the effect of the autocorrelation summation does not seem as severe as (2.102) leads on. It is obvious from (2.102) that larger estimation windows should improve the performance.

2.4 Performance Evaluation of Phase Offset Estimator by Simulation

This section links the theoretical findings of the previous sections with the more practical results obtained by extensive simulations. The simulations evaluate the estimate's *pdf*, its mean and its variance.

In addition, BER simulations compare the simulated burst-modem with an approximate bound, and are later compared to results measured with a physical QPSK/4QAM and OQPSK modem system. The section concludes with a discussion of a purely digital implementation of the algorithm.

2.4.1 Probability Density Function of Phase Offset Estimator

The first step in evaluating the phase estimator's performance is to determine how the oversampling affects the estimate's *pdf* and its moments. A closed form solution for the *pdf* is not possible for the case of oversampling, whereas a solution to the case of one-time sampling per symbol is possible after a laborious process [22]. Figures 2.3 to 2.7 show the effect of K for QPSK/4QAM and OQPSK, for varying

E_b/N_0 ($5dB$ and $15dB$) and an estimation window of $4K$ samples. The dotted points represent histogram plots of the occurrences of $\widehat{\theta'_{off}}$ using 10^4 estimates. In all cases, the *pdf* is even symmetric about the θ'_{off} and obeys a Gaussian distribution or a very close approximation thereof. The case shown is for a zero θ'_{off}, but the *pdf* was observed to behave in the same fashion for non-zero values as well. In general it focuses around θ'_{off}. The solid line depicts a true Normal distribution with mean and variance obtained directly from the moments of the estimates. Clearly the Gaussian *pdf* assumption is valid. In figures 2.6 and 2.7, the solid lines of figures 2.3, 2.4 and 2.5 are overlapped to demonstrate that oversampling marginally affects the *pdf* of $\widehat{\theta'_{off}}$ for both E_b/N_0. Consequently, approximately the same moments will result for different K, leading to similar performances.

Although varying the number of samples per symbol does not provide a performance advantage, it is not degraded either. This observation suggests that oversampling is not necessary. However, from a physical implementation viewpoint, it is more practical to design with as few clock domains as possible, especially at higher operating frequencies where clock skew may cause a system to behave erratically[3]. Multiple system clocks require extremely accurate timing alignment between clock regions so the implementation necessitates added attention. Furthermore, oversampling simplifies system integration with other components also based on oversampling, such as STR and equalization, since one sampling clock is employed. Already, modulator and demodulator structures proposed in [23], as well as the STR algorithm in [2] use two-fold and four-fold oversampling with a marginal resource cost.

[3]Clock skew is a phenomenon in which the clock signal arrives at one point before or after another instead of at the same time. High speed systems are very susceptible to clock skew because of the small propagation delays tolerated by the high operating frequency. Careful system design, particularly minimization of clock skew, becomes of primary importance.

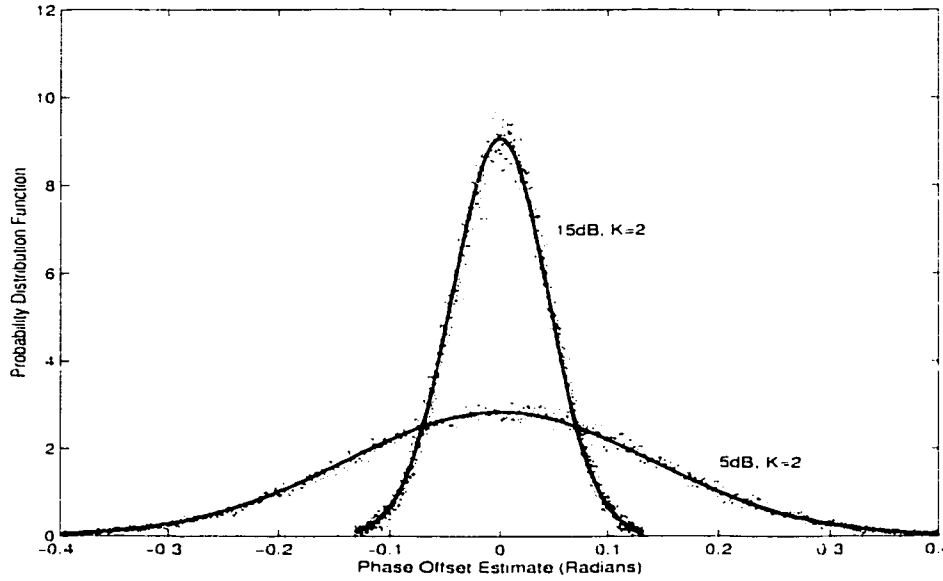

Figure 2.3: Plot of the *pdf* of $\widehat{\theta'_{off}}$ for $K = 2$; $N = 4K$, $\theta'_{off} = 0$, $\omega_{off} = 0$ (QPSK/4QAM and OQPSK).

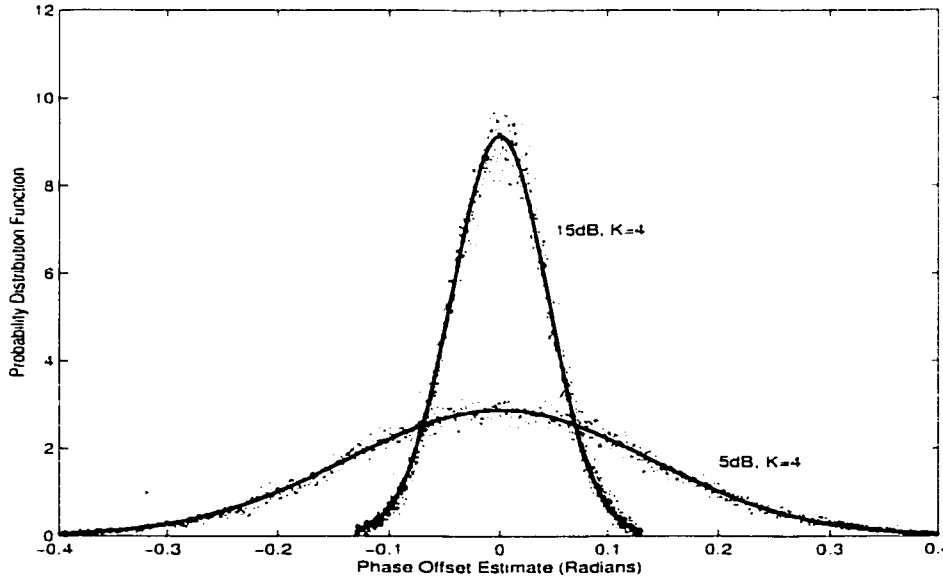

Figure 2.4: Plot of the *pdf* of $\widehat{\theta'_{off}}$ for $K = 4$; $N = 4K$, $\theta'_{off} = 0$, $\omega_{off} = 0$ (QPSK/4QAM and OQPSK).

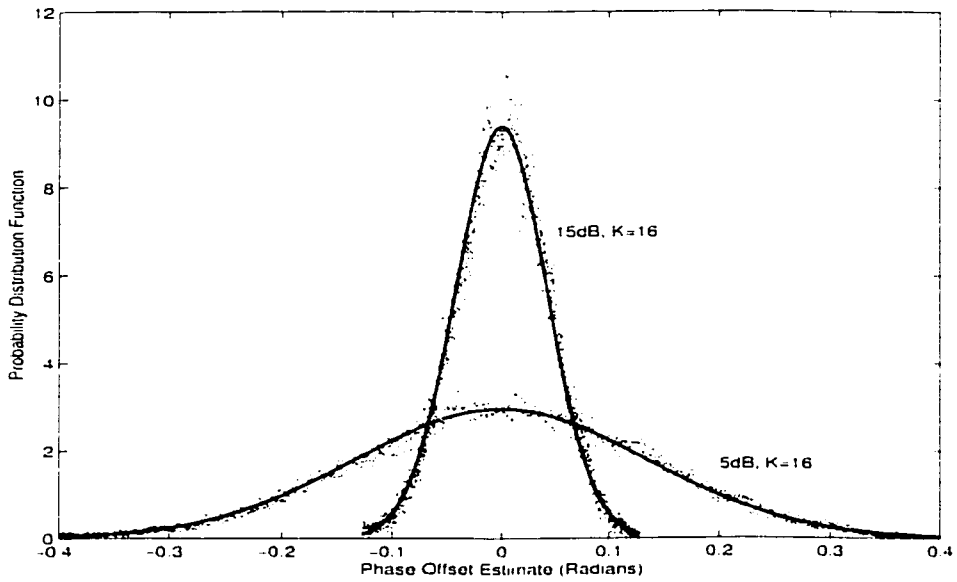

Figure 2.5: Plot of the *pdf* of $\widehat{\theta'_{off}}$ for $K = 16$; $N = 4K$, $\theta'_{off} = 0$, $\omega_{off} = 0$ (QPSK/4QAM and OQPSK).

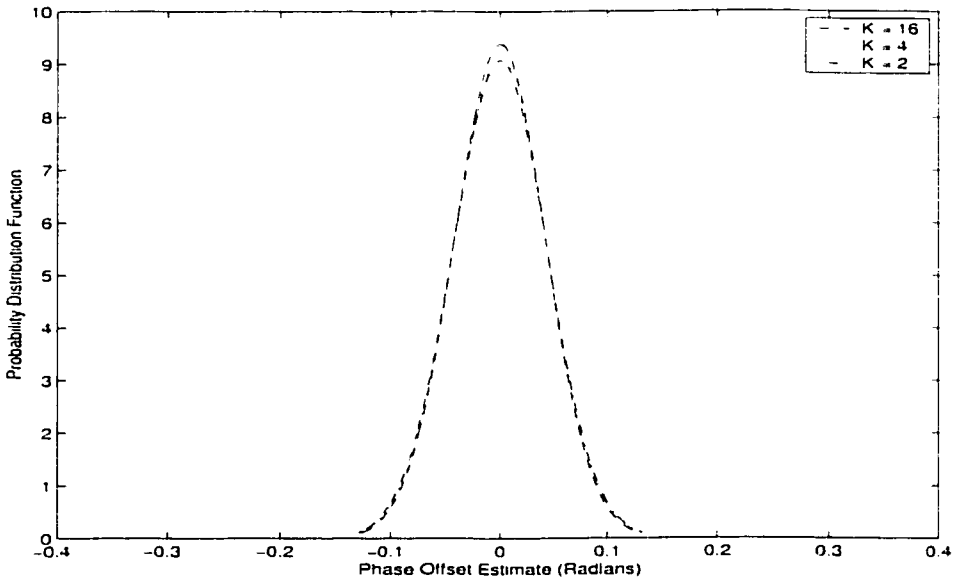

Figure 2.6: Plot of the *pdf* of $\widehat{\theta'_{off}}$ for Varying Values of K; $N = 4K$, $\theta'_{off} = 0$, $\omega_{off} = 0$ (QPSK/4QAM and OQPSK).

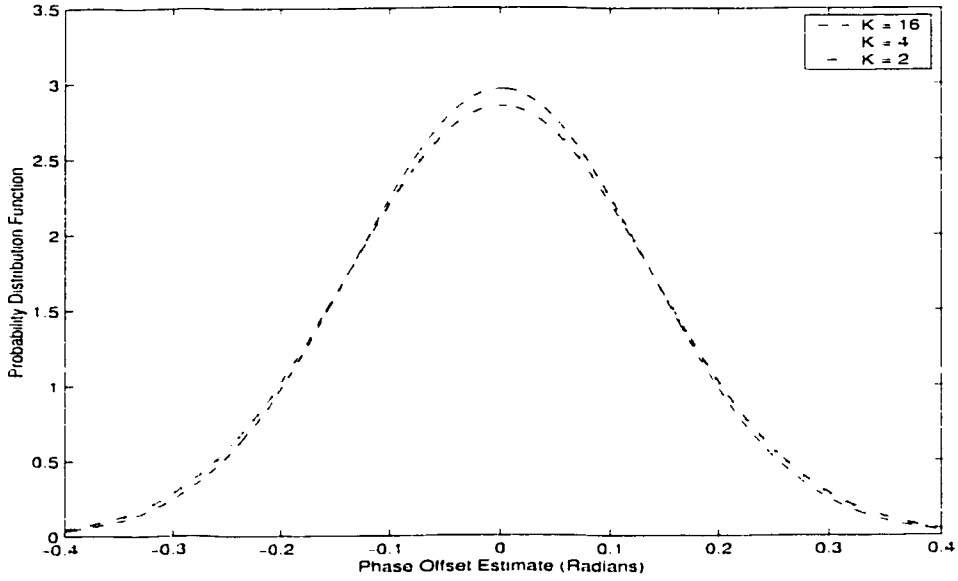

Figure 2.7: Plot of the *pdf* of $\widehat{\theta'_{off}}$ for Varying Values of K: $N = 4K$, $\theta'_{off} = 0$, $\omega_{off} = 0$ (QPSK/4QAM and OQPSK).

A similar histogram analysis is now shown in figure 2.8 for E_b/N_0 equal to $5dB$ and $15dB$, varying window size N, and a fixed K ($K = 16$ times oversampling). Once again, the estimates are Gaussian-distributed for N equal to $2K$, $4K$ and $16K$. The behavior is similar for both E_b/N_0. More observations concentrate the *pdf* closer around the mean, indicating that the corresponding variance is decreasing. Such behavior is strongly anticipated since, intuitively, more samples per observation window should average out the effects of the noise and, consequently, give rise to more accurate estimates. The results presented in this section are now summarized:

1. Oversampling marginally affects the phase offset estimate's *pdf* and is not expected to influence the estimator's performance, although it can reduce the number of required clock domains and simplify system integration with other oversampled units (STR and equalization).

2. Increasing the estimation window produces a focused *pdf*, so the estimates cluster more tightly about the parameter of interest.

The next few sections verify these assertions by simulation.

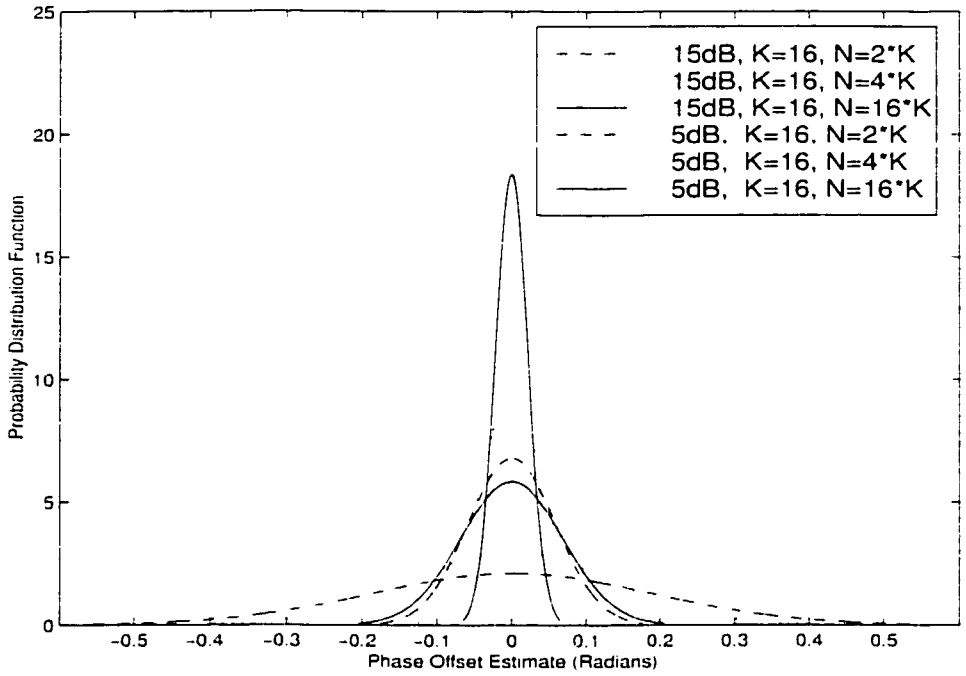

Figure 2.8: Plot of the *pdf* of $\widehat{\theta'_{off}}$ for Varying Values of N: $K = 16$, $\theta'_{off} = 0$, $\omega_{off} = 0$ (QPSK/4QAM and OQPSK).

2.4.2 Mean of Phase Offset Estimator by Simulation

The mean is the first criterion in judging an estimator's performance. In particular, the estimate should be unbiased if it is to focus around the true value. For non-random but unknown parameters, the introduced bias equals the difference between the estimate's mean and the true value. To verify equation (2.84), the mean of $\widehat{\theta'_{off}}$ is evaluated by simulation for moderate E_b/N_0. A wide sweep of θ'_{off} checks the bias for larger non-zero phase offsets. Figure 2.9 illustrates the behavior of $E\left[\widehat{\theta'_{off}}\right]$ with respect to the true phase offset for K equal to 2, 4, and 16-times oversampling.

$N = 4K$ and QPSK/4QAM and OQPSK modulation at $E_b/N_0 = 5dB$. The results were very similar for these modulation formats.

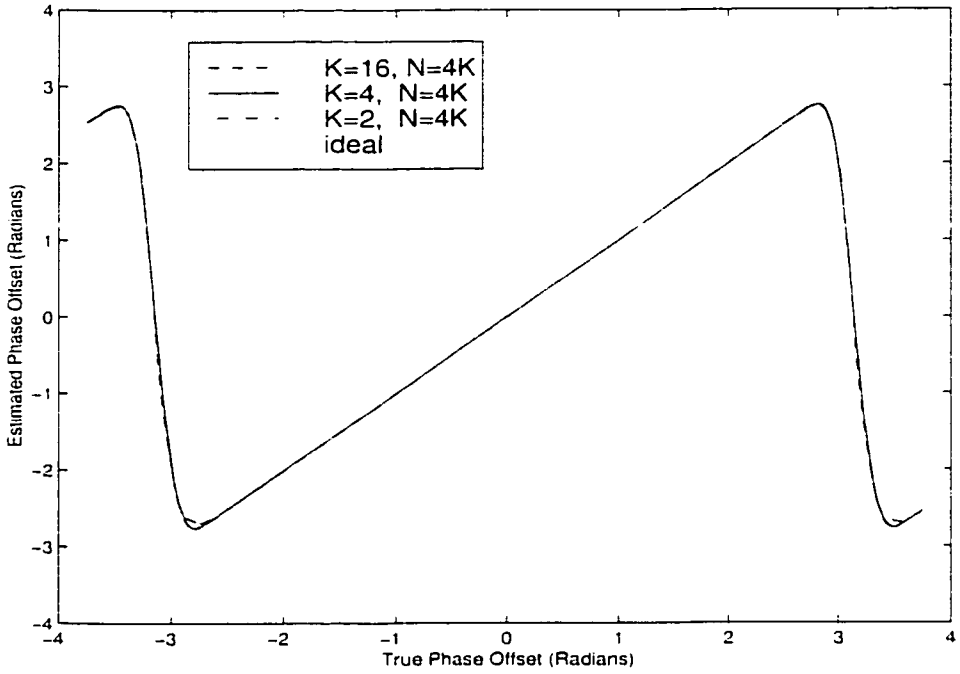

Figure 2.9: Mean of $\widehat{\theta'_{off}}$ versus the True Phase Error: Effect of K, $\omega_{off} = 0$, $E_b/N_0 = 5dB$ (QPSK/4QAM and OQPSK).

As expected from section (2.4.2), $\widehat{\theta'_{off}}$ is unbiased for virtually the entire range $[-\pi, \pi]$, outside of which modulo-2π foldover of the phase occurs due to the arctangent's limited range. Nevertheless, the reader should note that the entire range of angles is covered with a slight bias appearing exclusively around the foldover points. Angles lying outside $[-\pi, \pi]$ map within $[-\pi, \pi]$ and preserve their original phase information. For practical systems, K may be selected to satisfy the oversampling requirements of a given application. Most contemporary systems operate at higher bit rates and can also use 2 to 4 samples per symbol, whereas lower capacity applications may increase this factor to 16 with only a minor penalty in hardware cost. For instance, symbol-timing recovery usually requires oversampled symbols to accurately

determine the symbol-timing clock. The matched filter may also run at the higher rate. Hence, practical systems already benefit from oversampling and the extension to carrier recovery is straightforward.

Varying K does not induce a bias; however, the same does not hold entirely when the estimation window length varies. Figure 2.10 exemplifies a larger yet tolerable bias near the $\pm\pi$ foldover points for small N (which uses less samples per estimation interval). The bias may be circumvented by increasing N. The bias is essentially negligible in $[-\pi, \pi]$ when the estimation window is composed of 16 symbols oversampled by $K = 16$, as opposed to shorter windows of $4K$ and $2K$. A similar observation is noted in the next section for the variance of $\widehat{\theta'_{off}}$.

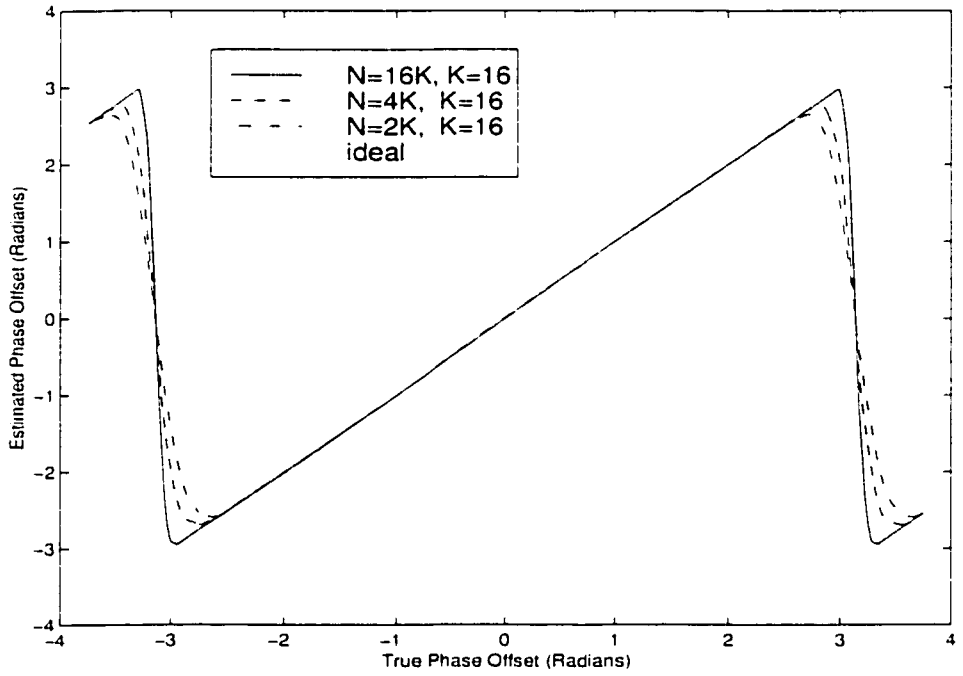

Figure 2.10: Mean of $\widehat{\theta'_{off}}$ versus the True Phase Error: Effect of N. $\omega_{off} = 0$. $E_b/N_0 = 5dB$ (QPSK/4QAM and OQPSK).

2.4.3 Variance of Phase Offset Estimator by Simulation

The variance constitutes the second most crucial performance measure of an estimator. It informatively describes the estimate's deviation from the value being estimated. A smaller variance is always desirable because the estimates would then gather more closely around the actual offset and, correspondingly, reduce the root-mean-square error. Figure 2.11 convincingly validates via simulation the variance approximation derived in section 2.3.3. The overall performance closely matches that of an equivalent efficient estimator achieving the CRLB (in the presence of AWGN and founded on one matched filter sample per symbol, i.e., N/K symbols). The results are plotted versus N for common values of E_b/N_0. The system operates in burst-mode QPSK/4QAM and OQPSK. The dotted lines represent the CRLB for a complex sinusoid in AWGN for N/K symbols, with $K = 16$. The simulations indicate that the variance compares favorably to the CRLB of an equivalent efficient estimator using N/K symbols using one sample per symbol interval. The high signal-to-noise ratio approximation (2.102), illustrated by the solid lines, and the simulations, shown as circles, hug the CRLB for all E_b/N_0 and N of interest. As expected, the variance diminishes with increasing N. Estimation window sizes between $4K$ and $16K$ samples, i.e., 4 to 16 QPSK/4QAM or OQPSK, are optimal for low complexity and small overhead.

The analytical approximation for the variance is valid at high signal-to-noise ratio, but tends to be misleading for smaller estimation windows, providing slightly optimistic values with regard to the CRLB.

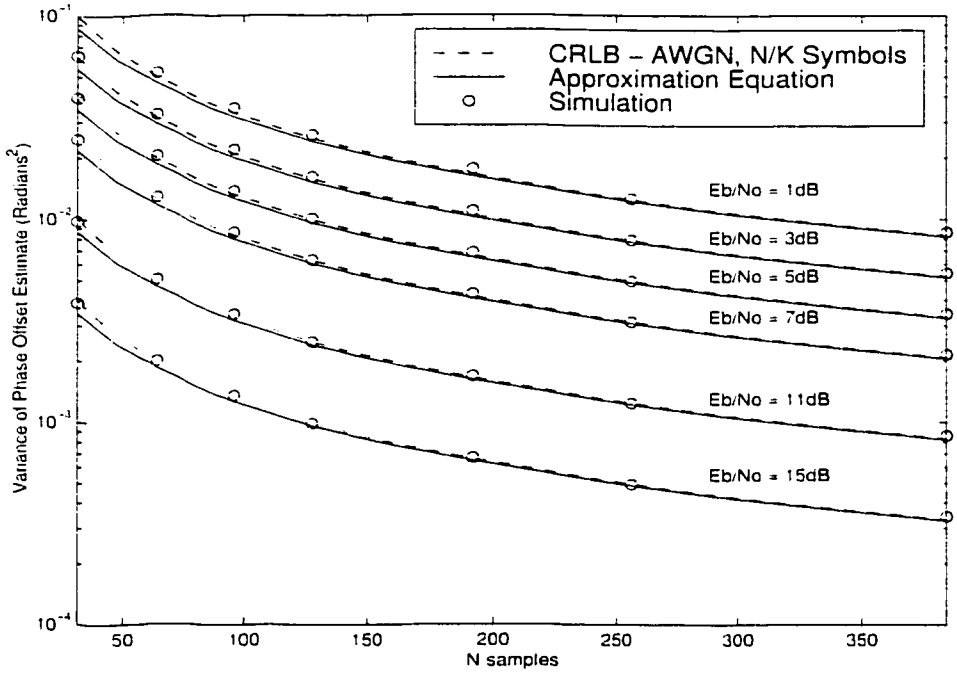

Figure 2.11: Variance of $\widehat{\theta'_{off}}$ versus Window Length N: $\theta'_{off} = 0$, $\omega_{off} = 0$, K=16.

It has already been seen from the mean and variance of $\widehat{\theta'_{off}}$ that oversampling has a minute effect on the estimator's performance, and that the performance is very similar to that of traditional ML single-sample-per-symbol estimators averaging N/K symbols. However, the oversampling estimator does not perform worse than an efficient estimator using N/K symbols because it was assumed that, on the average, each symbol is of energy E_s. Oversampling the preamble by K increases the amount of noise approximately K times per symbol (because the preamble possesses approximately constant amplitude, see (2.31)) so that any performance gain achieved with K samples per symbol is countered by an equivalent loss due to the additional noise resulting from oversampling. In light of this information, the performance comparison should be carried out on the basis of the number of symbols rather than the number of samples. Under this condition alone can the proposed estimator be considered efficient. Although oversampling does not improve the variance, multiple samples per

symbol present benefits in a hardware implementation as discussed earlier in section 2.4.1.

FF phase estimators often perform poorly under the influence of non-zero frequency offsets. For example, the performance of the V&V algorithm [16] decreases rapidly, even for very small frequency offsets. The author in [22] determines that the V&V phase estimation technique can sustain a frequency error of up to 1% of the symbol rate before estimation is severely degraded. His analysis assumes an infinite bandwidth AWGN channel using rectangular pulse shaping. A method exploiting the symmetry of the frequency offset about the center of the estimation window is presented to estimate the phase offset independently of the frequency offset, with only a moderate increase in hardware complexity [22].

The algorithm proposed here resembles an oversampled version of the V&V algorithm and unfortunately suffers from a similar performance degradation when subjected to a rather small ω_{off}. Figure 2.12 illustrates the behavior for the case of $K = 16$, $N = 4K$ and two values of E_b/N_0. The frequency offset normalized to the symbol period, $\Delta f T_{sym}$, is varied between zero and 10% of the symbol rate. The range of tolerable frequency offset in the band-limited channel is extremely narrow, approximately $\pm 0.3\%$ of the symbol rate. The smaller range is not attributed to oversampling in our case but rather to band-limiting of the channel.

To understand the implications of this result, consider the case of a QPSK system operating at 100 Mbps (50 Mbaud symbol rate) and transmitted over two different carrier frequencies, 150MHz (narrowband) and 38GHz (wideband). Also, assume that the oscillators are accurate to $\pm$100ppm. After transmission and reception, a maximum $\pm$200ppm frequency error may be embedded in the demodulated data. For the 150MHz case, this is equivalent to a $\pm$30kHz maximum frequency error, while for 38GHz, it corresponds to $\pm$7.6MHz. Based on figure 2.12, the maximum tolerable

offset by the phase offset estimator is ±0.3% of 50Mbaud, or ±150kHz. Although the estimator is still capable of operating in the narrowband case, it fails in the wideband setting (as does the V&V technique). This indicates that higher precision oscillators are required (with a maximum ±2ppm deviation at most for the 38GHz example), which ultimately increases the transceiver production costs. If this is not the case, a substantial increase in the bit-rate (about 51 times) would be necessary, which is clearly not feasible in practice. Hence, the application of the phase estimator with loose oscillator tolerances should be avoided where applicable.

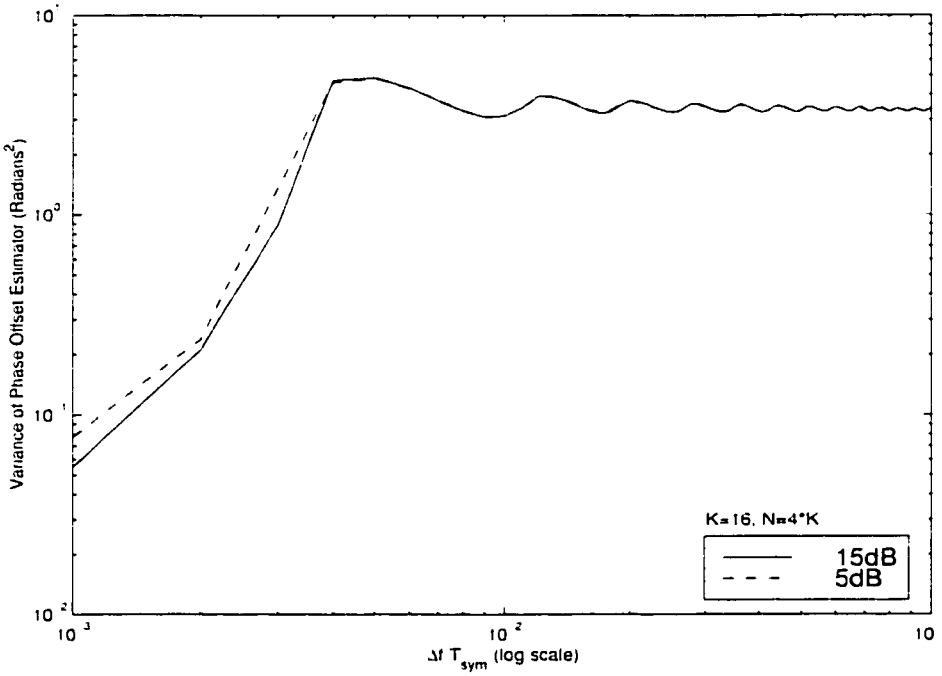

Figure 2.12: Variance of $\widehat{\theta'_{off}}$ versus Frequency Offset ω_{off} (log scale)

2.4.4 BER Performance of Phase Offset Estimator

In most physical implementations, the BER and the BER degradation constitute two commonly used figures-of-merit for a practical modem design. For illustrative purposes, BER tests were performed for burst-mode QPSK/4QAM and OQPSK.

The theoretical BER for QPSK/4QAM and OQPSK is

$$BER_{QPSK} = Q\left(\sqrt{\frac{2E_b}{N_0}}\right) \tag{2.106}$$

where $Q(x)$ is the Markum Q-function defined by [12, Sec 4.4]

$$Q(x) = \frac{1}{2\pi}\int_x^\infty e^{-x^2/2}\,dx. \tag{2.107}$$

E_b is the average signal power integrated over one bit period, $N_0/2$ is the double-sided *psd* of AWGN, and E_b/N_0 is the bit-energy-to-noise ratio. Equation (2.106) serves as the reference for the simulation results and the practical measurements.

To determine an approximate mathematical expression for the BER degradation incurred by the variance of $\widehat{\theta'_{off}}$, the procedure described in [9, Ch. 7] is applied. Although $\widehat{\theta'_{off}}$ is obtained using the correlated observations at the output of the matched filter, the symbols of useful information need only be corrected at the symbol rate since at that time the estimated offsets will be known. Moreover, since perfect symbol-timing is assumed during the correction of the burst's payload (at the symbol rate), independent matched-filtered symbol decisions result. Hence, the results derived in [9, Ch. 7] apply here without restrictions.

In general, the BER degradation D is defined by

$$D = -10\log\left(\frac{\sigma^2}{\sigma_0^2}\right) \tag{2.108}$$

where σ^2 and σ_0^2 are determined by

$$BER_0 = P(0;\sigma_0^2) \tag{2.109}$$

$$= E_\psi[P(\psi;\sigma)] \tag{2.110}$$

in which $P(w;\sigma^2)$ is the conditional BER associated with the synchronization error $w = \theta'_{off} - \widehat{\theta'_{off}}$ at $E_s/N_0 = 1/(2\sigma^2)$, and $E_w[P(w;\sigma)]$ involves the expectation over the synchronization error w. An approximate relationship for the degradation is derived in [9, Ch. 7] when the synchronization error is small.

$$D \approx \frac{10}{\ln(10)}\left(F + \frac{J}{\sigma_0^2}\right) var(w) \quad [dB] \tag{2.111}$$

where

$$F = \frac{1}{d(0)} E_{\underline{a}}\left[-d^{(ww)}(0)\right] \tag{2.112}$$

$$J = E_{\underline{a}}\left[(d^{(w)}(0))^2\right] \tag{2.113}$$

and

$$d(w) = \Im\left\{s(w)e^{j\pi/M}\right\}. \tag{2.114}$$

The expressions $d^{(w)}(w)$ and $d^{(ww)}(w)$ represent the first and second order derivatives of $d(w)$ with respect to w, respectively, and $E_{\underline{a}}[\cdot]$ denotes averaging over the symbol sequence $\underline{a}$ (or $\{a_k\}$).

For M-PSK, $s(w) = e^{jw} = \cos w + j \sin w$ so that

$$d(w) = \sin(w + \pi/M) \tag{2.115}$$

$$= \cos(w)\sin(\pi/M) + \sin(w)\cos(\pi/M). \tag{2.116}$$

Calculating the first and second order derivatives of $d(w)$ with respect to w, we

obtain

$$d^{(\epsilon)}(\epsilon) = -\sin(\epsilon)\sin(\pi/M) + \cos(\epsilon)\cos(\pi/M) \quad (2.117)$$

$$d^{(\epsilon\epsilon)}(\epsilon) = -\cos(\epsilon)\sin(\pi/M) - \sin(\epsilon)\cos(\pi/M). \quad (2.118)$$

Evaluating the derivatives at zero and substituting these results into F and J, followed by the evaluation of the expectation $E_{\underline{a}}[\cdot]$ over the symbol sequence $\underline{a}$, yields

$$F = \frac{1}{\sin(\pi/M)} E_{\underline{a}}[\sin(\pi/M)] \quad (2.119)$$

$$= 1. \quad (2.120)$$

$$J = E_{\underline{a}}\left[(\cos(\pi/M))^2\right] \quad (2.121)$$

$$= \cos^2(\pi/M) \quad (2.122)$$

For QPSK/4QAM and OQPSK, $M = 4$ leads to $F = 1$ and $J = cos^2(\pi/4) = 1/2$. Given the operating BER_0, a value for σ_0 may be obtained by using the theoretical BER equation (2.106) and tables of the Q-function [24]. For the case of no synchronization errors and operation at $E_s/N_0 = 1/(2\sigma_0^2)$, or $\sigma_0^2 = 1/(2E_s/N_0) = 1/(4E_b/N_0)$, (2.109) becomes

$$P(0;\sigma_0^2) = Q\left(\sqrt{\frac{2E_b}{N_0}}\right). \quad (2.123)$$

BER simulation results for QPSK/4QAM and OQPSK are compared against the theoretical values in figures 2.13 and 2.14 for low to moderate E_b/N_0. Estimation window sizes of $4K$ and $16K$ are shown for $K = 16$. The frequency offset is zero and the modem operates in burst-mode.

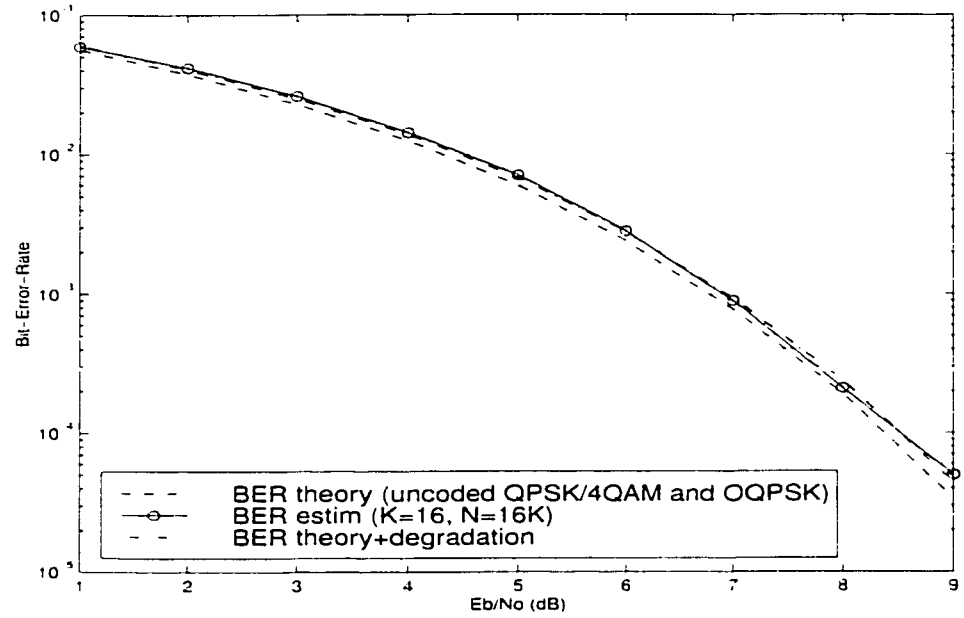

Figure 2.13: BER versus E_b/N_0 for $\widehat{\theta'_{off}}$ with $N = 16K$, $K = 16$, $\theta'_{off} = 0$, $\omega_{off} = 0$ (QPSK/4QAM and OQPSK).

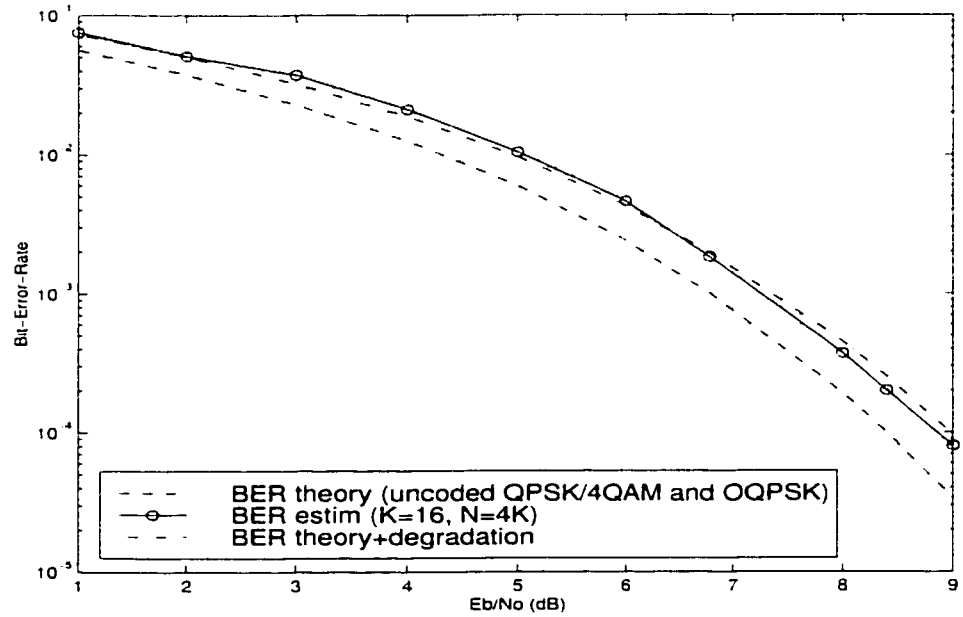

Figure 2.14: BER versus E_b/N_0 for $\widehat{\theta'_{off}}$ with $N = 4K$, $K = 16$, $\theta'_{off} = 0$, $\omega_{off} = 0$ (QPSK/4QAM and OQPSK).

The BER simulations are in line with the predicted BER degradation for both estimation windows, with slightly more performance loss in the case of the shorter window size. The BER degradation is approximately $0.2dB$ to $0.3dB$ for $N = 16K$, which is within the recommended range of $0.2dB$ loss, whereas for $N = 4K$, the E_b/N_0 penalty exceeds the recommended since it ranges from $0.4dB$ to $0.6dB$ [9, Sec. 7.1]. Nevertheless, the degradation is still quite acceptable for QPSK/4QAM and OQPSK. The minor discrepancy between the theoretical and simulation results observed in figure 2.14 from $3dB$ to $6dB$ is attributed to the construction of the matlab simulation model.

Figure 2.15 illustrates the BER degradation for a practical implementation of the synchronizer tested with QPSK/4QAM and OQPSK using $N = 4K$, $K = 16$, $\theta'_{off} = 0$, and $\omega_{off} = 0$. The practical curve closely matches the theoretical one, effecting approximately a $0.7dB$ total degradation (about $0.1dB$ extra loss relative to the theoretical value). This increase may be attributed to the quantization effects related to the fixed-width data paths of the hardware implementation.

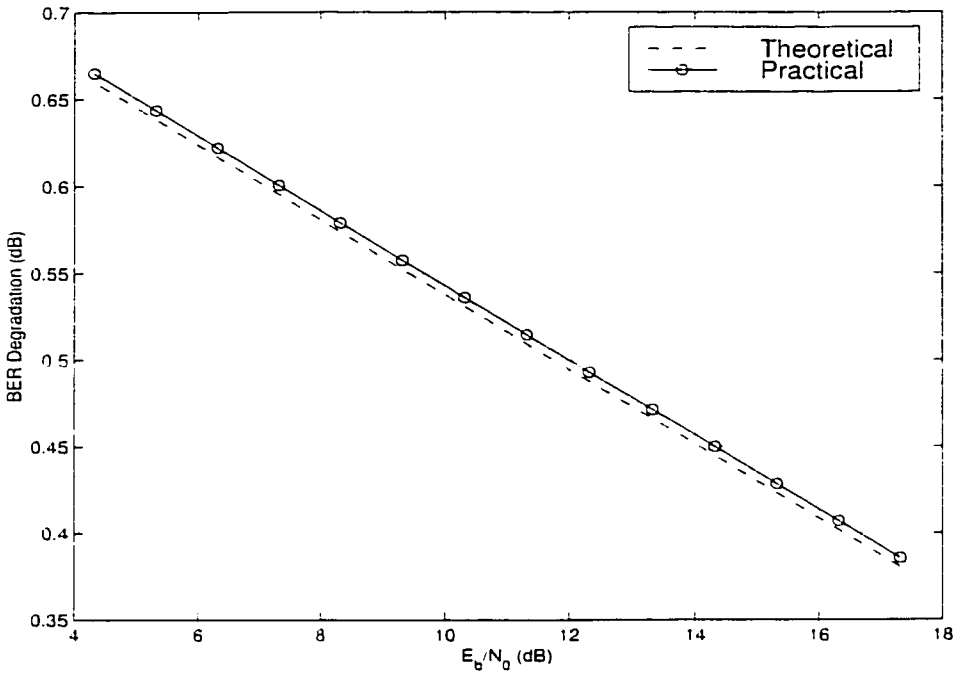

Figure 2.15: Theoretical and Practical BER degradation versus E_b/N_0 with $N = 4K$, $K = 16$, $\theta'_{off} = 0$, $\omega_{off} = 0$ (QPSK/4QAM and OQPSK).

2.5 Implementation Aspects

The proposed phase offset estimator is computationally very efficient and requires little hardware for its implementation. The simple block diagram is shown in figure 2.16.

The in-phase (I) and quadrature (Q) channels are independent of each other, so averaging z_n is equivalent to averaging its real and imaginary components separately. The averaged sums for the two channels following the $1/N$ scaling blocks are presented to the arctangent inputs. The trigonometric function, in turn, determines the corresponding $\widehat{\theta'_{off}}$. Note that scaling by $1/N$ is equivalent to manipulating the bus interconnections if N is an integer power of 2. The designer may choose to remove

the scaling blocks altogether (or adjust the bus connections differently in the case of power-of-2 data paths) since their effect cancels in the arctangent's ratio.

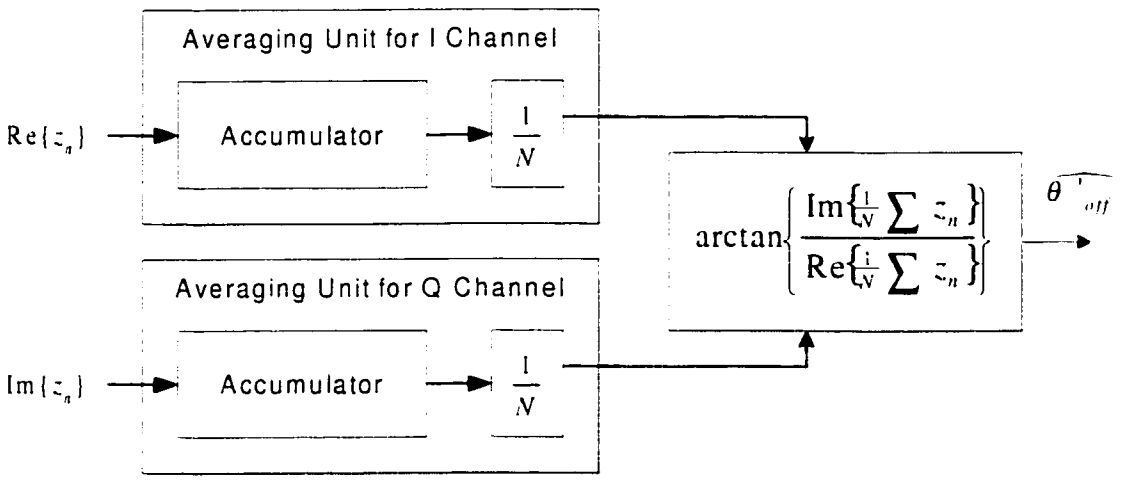

Figure 2.16: Block Diagram of the Phase Offset Estimator.

The averaging functions are simple and fast accumulators, occupying a fraction of the silicon in today's VLSI and FPGA technologies. The heart of the algorithm lies in an efficient implementation of the non-linear arctangent function. Many implementation strategies exist depending on the required arctangent precision, but look-up tables (LUT's) are the most common [25]. Nowadays, the coordinate rotation digital computer (CORDIC) method is gaining much popularity for the hardware implementation of trigonometric and other non-linear functions. Volder first introduced this technique in 1959 [26]. CORDIC is well suited when higher precision is demanded. The method achieves an efficient compromise between silicon area and speed.

For the QPSK/4QAM and OQPSK burst-modem used in this research, 6-bit quantization for the accumulated inputs and the LUT phase values were sufficient to achieve acceptable BER performance. For these small data widths, the LUT approach proved just as economical as CORDIC but was simpler to implement.

To minimize the area occupied by the arctangent read-only memory (ROM), the

rotational symmetry of the $\Re\Im$ plane was exploited. Hence, only the first octant was stored with the insertion of some simple address decoding units to cover the entire $[-\pi, \pi]$ range.

The ROM was pipelined in three levels to reach the 40MHz oversampling requirement and avoids the long path delays normally incurred by a standard combinatorial implementation. The addressing scheme (6 bits for I, 6 bits for Q) concatenates the averaged real and imaginary samples to form a 12-bit bus. The extra address decoding units reduce this bus width to 9 bits so that the LUT retains a manageable size. It is a well-known fact that LUT's double in size for every additional address bit. Consequently, small ROMs are vital in hardware design involving applications with memory.

The phase estimator requires $2N - 2$ real additions for the two accumulators ($N - 1$ for each channel), a scaling function, easily reduced to a shift or bus-connection operation if N is an integer power of 2, and a LUT read operation from the arctangent ROM. The incurred latency equals $N + A$ clock cycles, where A represents the latency of the arctangent module. The algorithm was implemented with $K = 16$ and $N = 4K$. The arctangent module, including the ROM pipelining latency that of the address decoding circuits, required eight sampling clock cycles, for a total latency of $8 + 64 = 72$ cycles. The system was tested with an analog QPSK/4QAM hybrid modem, as well as an OQPSK modem. The BER results of this implementation were shown in figure 2.15 in the form of a BER degradation curve.

The receiver was also equipped with a complete digital phase correction circuitry comprising a 16-bit wide numerically-controlled oscillator (NCO) and an 8-bit wide complex multiplier for the data rotation. The phase correction unit was incorporated after the phase and frequency estimators. Except for the arctangent module already discussed, all data paths occupied 8 lines with maximum precision maintained

throughout in order to minimize the effects of round-off and truncation errors.

The phase estimator, together with the correction, control and decimation units, was implemented using VHDL. The design was synthesized and routed into a Xilinx XC4028EX-3 FPGA. It occupied 632 configurable logic blocks (CLBs), or approximately 23839 equivalent gates. The Xilinx XC4028EX-3 was the part of choice at the start of the research that was both cost effective and flexible enough for prototyping different kinds of designs. Our design can also target other vendors' FPGAs. The implementation achieved sampling rates up to 40 MHz, allowing operation at 5 Mbps, but the modem in question was conditioned to operate at a bit rate of 2 Mbps, requiring only a 16 MHz sampling rate. The stand-alone version of the phase estimator required 228 CLBs (approximately 8596 equivalent gates).

Although a low bit-rate burst-modem was used in order to verify the algorithms, faster operating speeds are achievable by selecting a faster technology and by further pipelining the algorithm. The transmission rates can be increased with higher modulation orders, but reducing number of samples per symbol without altering the sampling frequency has the same effect.

Chapter 3

Autocorrelation-Based Data-Aided Feedforward Frequency Offset Estimation Technique Employing Oversampling

This chapter focuses on the description and performance analysis of the frequency offset estimator used to counter the adverse effects of oscillator discrepancies. The first section presents the technique, while section 3.2 provides an analytical treatment of its moments. Simulations in section 3.3 evaluate the analytical results. A discussion on implementation of the algorithm terminates the chapter.

3.1 Presentation of Frequency Offset Estimation Algorithm

The frequency offset estimator based on oversampling employs the matched filtered samples given by (2.18). The algorithm, although not derived from the ML principle, accumulates a processed version of the observations with the intent to remove the phase offset and retain only the frequency offset. The phase dependence is removed by multiplying the complex samples by a delayed-by-L, conjugated version of themselves, after which averaging is performed. L provides an adjustable means by which the performance may be controlled.

The proposed frequency estimation technique may be interpreted as the sample autocorrelation of the observations, i.e.,

$$\lambda_\ell = \frac{1}{N} \sum_{n=\ell+L}^{\ell+L+N-1} z_n z_{n-L}^* \tag{3.1}$$

where the length N is not necessarily equal to that of the phase estimator, although a common preamble may be employed for both techniques, a direct consequence form the independence of the algorithms.

The purpose of λ_ℓ is to accumulate a multiple L of the true frequency offset so that a more accurate estimate is achieved.

If the definition of z_n given by (2.18) is combined with (2.41), and the noise terms are omitted, the complex product under the summation may be represented as

$$\begin{aligned} z_n z_{n-L}^* = & \left[\exp\left\{j\theta'_{off}\right\} \exp\left\{j\omega_{off} T_{sa} \left(n - \ell - \frac{N-1}{2}\right)\right\}\right. \\ & \left. \cdot H_N\left(\left(n - \ell - \frac{N-1}{2}\right) T_{sa}\right)\right] \\ & \cdot \left[\exp\left\{j\theta'_{off}\right\} \exp\left\{j\omega_{off} T_{sa} \left(n - L - \ell - \frac{N-1}{2}\right)\right\}\right. \end{aligned}$$

$$\cdot H_N\left(\left(n-L-\ell-\frac{N-1}{2}\right)T_{sa}\right)\Big]^{*}. \tag{3.2}$$

Carrying out the conjugation on the second factor and multiplying out all terms, with the knowledge that $H_N(\cdot)$ is real-valued, simplifies (3.2) to

$$\begin{aligned} z_n z_{n-L}^{*} &= \exp\{j\omega_{off}T_{sa}L\} \\ &\quad \cdot H_N\left(\left(n-\ell-\frac{N-1}{2}\right)T_{sa}\right) \\ &\quad \cdot H_N\left(\left(n-L-\ell-\frac{N-1}{2}\right)T_{sa}\right). \end{aligned} \tag{3.3}$$

As we notice from (3.3), the dependence on θ'_{off} has been removed. Remembering that for high signal-to-noise ratio and DA operation with one type of preamble symbol, $H_N(\cdot)$ is approximately constant and equal to a real constant B (see (2.31)). Hence,

$$z_n z_{n-L}^{*} \approx B^2 \exp\{j\omega_{off}T_{sa}L\}. \tag{3.4}$$

The averaging statistic under this new result approximately equals[1]

$$\lambda_\ell \approx \frac{1}{N}\sum_{n=\ell+L}^{\ell+L+N-1} B^2 \exp\{j\omega_{off}T_{sa}L\}. \tag{3.5}$$

All terms under the summation are independent of n. Moving them outside the summation and evaluating the sum over n yields

$$\lambda_\ell = B^2 \exp\{j\omega_{off}T_{sa}L\} \tag{3.6}$$

Taking the argument of (3.6) and dividing the result by the correlation separation reveals that in the absence of noise the algorithm estimates the true frequency offset.

[1]The approximate equality is subsequently replaced by the conventional equality to simplify the notation.

independently of the phase offset, that is,

$$\widehat{\omega_{off}T_{sa}} = \frac{1}{L}\arg\{\lambda_\ell\} \tag{3.7}$$

$$= \frac{1}{L}\arg\left\{B^2\exp\{j\omega_{off}T_{sa}L\}\right\} \tag{3.8}$$

$$= \omega_{off}T_{sa} \tag{3.9}$$

where $\widehat{\omega_{off}T_{sa}}$ denotes the estimated frequency offset normalized to the sampling period. If, instead, we seek ΔfT_{sym}, the frequency offset in Hertz normalized to the symbol period, then the following change of variable is appropriate:

$$\widehat{\Delta fT_{sym}} = \frac{K}{2\pi L}\arg\left\{\frac{1}{N}\sum_{n=\ell+L}^{\ell+L+N-1} z_n z_{n-L}^*\right\} \tag{3.10}$$

$$= \frac{\widehat{\omega_{off}T_{sa}}K}{2\pi}. \tag{3.11}$$

To provide a common basis for comparison with existing methods, $\omega_{off}T_{sa}$ and $\widehat{\omega_{off}T_{sa}}$ are adopted where applicable.

An important remark must be made about the estimator's range. Evidently, the $\arg\{\cdot\}$ function is restricted to $[-\pi, \pi]$, within which there is no phase ambiguity. However, the oversampling factor and the correlation distance limit this range. The unambiguous range of $\widehat{\Delta fT_{sym}}$ is bounded by

$$\left|\widehat{\Delta fT_{sym}}\right| \leq \frac{K}{2L}. \tag{3.12}$$

We now pursue the study of the estimator in the presence of the noise. Rewriting (3.2) to include the complex noise terms γ_n, the sample product evolves into

$$z_n z_{n-L}^* = \left[\exp\left\{j\theta'_{off}\right\}\exp\left\{j\omega_{off}T_{sa}\left(n-\ell-\frac{N-1}{2}\right)\right\}\right.$$

$$\cdot H_N\left(\left(n-\ell-\frac{N-1}{2}\right)T_{sa}\right)+\gamma_n\Big]$$
$$\cdot\left[\exp\left\{-j\theta'_{off}\right\}\exp\left\{-j\omega_{off}T_{sa}\left(n-L-\ell-\frac{N-1}{2}\right)\right\}\right.$$
$$\left.\cdot H_N\left(\left(n-L-\ell-\frac{N-1}{2}\right)T_{sa}\right)+\gamma^*_{n-L}\right]. \tag{3.13}$$

Expanding the product generates the following four complex-valued terms, where (2.31) was implicitly substituted:

$$\begin{aligned}
z_n z^*_{n-L} &= \exp\{j\omega_{off}T_{sa}L\}\,H_N\left(\left(n-\ell-\frac{N-1}{2}\right)T_{sa}\right)\\
&\quad\cdot H_N\left(\left(n-L-\ell-\frac{N-1}{2}\right)T_{sa}\right)\\
&\quad+\gamma^*_{n-L}\exp\left\{j\theta'_{off}\right\}\exp\left\{j\omega_{off}T_{sa}\left(n-\ell-\frac{N-1}{2}\right)\right\}\\
&\quad\cdot H_N\left(\left(n-\ell-\frac{N-1}{2}\right)T_{sa}\right)\\
&\quad+\gamma_n\exp\left\{-j\theta'_{off}\right\}\exp\left\{-j\omega_{off}T_{sa}\left(n-L-\ell-\frac{N-1}{2}\right)\right\}\\
&\quad\cdot H_N\left(\left(n-L-\ell-\frac{N-1}{2}\right)T_{sa}\right)\\
&\quad+\gamma_n\gamma^*_{n-L} \qquad (3.14)\\
&= B^2\exp\{j\omega_{off}T_{sa}L\}\\
&\quad+B\gamma^*_{n-L}\exp\left\{j\theta'_{off}\right\}\exp\left\{j\omega_{off}T_{sa}\left(n-\ell-\frac{N-1}{2}\right)\right\}\\
&\quad+B\gamma_n\exp\left\{-j\theta'_{off}\right\}\exp\left\{-j\omega_{off}T_{sa}\left(n-L-\ell-\frac{N-1}{2}\right)\right\}\\
&\quad+\gamma_n\gamma^*_{n-L}. \qquad (3.15)
\end{aligned}$$

The averaging statistic now equals

$$\begin{aligned}
\lambda_\ell &= \frac{1}{N}\sum_{n=\ell+L}^{\ell+L+N-1}B^2\exp\{j\omega_{off}T_{sa}L\}\\
&\quad+\frac{1}{N}\sum_{n=\ell+L}^{\ell+L+N-1}B\gamma^*_{n-L}\exp\left\{j\theta'_{off}\right\}\exp\left\{j\omega_{off}T_{sa}\left(n-\ell-\frac{N-1}{2}\right)\right\}
\end{aligned}$$

$$+\frac{1}{N}\sum_{n=\ell+L}^{\ell+L+N-1} B\gamma_n \exp\left\{-j\theta'_{off}\right\}\exp\left\{-j\omega_{off}T_{sa}\left(n-L-\ell-\frac{N-1}{2}\right)\right\}$$

$$+\frac{1}{N}\sum_{n=\ell+L}^{\ell+L+N-1}\gamma_n\gamma^*_{n-L} \tag{3.16}$$

$$= B^2\exp\left\{j\omega_{off}T_{sa}L\right\} + degradation(\omega_{off},\gamma_n,\gamma^*_{n-L}). \tag{3.17}$$

The averaging statistic in (3.16) and (3.17) contains the deterministic portion of the transmitted preamble, but it is corrupted by signal-noise cross-terms as well as cross-noise terms. Hence, it becomes difficult to manipulate (3.16) into a more workable expression. It is not clear from this equation how the correlated noise affects the estimator, so an approximate moment study is carried out analytically in the next section. Simulations are used later to determine the estimator's variance.

3.2 Analytical Study of the Frequency Estimator Statistics

3.2.1 Cramér-Rao Lower Bound for Frequency Offset Estimation

Following the same explanations presented for the CRLB of phase estimators, the CRLB applied to frequency estimation of a complex sinusoid in AWGN also considers an unmodulated carrier [19] and is given by

$$\sigma^2_{\widehat{\Delta f}}T^2_{sym} \geq \frac{6}{N(N^2-1)(E_s/N_0)} \tag{3.18}$$

where $\widehat{\Delta f}$ is the frequency offset in Hertz, N is the number of independent samples in the estimation window, E_s/N_0 is the average symbol-energy-to-noise ratio, and T_{sym} is the symbol period.

For QPSK/4QAM and OQPSK, $E_s = 2E_b$ so that the CRLB equals

$$\sigma^2_{\widehat{\Delta f}} T^2_{sym} \geq \frac{6}{N(N^2-1)(2E_b/N_0)}. \tag{3.19}$$

3.2.2 Mean of Frequency Offset Estimator by Analysis

Using the averaging statistic of (3.1) as our starting point, the mean of $\widehat{\omega_{off}}$ normalized to the sampling period may be expressed as

$$\begin{aligned} E\left[\widehat{\omega_{off}} T_{sa}\right] &= E\left[\frac{1}{L}\arg\{\lambda_\ell\}\right] && (3.20)\\ &= E\left[\frac{1}{L}\arg\left\{\frac{1}{N}\sum_{n=\ell+L}^{\ell+L+N-1} z_n z^*_{n-L}\right\}\right] && (3.21)\\ &= E\left[\frac{1}{L}\arg\left\{\frac{1}{N}\sum_{n=\ell+L}^{\ell+L+N-1} x_n + jy_n\right\}\right] && (3.22) \end{aligned}$$

where the observations contain the signal portion in the presence of noise. The substitution

$$z_n z^*_{n-L} = x_n + jy_n \tag{3.23}$$

was used in (3.22). By definition,

$$x_n = \Re\left\{z_n z^*_{n-L}\right\} \tag{3.24}$$

$$y_n = \Im\left\{z_n z^*_{n-L}\right\}. \tag{3.25}$$

If the signal-to-noise ratio is high and $\omega_{off} \ll 1$, then $\sum_n y_n \ll \sum_n x_n$, and $\arg\{\cdot\}$ takes on small values. Therefore, expectation and argument may be interchanged in

(3.22). This yields

$$E\left[\widehat{\omega_{off}}T_{sa}\right] = \frac{1}{L}\arg\left\{E\left[\frac{1}{N}\sum_{n=\ell+L}^{\ell+L+N-1} x_n + jy_n\right]\right\} \tag{3.26}$$

$$= \frac{1}{L}\arg\left\{\frac{1}{N}\sum_{n=\ell+L}^{\ell+L+N-1} E\left[x_n + jy_n\right]\right\} \tag{3.27}$$

$$= \frac{1}{L}\arg\left\{\frac{1}{N}\sum_{n=\ell+L}^{\ell+L+N-1} E\left[z_n z_{n-L}^*\right]\right\}. \tag{3.28}$$

It is now possible to manipulate (3.28) with the use of (3.16). Considering $E\left[z_n z_{n-L}^*\right]$ alone, and substituting (3.16) for $z_n z_{n-L}^*$ leads to

$$\begin{aligned} E\left[z_n z_{n-L}^*\right] = E\Bigg[& \frac{1}{N}\sum_{n=\ell+L}^{\ell+L+N-1} B^2 \exp\left\{j\omega_{off}T_{sa}L\right\} \\ & + \frac{1}{N}\sum_{n=\ell+L}^{\ell+L+N-1} B\gamma_{n-L}^* \exp\left\{j\theta'_{off}\right\} \exp\left\{j\omega_{off}T_{sa}\left(n-\ell-\frac{N-1}{2}\right)\right\} \\ & + \frac{1}{N}\sum_{n=\ell+L}^{\ell+L+N-1} B\gamma_n \exp\left\{-j\theta'_{off}\right\} \exp\left\{-j\omega_{off}T_{sa}\left(n-L-\ell-\frac{N-1}{2}\right)\right\} \\ & + \frac{1}{N}\sum_{n=\ell+L}^{\ell+L+N-1} \gamma_n\gamma_{n-L}^*\Bigg]. \end{aligned} \tag{3.29}$$

The first term in (3.29) is a deterministic quantity so the expectation has no effect on it. Thus, it can be rewritten with the expectation removed.

The second term comprises four sub-terms resulting from carrying out the complex multiplication. Letting

$$s_n = B\exp\left\{j\theta'_{off}\right\}\exp\left\{j\omega_{off}T_{sa}\left(n-\ell-\frac{N-1}{2}\right)\right\} \tag{3.30}$$

and

$$\gamma_n = \gamma_{In} + j\gamma_{Qn} \tag{3.31}$$

and carrying out the complex multiplications in the second term under the expectation in (3.29), we obtain

$$\begin{aligned} term\ 2 \;=\; & E\left[B\cos\left(\theta'_{off}+\omega_{off}T_{sa}\left(n-\ell-\frac{N-1}{2}\right)\right)\gamma_{In-L}\right] \\ & +E\left[B\sin\left(\theta'_{off}+\omega_{off}T_{sa}\left(n-\ell-\frac{N-1}{2}\right)\right)\gamma_{Qn-L}\right] \\ & -jE\left[B\cos\left(\theta'_{off}+\omega_{off}T_{sa}\left(n-\ell-\frac{N-1}{2}\right)\right)\gamma_{Qn-L}\right] \\ & +jE\left[B\sin\left(\theta'_{off}+\omega_{off}T_{sa}\left(n-\ell-\frac{N-1}{2}\right)\right)\gamma_{In-L}\right]. \end{aligned} \tag{3.32}$$

The expectation operates exclusively on the γ_{In-L} and γ_{Qn-L} factors, the only random quantities in *term* 2. Since the noise components are zero-mean, and they are also independent of the signal, *term* 2 reduces to zero. Similarly to *term* 2, *term* 3 equals zero.

Expanding the fourth term produces

$$\begin{aligned} term\ 4 \;=\; & E\left[\gamma_{In}\gamma_{In-L}\right]+E\left[\gamma_{Qn}\gamma_{Qn-L}\right] \\ & -jE\left[\gamma_{In}\gamma_{Qn-L}\right]+jE\left[\gamma_{In-L}\gamma_{Qn}\right]. \end{aligned} \tag{3.33}$$

In-phase and quadrature noise terms are independent of each other by construction of the equivalent complex baseband signal model. Applying the theory of independent random variables to (3.33), the last two expectations can be separated and ultimately equated to zero, since the noise components are zero-mean and vanish under the expectation operator. In other words,

$$E\left[\gamma_{In}\gamma_{Qn-L}\right] = E\left[\gamma_{In}\right]\cdot E\left[\gamma_{Qn-L}\right] \tag{3.34}$$

$$= 0 \tag{3.35}$$

$$E\left[\gamma_{In-L}\gamma_{Qn}\right] = E\left[\gamma_{In-L}\right]\cdot E\left[\gamma_{Qn}\right] \tag{3.36}$$

$$= 0. \tag{3.37}$$

and only the autocorrelation functions of γ_{In} and γ_{Qn} remain in *term* 4, i.e.,

$$term\ 4 \;=\; R_{\gamma_I}(L) + R_{\gamma_Q}(L). \tag{3.38}$$

Appropriately selecting L as integer multiples p ($p > 0$) of the oversampling factor K drives $R_{\gamma_I}(L)$ and $R_{\gamma_Q}(L)$ in *term* 4 to zero at these time instants. Hence,

$$E\left[z_n z_{n-L}^*\right] \;=\; B^2 \exp\{jL\omega_{off}T_{sa}\} \tag{3.39}$$

Substituting (3.39) into (3.28) yields

$$E\left[\widehat{\omega_{off}}T_{sa}\right] \;=\; \frac{1}{L}\arg\left\{\frac{1}{N}\sum_{n=\ell+L}^{\ell+L+N-1} B^2 \exp\{jL\omega_{off}T_{sa}\}\right\} \tag{3.40}$$

$$\;=\; \frac{1}{L}\arg\left\{B^2 \exp\{jL\omega_{off}T_{sa}\}\right\} \tag{3.41}$$

$$\;=\; \frac{1}{L}\, L\, \omega_{off}T_{sa} \tag{3.42}$$

$$\;=\; \omega_{off}T_{sa}. \tag{3.43}$$

Equation (3.43) indicates that $\widehat{\omega_{off}}$ is unbiased.

The estimation range of $\widehat{\omega_{off}}T_{sa}$ is bounded by (see (3.39))

$$|\widehat{\omega_{off}}T_{sa}L| \le \pi. \tag{3.44}$$

or,

$$\left|2\pi L\, \widehat{\Delta f}\frac{T_{sym}}{K}\right| \le \pi. \tag{3.45}$$

which readily reduces to

$$\left|\widehat{\Delta f}T_{sym}\right| \le \frac{K}{2L}. \tag{3.46}$$

Hence, the estimate is unbiased when (3.46) is satisfied.

3.2.3 Variance of Frequency Offset Estimator by Analysis

The derivation of an approximate formula for the variance of $\widehat{\omega_{off}}$ begins with the general definition for the variance.

$$var\left[\widehat{\omega_{off}}T_{sa}\right] = E\left[(\widehat{\omega_{off}}T_{sa})^2\right] - \left(E\left[\widehat{\omega_{off}}T_{sa}\right]\right)^2 \tag{3.47}$$

$$= E\left[(\widehat{\omega_{off}}T_{sa})^2\right] - (\omega_{off}T_{sa})^2 \tag{3.48}$$

where the substitution in the last term is a direct consequence of (3.43). Without loss of generality, θ'_{off} is assumed zero ($\widehat{\omega_{off}}$ is independent of θ'_{off}).

Under the condition of small frequency offsets and high signal-to-noise ratios, the second moment of $\widehat{\omega_{off}}T_{sa}$ (first term in (3.48)) is easily approximated as outlined in [27] and [28]. Pursuing the method detailed in those two papers, the imaginary part y_n is zero-mean and the variances of both the real and imaginary components of (3.23) are small vis-à-vis the squared real mean. Consequently, $\sum_n y_n \ll \sum_n x_n$ holds for (3.22) and $\arg\{\cdot\}$ may be replaced by its small angle approximation. For high signal-to-noise ratios, $\frac{1}{N}\sum_n x_n \approx B^2$, where, as before, B is a real constant close to unity. To simplify the notation, B is arbitrarily set to unity.

The second moment of $\widehat{\omega_{off}}T_{sa}$ approximately equals

$$E\left[(\widehat{\omega_{off}}T_{sa})^2\right] = E\left[\left(\frac{1}{(LN)}\sum_{n=\ell+L}^{\ell+L+N-1} y_n\right)^2\right] \tag{3.49}$$

$$= \frac{1}{(LN)^2}E\left[\sum_{n=\ell+L}^{\ell+L+N-1}\sum_{m=\ell+L}^{\ell+L+N-1} y_n y_m\right]. \tag{3.50}$$

Deferring the lengthy mathematical details to appendix A. (3.50) results in

$$
\begin{aligned}
E\left[(\widehat{\omega_{off}}T_{sa})^2\right] &= \frac{1}{(LN)^2}\left\{2\left(NR(0)+2\sum_{m=1}^{N-1}(N-m)R(m)\right)\right. \\
&\quad -2\left(NR(L)+\sum_{m=1}^{N-1}(N-m)\left[R(|m-L|)+R(|m+L|)\right]\right) \\
&\quad +2\left(NR^2(0)+2\sum_{m=1}^{N-1}(N-m)R^2(m)\right) \\
&\quad \left.+2\left[2\left(NR(L)+\sum_{m=1}^{N-1}(N-m)\left[R(|m-L|)+R(|m+L|)\right]\right)\right]^2\right\}
\end{aligned}
\tag{3.51}
$$

where $R(m)$ represents the noise autocorrelation function in each channel. It has already been assumed that the in-phase and quadrature channels behave similarly. Equation (3.51) bears no resemblance to the CRLB for frequency estimation even when the noise is AWGN. However, the approximated expression for the variance is seemingly proportional to $1/L^2$, although some opposite effects directly dependent on L may be implied in the numerator terms ($R(n)$ depends on L for some terms). The overall effect may be approximately proportional to $1/L$ rather than $1/L^2$. Simulations evaluate the true behavior of the frequency estimator's variance in the next section.

As a note, to obtain $E\left[(\Delta f T_{sym})^2\right]$, one simply needs to multiply the right hand side of (3.51) by $\left(\frac{K}{2\pi}\right)^2$ (see the substitution in (3.11)).

3.3 Performance Evaluation of Frequency Offset Estimator by Simulation

3.3.1 Probability Density Function of Frequency Offset Estimator

As in the case of the phase offset algorithm, the *pdf* of the frequency error estimator is now studied to gain some insight on the distribution of the estimator statistics.

As a first step in the analysis, the effect of oversampling is presented. Figure 3.1 illustrates the cases for K taking on values of 2, 4 and 16 samples per symbol with $\Delta f = 0$.

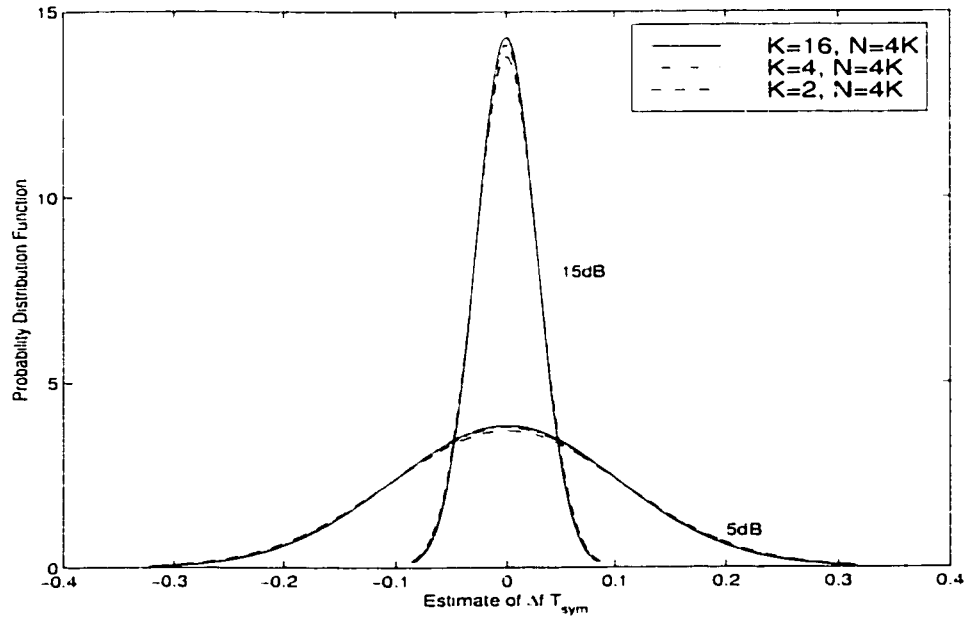

Figure 3.1: Effect of K on the *pdf* of $\widehat{\Delta f T_{sym}}$ (QPSK/4QAM and OQPSK).

The spread of the curves depends on the signal-to-noise ratio but is marginally affected as K varies. A similar behavior was observed with the phase estimator in the previous chapter. $\widehat{\Delta f T_{sym}}$ is Gaussian distributed and the estimates are independent

of each other so that only the mean and the variance are required to fully describe its statistics. Also, the *pdf* is centered at the true phase offset $\Delta f T_{sym}$, in this case, it is zero. This was also verified for non-zero $\Delta f T_{sym}$ satisfying (3.12).

On the other hand, the number of observations N does affect the statistical properties of the frequency error estimate. For instance, in figures 3.2 and 3.3, a larger N concentrates the *pdf* closer to the true frequency error. Consequently, the variance diminishes.

For practical purposes, a window of $4K$ samples leads to a small estimator, but produces somewhat coarse estimates, whereas $16K$ samples is suited for better estimates at the expense of an additional computational burden.

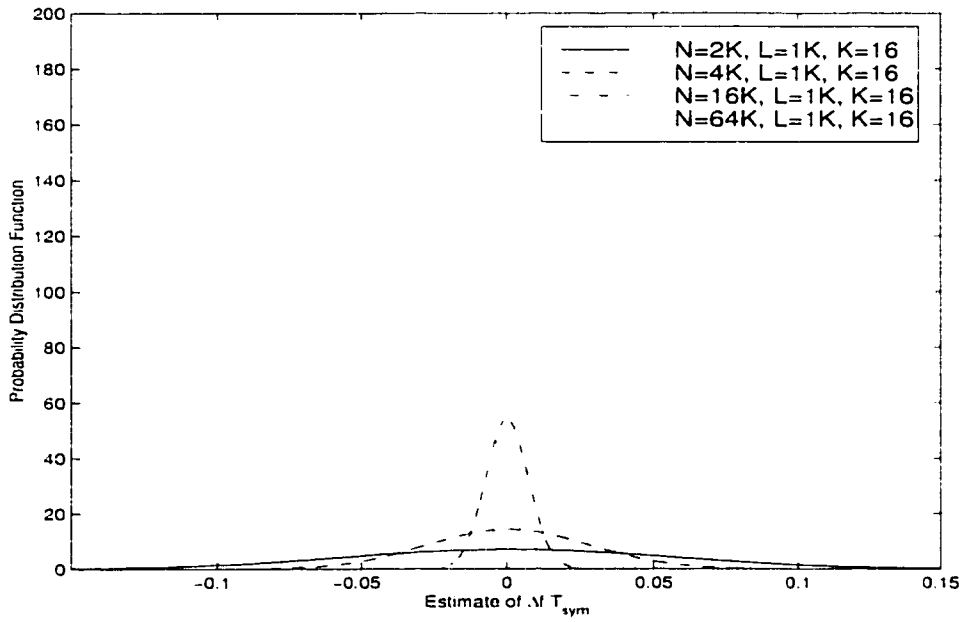

Figure 3.2: Effect of N on the *pdf* of $\widehat{\Delta f T_{sym}}$. $E_b/N_0 = 15dB$ (QPSK/4QAM and OQPSK).

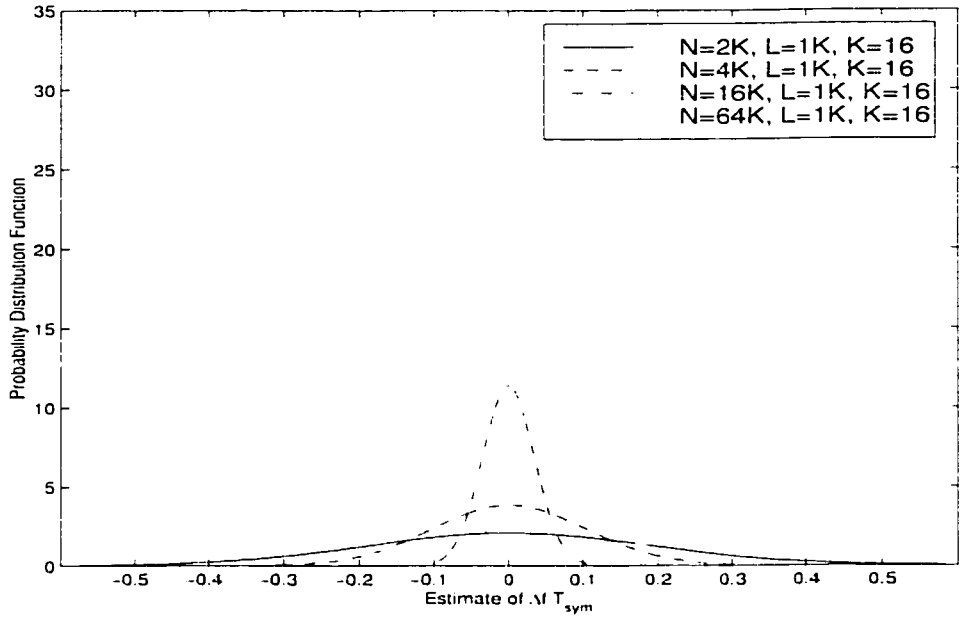

Figure 3.3: Effect of N on the *pdf* of $\widehat{\Delta f T_{sym}}$. $E_b/N_0 = 5dB$ (QPSK/4QAM and OQPSK).

A third degree of freedom to control the frequency estimator's performance is L, the correlation distance between samples. So far, figures 3.1, 3.2 and 3.3 displayed results when L was fixed at one symbol interval, i.e., $L = 1K$ samples. It was seen from (3.43) that an unbiased estimate was possible as long as L equaled a positive integer multiple of K. Figures 3.4 and 3.5 depict the *pdf* for $L = 1K$, $5K$, $9K$, and $15K$ samples. The advantages of parametrizing the correlation separation are apparent in these two figures, in which the *pdf* sharpens itself around the mean as L widens. This is anticipated from (3.51).

However, for each advantage gained an opposite disadvantage appears. Increasing L too much narrows the estimation range proportionally. Hence, a compromise must be reached between the estimation range and the desired accuracy. Simulation studies regarding this topic follow in the next two sections.

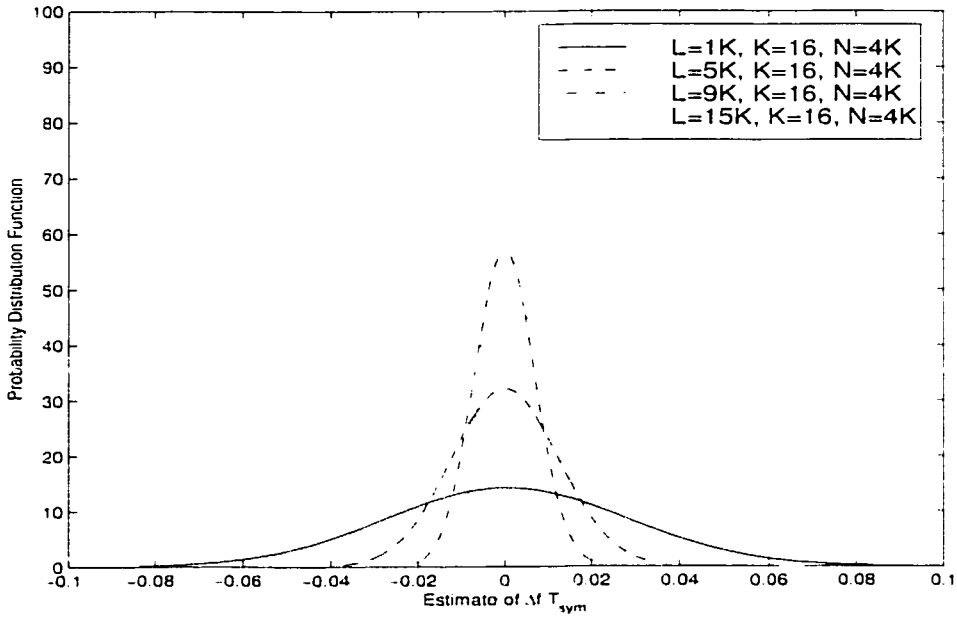

Figure 3.4: Effect of L on the *pdf* of $\widehat{\Delta f T_{sym}}$, $E_b/N_0 = 15dB$ (QPSK/4QAM and OQPSK).

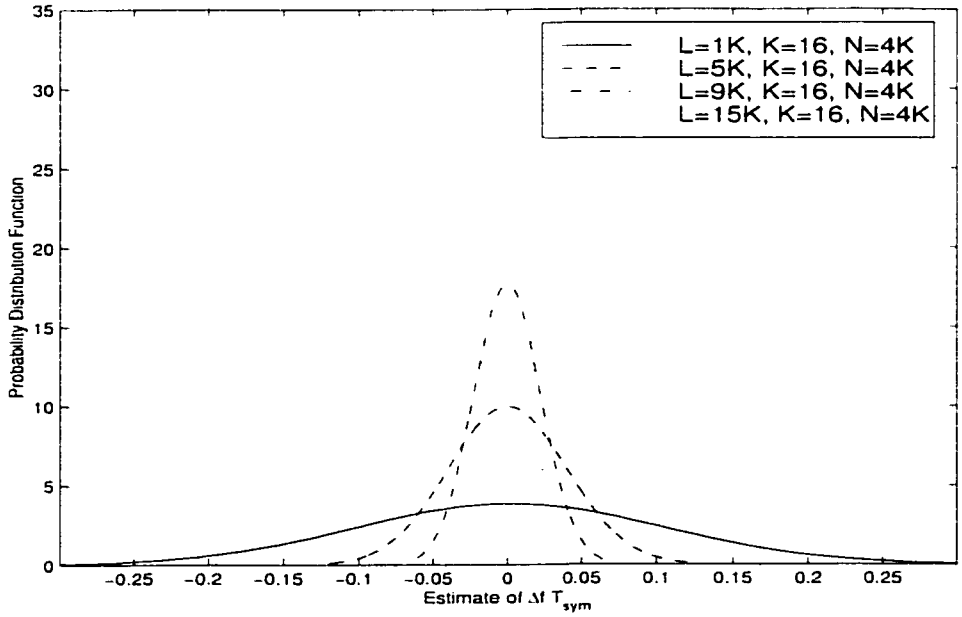

Figure 3.5: Effect of L on the *pdf* of $\widehat{\Delta f T_{sym}}$, $E_b/N_0 = 5dB$ (QPSK/4QAM and OQPSK).

3.3.2 Mean of Frequency Offset Estimator by Simulation

Founded on the results of the previous section, the mean of $\widehat{\Delta f T_{sym}}$ barely depends on K and simulations of the mean verify that this is indeed the case. For this reason, they are excluded from this section.

The bias introduced by N and L is analyzed in this section using simulations. The results for $E_b/N_0 = 5dB$ and $K = 16$ are shown in figures 3.6 and 3.7. Clearly, from figure 3.6, increasing N indeed reduces the bias at the $\Delta f T_{sym} = \pm\frac{K}{2L}$ foldover points, but cannot completely eliminate it unless N is excessively large. The estimator inherits its modulo-$(1/2)$ behavior from the arctangent function ($L = 1K$), as did the phase estimator with its modulo-2π behavior. Nonetheless, $\widehat{\Delta f T_{sym}}$ remains unbiased for the majority of $[-\frac{K}{2L}, \frac{K}{2L}]$.

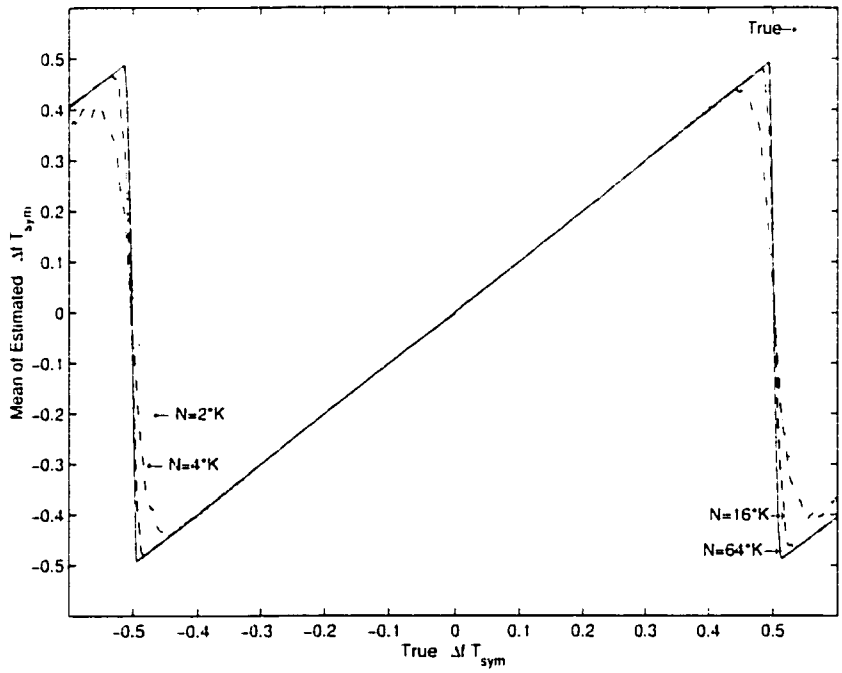

Figure 3.6: Effect of N on the Mean of $\widehat{\Delta f T_{sym}}$ versus the True Frequency Offset: $K = 16$, $L = 1K$, $E_b/N_0 = 5dB$ (QPSK/4QAM and OQPSK).

The plots in figure 3.7 exemplify the decrease in the estimation range of $\widehat{\Delta f T_{sym}}$ as L is augmented. The modulo-$\frac{K}{2L}$ behavior is clearly noted for different L. When $L = 1K$, the estimation range is maximized and the algorithm remains unbiased for the full range of frequency offsets (modulo-$\frac{1}{2}$ behavior). However, when L is increased to $2K$ and $5K$, the estimation range is reduced proportionally. If the true offset never exceeds a given (approximately known) maximum threshold, the designer should very well select from (3.46) the lowest possible value for L that avoids cycle slips during the correction process.

The next subsection demonstrates the performance improvement in the estimator's variance by increasing L.

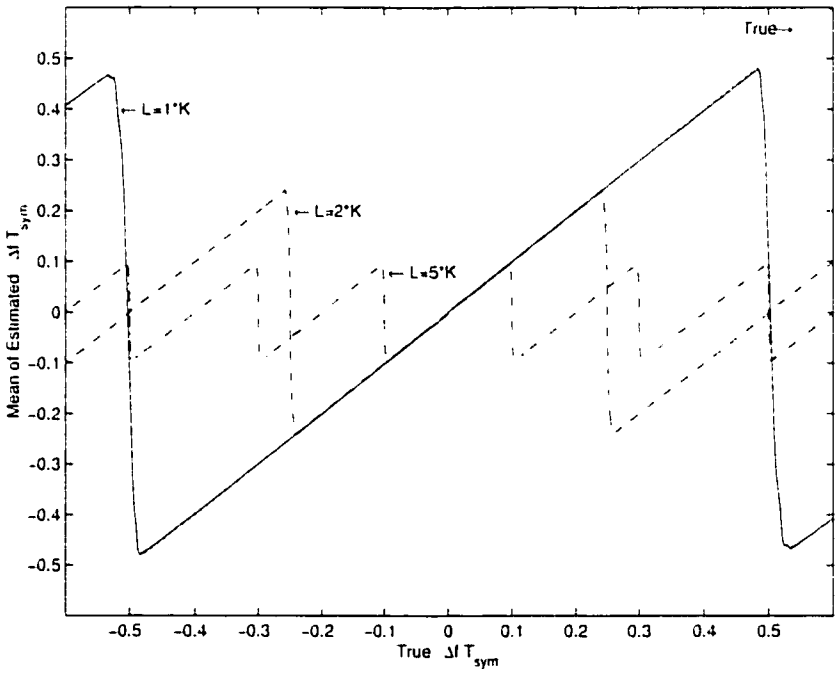

Figure 3.7: Effect of L on the Mean of $\widehat{\Delta f T_{sym}}$ versus the True Frequency Offset: $K = 16$, $N = 16K$, $E_b/N_0 = 5dB$ (QPSK/4QAM and OQPSK).

3.3.3 Variance of Frequency Offset Estimator by Simulation

The variance of $\widehat{\Delta f T_{sym}}$ depends strictly on the estimation window length and the correlation separation between samples, since oversampling by K had negligible influence. This section qualitatively explores the compromise that must be met between the two parameters, based on the anticipated maximum frequency deviation.

The effect of N is examined first. In the discussion to follow, the phase offset is set to zero. Figure 3.8 illustrates the variance of $\widehat{\Delta f T_{sym}}$ versus N for $\Delta f = 0$ and $L = 1K$.

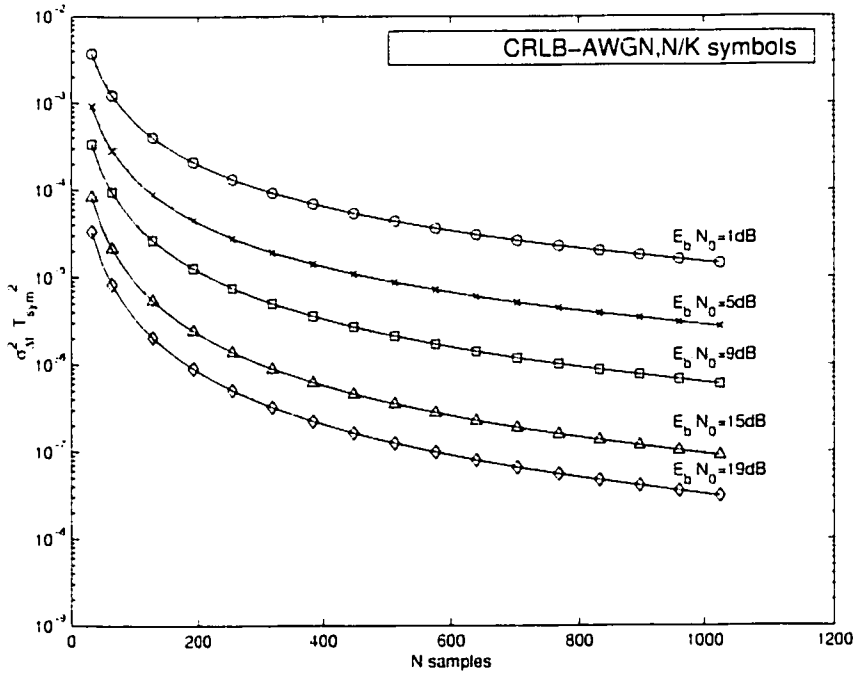

Figure 3.8: Variance of $\widehat{\Delta f T_{sym}}$ versus N for $\Delta f T_{sym} = 0$, $L = 1K$, $K = 16$ (QPSK/4QAM and OQPSK).

Although the variance of the estimate decreases steadily for moderate to high E_b/N_0, it distances itself from the AWGN CRLB as the observation window increases[2].

[2][9, Ch. 8] shows that the ML estimator of $\Delta f T_{sym}$ based on one sample per symbol is achieved with a correlation interval equal to a unit symbol interval. Although increasing the correlation

A similar behavior is observed for all E_b/N_0 considered.

Even though the performance of the simple autocorrelation-based open-loop frequency offset estimator does not compare favorably to the CRLB, its variance can benefit by adjusting L. Referring to figures 3.9 through 3.12, larger L, i.e., greater correlation separation between samples, reduces the variance. Intuitively, increasing L reduces the correlation of the dependent noise samples, so they behave more and more as independent random variables (refer to (3.51)). The time-averaging operation can then more effectively filter out their effect on estimation.

The influence of L on the variance is demonstrated for four different cases of N in figures 3.9 through 3.12. The results are quite promising for the considered quantities of E_b/N_0. For instance, when $N = 4K$, $K = 16$ and $E_b/N_0 = 9dB$ (figure 3.10), increasing L from $L = 1K = 16$ samples (1-symbol correlation separation) to $L = 3K = 48$ samples (3-symbol correlation separation) achieves a decade of improvement in the estimator's variance, while unambiguously operating over a wide frequency range equal to $\frac{K}{2(3K)} = (1/6)f_{sym}$, (approximately 17% of the symbol rate). Similar results are also witnessed for the other window sizes and operating E_b/N_0.

The true benefits of adjusting the correlation gap are apparent when the offset to be estimated takes on small values. This case occurs frequently in practice in fixed-user topologies, for which frequency offsets arise from oscillator imperfections.

distance improves the variance of the algorithm (with respect to the CRLB for the 1K symbol distance), the estimator should no longer be categorized as ML. Nevertheless, the CRLB, although no longer directly applicable to these cases, can still be used as a reference for comparison.

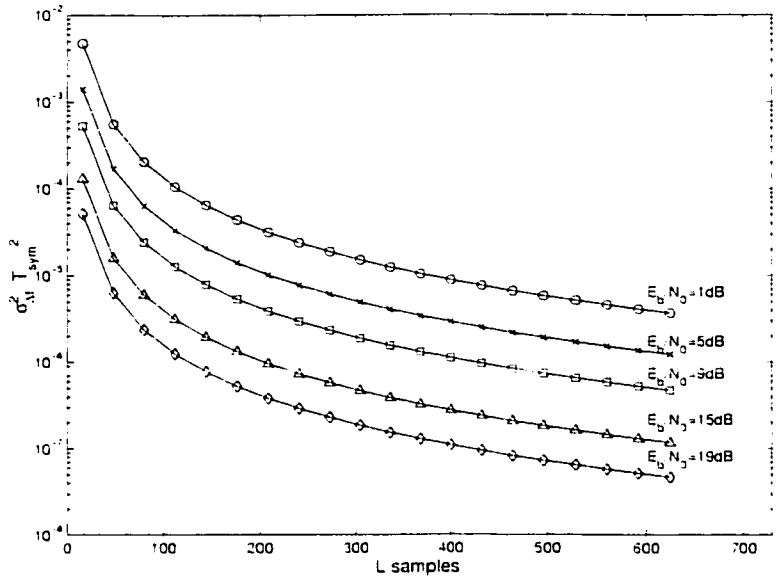

Figure 3.9: Variance of $\widehat{\Delta f T_{sym}}$ versus L for $\Delta f T_{sym} = 0$, $N = 2K$, $K = 16$ (QPSK/4QAM and OQPSK).

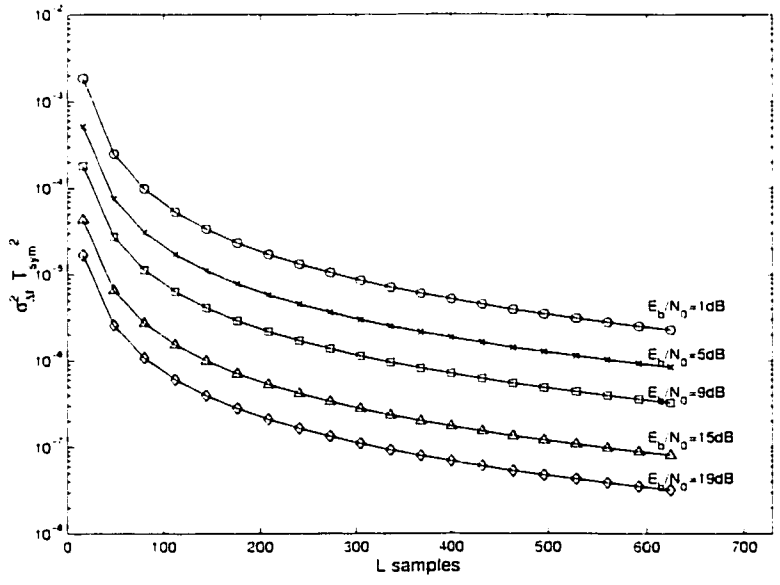

Figure 3.10: Variance of $\widehat{\Delta f T_{sym}}$ versus L for $\Delta f T_{sym} = 0$, $N = 4K$, $K = 16$ (QPSK/4QAM and OQPSK).

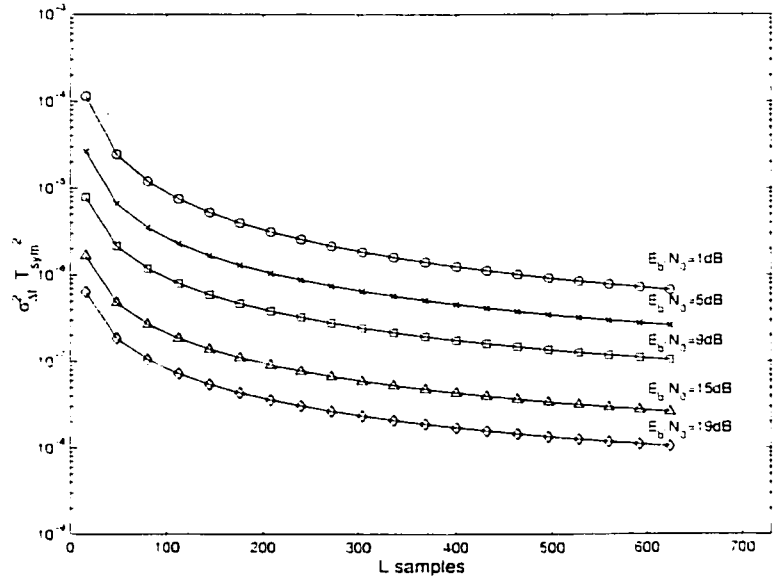

Figure 3.11: Variance of $\widehat{\Delta f T_{sym}}$ versus L for $\Delta f T_{sym} = 0$, $N = 16K$, $K = 16$ (QPSK/4QAM and OQPSK).

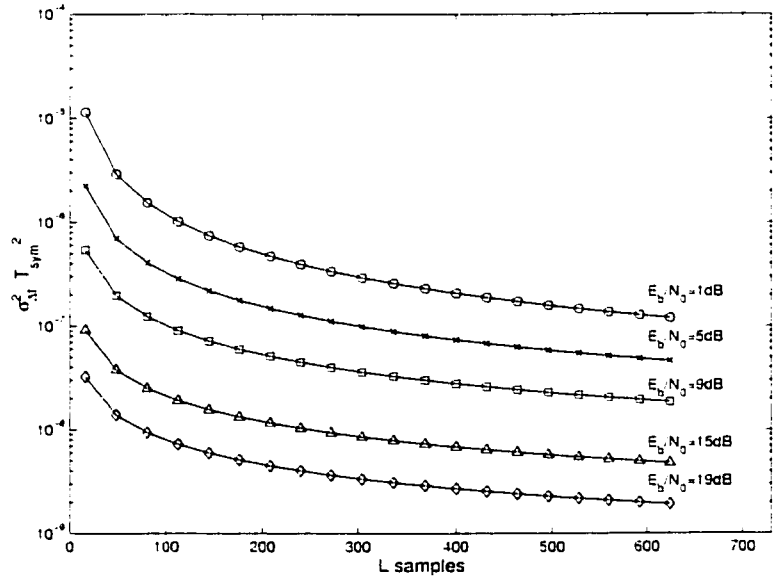

Figure 3.12: Variance of $\widehat{\Delta f T_{sym}}$ versus L for $\Delta f T_{sym} = 0$, $N = 64K$, $K = 16$ (QPSK/4QAM and OQPSK).

3.4 Implementation Aspects

The practical implementation considerations associated with the proposed frequency estimator begin with the block diagram in figure 3.13. The technique is suitable for a fixed-point hardware realization using an FPGA test bed.

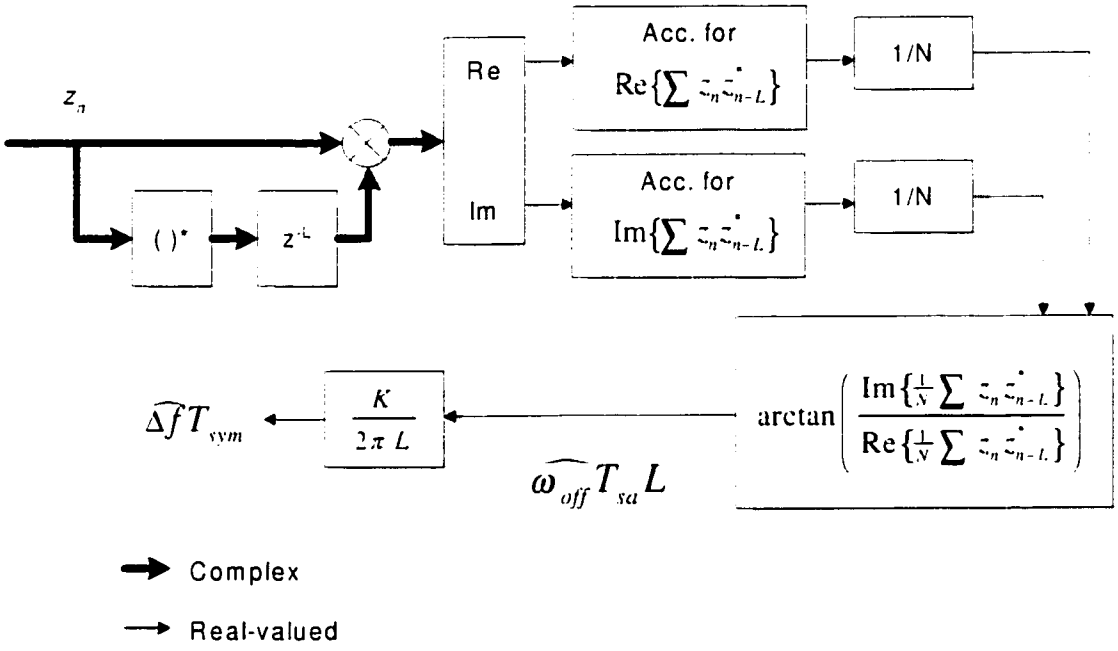

Figure 3.13: Block Diagram of the Frequency Offset Estimator.

The complex-valued correlation circuit multiplies the incoming samples with a delayed, complex-conjugated version of themselves before feeding them to the accumulators. The arctangent module returns the phase associated with the averaged complex sum at the output of the accumulator-scaling blocks. Finally, the result is scaled by $\frac{K}{2\pi L}$ to yield $\widehat{\Delta f} T_{sym}$. Once the estimate is determined, the NCO and complex rotator correct the optimal payload symbol sample at the symbol rate.

The frequency offset recovery algorithm requires N complex products for the correlation section, equivalent to $4N$ real products and $2N$ additions. The correlator also necessitates L unit delays.

Because the input data sequence is complex-valued, the output of the complex multiplier is also complex-valued, thus requiring 2 accumulators working in parallel to sum the N correlation results. Hence, an extra $2N-2$ additions are needed. The $1/N$ blocks scale the sums, but may be removed entirely since they cancel in the arctangent operation. An arctangent ROM calculates the argument of the complex-valued result. Other possibilities include the use of the CORDIC algorithm [25, 26] in place of a LUT, or, if the frequency offset is expected to be small, the approximation $\arctan(y/x) \approx y/x$. The latter was used in the hardware implementation since it was simple and required little silicon. Final scaling by $\frac{K}{2\pi L}$ generates the required estimate normalized to the symbol interval.

From the viewpoint of a hardware implementation employing the LUT approach, the arctangent ROM is designed to lump $\frac{K}{2\pi L}$ with the arctangent values. Because the final result is already normalized by 2π, this simplifies the NCO's internal accumulation operations. Furthermore, picking N, L and K as integer powers of 2 reduces the scaling operations to simple shift operations or bus connections and further reduces the associated hardware complexity.

The frequency estimator with $N = 4K = 64$ and $L = K = 16$ was implemented in VHDL and consumed 474 CLBs (17871 equivalent gates) in a Xilinx XC4028EX-3 FPGA. Inputs were 8 bits wide, while most of the internal operations were carried out using 16 bits to preserve the greatest accuracy. The latency of the circuit was 112 clock cycles. The complete design, comprising the phase and frequency estimators, the NCO and the complex rotator (which was shared with the frequency estimator) utilized 844 CLBs (31822 equivalent gates) with an overall 126 clock cycle latency. The maximum sampling speed achieved by the complete digital FF recovery system including both carrier recovery schemes, the data correction circuitry and the control unit, was 33 MHz, i.e. 4.125 Mbps for QPSK/4QAM and OQPSK. A substantial

increase in the system throughput may be achieved by applying the same solutions as those suggested at the end of section 2.5

Briefly, the frequency estimator pursued in this chapter, although not achieving the CRLB, emphasized numerous implementation advantages over other techniques, relative to size and speed.

Chapter 4

Analysis of an All-Digital Decision-Directed Feedback Algorithm for Carrier Frequency Tracking

This chapter presents and analyzes a DD FB algorithm suitable for tracking frequency errors for short-burst, long-burst and continuous-mode operations. The FB algorithm complements the FF techniques in maintaining the length of the synchronization preamble fixed without greatly affecting performance. An all-digital phase-locked loop (ADPLL) employing oversampling is the algorithm of interest. The FF schemes produce coarse carrier offset estimates to initialize the ADPLL and allow it to work in the vicinity of its stable tracking range from the beginning. This bypasses the loop's lengthy acquisition process and the received data needs only to be tracked. For this reason, acquisition is not examined.

This chapter is subdivided in many sections, each focusing on a particular aspect

of the ADPLL. Section 4.1 presents control theory background necessary in understanding the operation of the ADPLL. Then, the phase detector is analyzed in more detail in section 4.2 while section 4.3 discusses the digital loop filter, which processes the phase error at the output of the phase detector. The core of the chapter commences with the derivation of the ADPLL transfer function in section 4.4. Here the necessary approximations are presented. The ADPLL's performance assessment follows in section 4.5, in which section the loop noise variance is evaluated in terms of the loop bandwidth. Section 4.6 derives the region of stable loop filter gains that result in stable closed-loop transfer functions. The ADPLL's tracking range is another important aspect treated in section 4.7. Finally, the BER degradation of the loop is analyzed in section 4.8 with respect to the loop variance. In the foregoing discussion, the z-transform technique serves as the analysis tool because of the ADPLL's sampled nature.

4.1 Background on ADPLL

The ADPLL extends naturally from the well-established theory on analog phase-locked loops (PLLs) [4]. Figure 4.1 depicts the general analog PLL and ADPLL structures. Their differences lie in the substitution of the analog components by digital ones. For instance, the analog PLL loop filter is replaced by a digital version, and the voltage-controlled oscillator (VCO) by a numerically-controlled oscillator (NCO). The phase detector has been implemented as a digital sub-function for over twenty years, indicating that the ADPLL is the logical extension of the analog PLL.

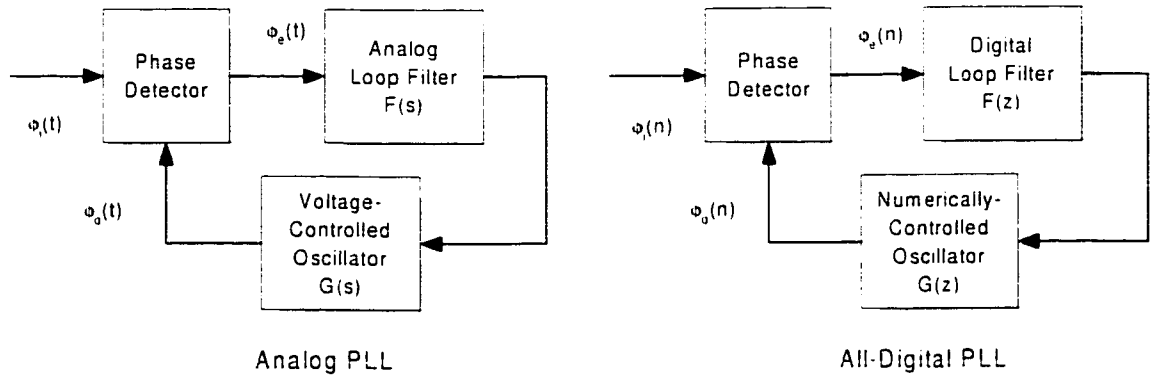

Figure 4.1: Block Diagrams of Analog and All-Digital PLLs.

A brief explanation of the various loop components now follows (refer to figure 4.1). In the analog PLL, the phase detector receives an input phase, $\phi_i(t)$, and VCO output phase, $\phi_o(t)$, and forms a phase error metric, $\phi_e(t)$. The error signal is subsequently processed by the loop filter, with analog transfer function $F(s)$, and outputs a VCO control voltage to adjust the VCO output frequency. The ADPLL functions similarly to its analog counterpart except that a digital filter replaces the analog one and that the filtered $\phi_e(n)$ samples adjust the output phase of an NCO directly. The transfer functions for the VCO and NCO are denoted by $G(s)$ and $G(z)$, respectively. The described process repeats itself since the systems contain feedback.

ADPLLs and analog PLLs are essentially non-linear systems, which makes their analysis very difficult. Fortunately, simplifying assumptions can be applied, allowing the loops to be examined using a linearized model. For instance, when the phase error is small, coinciding with the tracking mode of operation, the ADPLL may be linearized by the equivalent model shown in figure 4.2. In most cases of interest, the phase detector gain, K_d, is selected such that the slope of the combined phase detector and the gain blocks equals unity for zero phase error, i.e., $\phi_i(t) - \phi_o(t) = 0$.

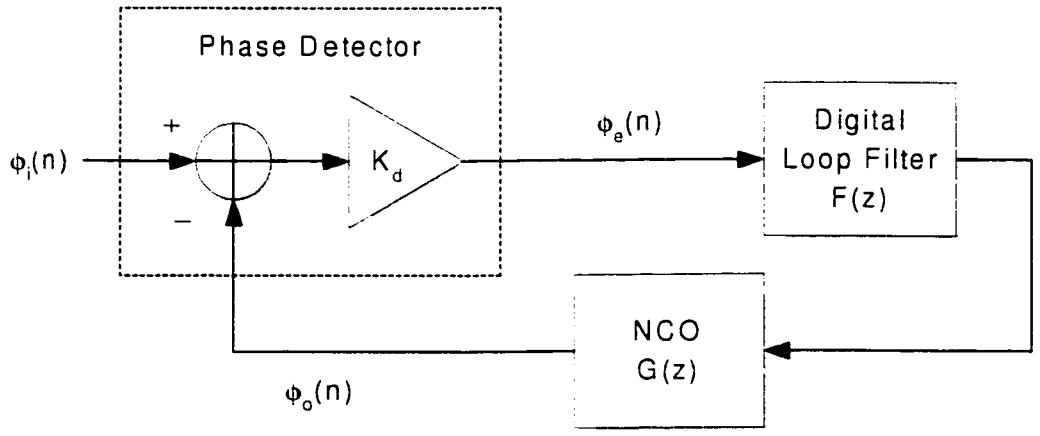

Figure 4.2: Linearized Equivalent Model of the ADPLL.

The analysis presented in this chapter is uniquely constrained to the ADPLL, with occasional references to the analog case. Figure 4.3 details the elaborated ADPLL structure of interest. The initial phase and frequency inputs of the NCO are explicitly included in the diagram, but, in practice, the phase and frequency estimates would initialize the NCO and the loop filter registers, respectively, thus bypassing two additions.

The NCO z-domain transfer function is given by

$$G(z) = \frac{z^{-1}}{1 - z^{-1}} \tag{4.1}$$

$$= \frac{1}{z - 1} \tag{4.2}$$

and the digital loop filter is chosen as a first-order low-pass filter with corresponding transfer function

$$F(z) = \gamma_d + \gamma_f \frac{z^{-1}}{1 - z^{-1}} \tag{4.3}$$

$$= \gamma_d + \gamma_f \frac{1}{z - 1}. \tag{4.4}$$

The coefficients γ_d and γ_f represent the direct path and integrator path gains of the digital loop filter.

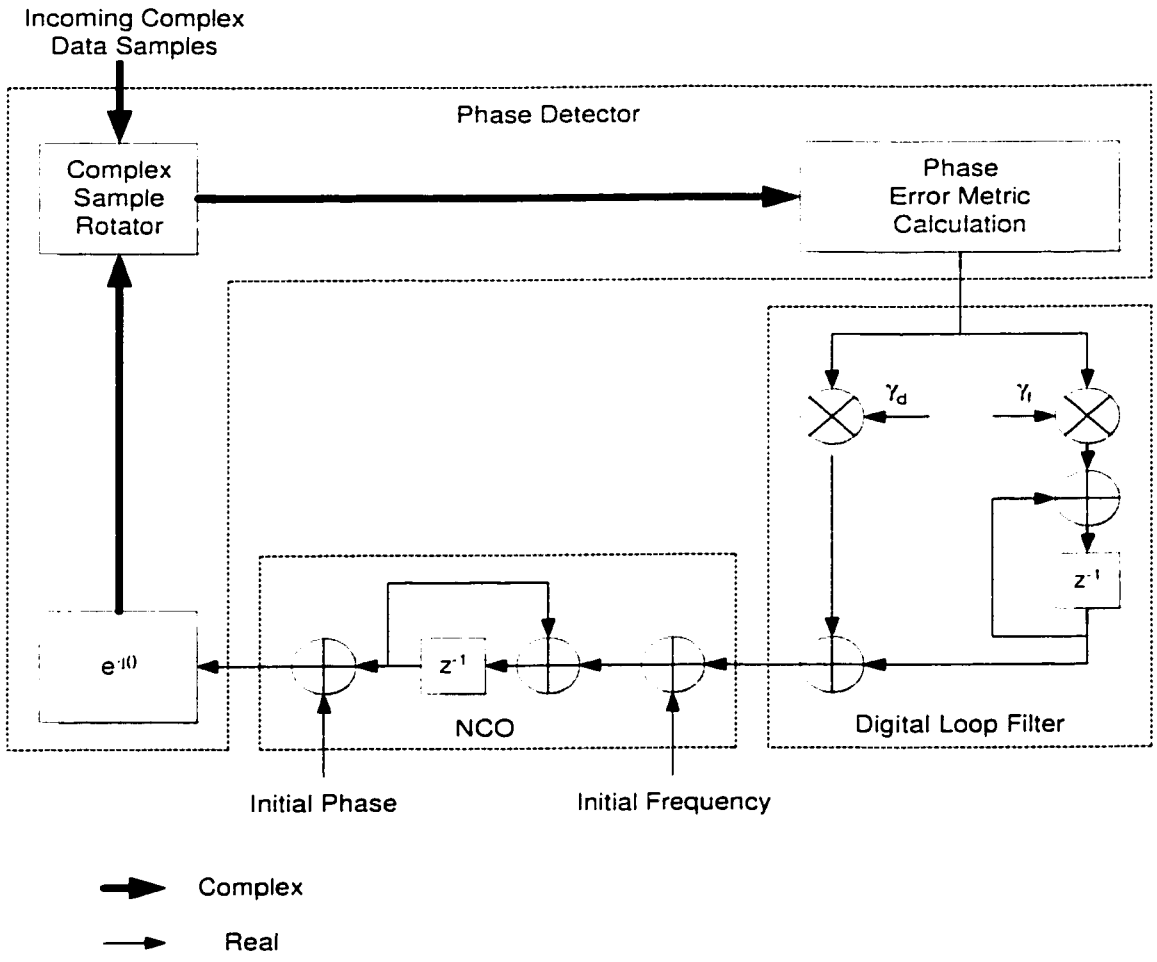

Figure 4.3: Expanded Structure of the ADPLL Used in this Thesis.

First-order filters in a closed loop with a perfect integrator, e.g., an NCO, yield zero steady-state errors when subjected to phase or frequency step inputs. The resulting closed-loop transfer function is second order. The phase detector of figure 4.3 includes an exponential function, a complex sample rotator and the phase error metric calculation. Note that although the phase error metric component performs the necessary error computations, the other two blocks serve to translate or apply

the updated metric to the newly arriving samples at the rotator. These three blocks loosely constitute the complete phase detector.

The matched-filtered samples at the ADPLL input run at the symbol rate and the true frequency offset is expected to remain below one percent of the symbol rate. Hence, adequate oversampling of the frequency offset is already available at this rate. In fact, for proper operation, the ADPLL must be designed to mimic its analog equivalent, and this, by increasing the ADPLL's sampling rate [6]. The benefits of running the ADPLL at the symbol rate are demonstrated in section 4.5 where the noise variance and the loop bandwidth are evaluated.

4.2 Phase Detector Characteristic

One of the major components in a PLL system is the phase detector and is usually the single most important block that varies between implementations. The hard-limited phase detector selected for the ADPLL of this project obeys the relationship

$$\phi_e(n) = K_d[y_n sign(x_n) - x_n sign(y_n)]. \tag{4.5}$$

which describes a combination of adders, subtractors and exclusive-OR gates[1]. The quantities x_n and y_n represent the real and imaginary components of z_n at the input of the phase error detector, and $sign(\cdot)$ denotes the mathematical representation of

[1]Equation (4.5) follows directly from the expression $\phi_e(n) = K_d \Im\{z_n d^*(z_n)\}$, where z_n is the current complex data samples, $d(z_n)$ is the decision made on z_n, K_d is the phase detector gain chosen to satisfy a unity slope for zero phase error, $*$ denotes complex conjugate and $\Im\{\}$ takes the imaginary part of its argument. With $z_n = x_n + jy_n$ and $d(z_n) = a_n + jb_n$, $\phi_e(n) = K_d[y_n a_n - x_n b_n] = K_d[sign(\Re\{z_n\})\Im\{z_n\} - sign(\Im\{z_n\})\Re\{z_n\}] = K_d[y_n sign(x_n) - x_n sign(y_n)]$, where the last substitution results directly from the decision rules in QPSK/4QAM and OQPSK.

a hard-limiter expressed as

$$sign(Y) = \begin{cases} 1. & if \ Y > 0 \\ 0. & if \ Y = 0 \\ -1. & if \ Y < 0 \end{cases} . \tag{4.6}$$

Phase detectors are generally characterized by their S-curve, a plot of the average phase error detector output as a function of the input phase error. A sawtooth response possesses sharp transitions, which aid acquisition. Sinusoidal S-curves are also encountered in practice, but their acquisition durations tend to be larger because they lack the sharp transitions [7, Ch. 8]. A sinusoidal response may be observed with the hard-limited phase detector, when it is operated in a noisy environment. Both types are suitable for tracking once acquisition has successfully completed. Nevertheless, the sawtooth phase detector provides for a simpler implementation. M-PSK phase detectors exhibit $2\pi/M$ periodicity owing to the $2\pi/M$ circular phase symmetry of the constellation. The phase detector characteristic for M-QAM modulation is periodic in $\pi/2$ because of the $\pi/2$ square symmetry of the constellation. Figure 4.4 shows the S-curve for a hard-limited phase detector for QPSK/4QAM and OQPSK ($M = 4$, and the period equals $\pi/2$).

Since the hard-limited phase detector demonstrates approximately linear sawtooth sections, (4.5) may be linearized in each region covering an angle of $2\pi/M$, that is,

$$\phi_e(n) \approx K_d \cdot \frac{\pi}{4} \cdot (\phi_i(n) - \phi_o(n)) \tag{4.7}$$

$$\approx \phi_i(n) - \phi_o(n). \tag{4.8}$$

where $K_d = 4/\pi$ achieves unit slope at the origin of the S-curve. The $\pi/4$ factor in (4.7) is attributed to the approximate slope of the phase error characteristic at the

origin, excluding K_d.

Since the phase detector employed herein is based on decisions of the rotated symbol samples selected at the optimum eye openings, the phase detector is therefore DD, so the overall loop qualifies also as DD.

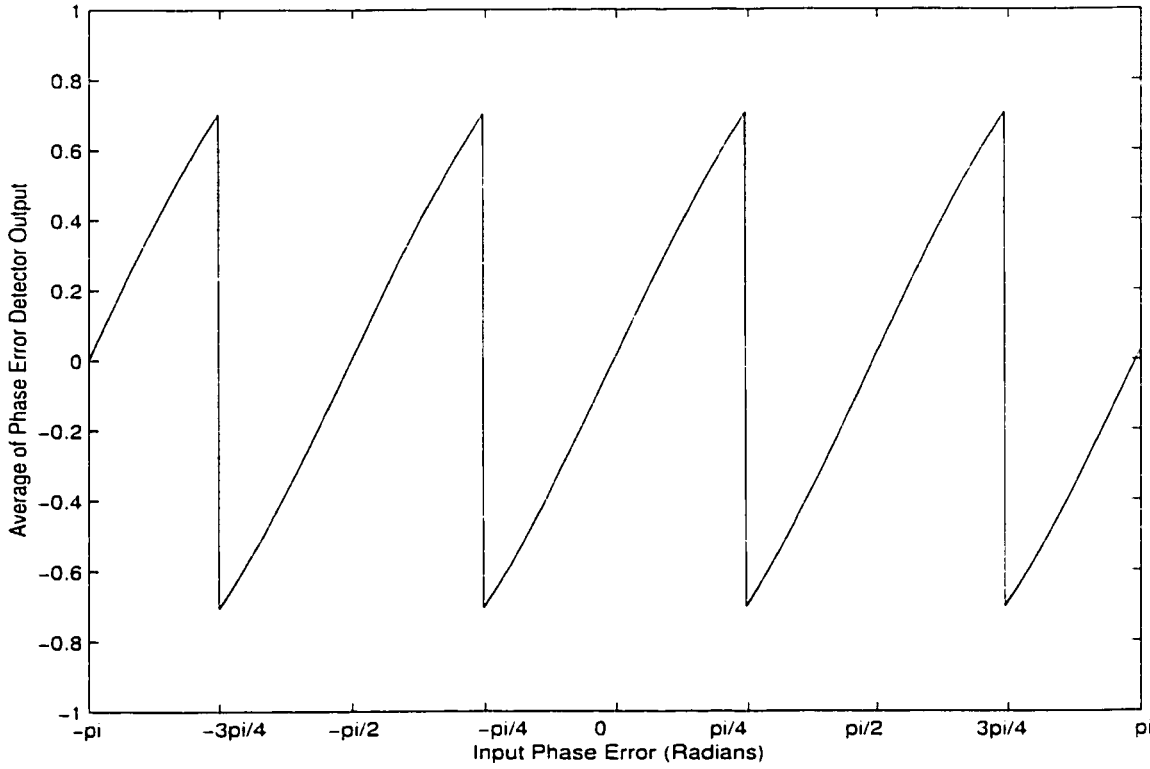

Figure 4.4: Phase Detector S-Curve for QPSK/4QAM and OQPSK - Noiseless Case.

4.3 Digital Loop Filter

The digital loop filter $F(z)$ determines the amount of noise entering the loop by adjusting the loop's bandwidth through its gain coefficients, γ_d and γ_f (discussed in a later section). A small bandwidth passes less noise but restricts the tractable frequency range. It additionally increases the overall acquisition time. In contrast, a large bandwidth allows the loop to quickly acquire and track much greater frequency

offsets at the expense of increased steady-state noise. Since the ADPLL is introduced primarily for tracking purposes, a residual frequency offset equal to a small fraction of the symbol rate is to be tolerated and, consequently, a narrow bandwidth suffices.

Choosing a first-order loop filter allows the ADPLL to track not only a phase error, but also a frequency error, as mentioned earlier[2] [30]. The general first-order loop filter transfer function is

$$F(z) = \gamma_d + \gamma_f \frac{z^{-1}}{1 - z^{-1}} \tag{4.9}$$

with the equivalent structure shown in figure 4.5.

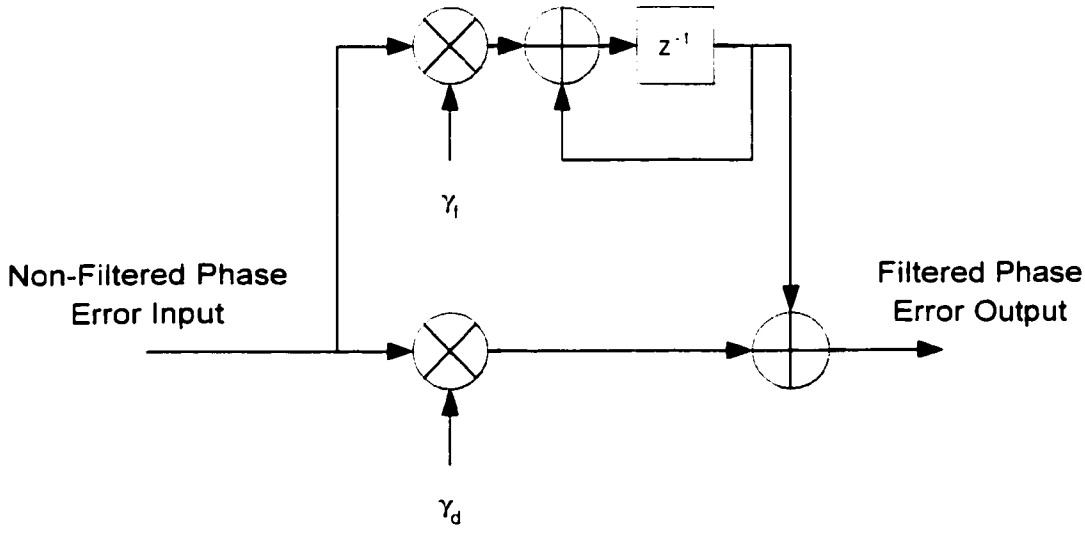

Figure 4.5: Block Diagram of a First-Order Digital Loop Filter.

[2]A loop filter composed solely of a direct gain branch (zero-order loop filter) is unable to track a frequency error. However, a loop filter higher than order-one does provide a significant advantage relative to the additional hardware complexity it imposes, and most implementations behave very satisfactorily with a first-order loop [29, Sec. 6.4].

4.4 Transfer Function

The derivations of the ADPLL's loop bandwidth and loop noise variance presented in the next section require knowledge of the closed-loop transfer function, and, so, is derived here.

From control theory, the closed loop ADPLL transfer function, $H(z)$, of figure 4.2 is expressed, in general, as

$$H(z) = \frac{\Phi_o(z)}{\Phi_i(z)} \tag{4.10}$$

$$= \frac{F(z)G(z)}{1 + F(z)G(z)}. \tag{4.11}$$

Using the expressions for $G(z)$ and $F(z)$ from equations (4.2) and (4.4), and substituting (4.8) for K_d, the numerator of (4.11) equals

$$F(z)G(z) = \frac{\gamma_d(z-1) + \gamma_f}{(z-1)^2}. \tag{4.12}$$

Substituting (4.12) into (4.11) produces the closed-loop transfer function,

$$H(z) = \frac{\gamma_d(z-1) + \gamma_f}{(z-1)^2 + \gamma_d(z-1) + \gamma_f} \tag{4.13}$$

$$= \frac{N(z)}{D(z)}. \tag{4.14}$$

Correspondingly, the phase error to phase input transfer function equals

$$1 - H(z) = \frac{\Phi_e(z)}{\Phi_i(z)} \tag{4.15}$$

$$= \frac{(z-1)^2}{(z-1)^2 + \gamma_d(z-1) + \gamma_f} \tag{4.16}$$

$$= \frac{N_e(z)}{D(z)}. \tag{4.17}$$

Referring to the analysis procedure outlined in [6], $1 - H(z)$ is denoted by

$$1 - H(z) = \frac{(z-1)^2}{(z-\alpha)^2 + \beta^2} \tag{4.18}$$

$$= \frac{N_e(z)}{D(z)} \tag{4.19}$$

where α and β are variables chosen to meet the ADPLL design specifications. Let

$$\alpha = \exp(-\zeta\omega_n T_{sym}) \cos(\omega_n T_{sym}\sqrt{1-\zeta^2}) \tag{4.20}$$

$$\beta = \exp(-\zeta\omega_n T_{sym}) \sin(\omega_n T_{sym}\sqrt{1-\zeta^2}) \tag{4.21}$$

where T_{sym} is the ADPLL sampling period (selected as the symbol rate), ω_n is the natural frequency of the loop ($\omega_n T_{sym}$ is the natural frequency normalized to the sampling period), and ζ is the loop damping factor.

Substituting (4.20) and (4.21) into the denominator polynomial $D(z)$ of (4.18) and (4.19) results in

$$D(z) = (z-\alpha)^2 + \beta^2 \tag{4.22}$$

$$= z^2 - 2\alpha z + \alpha^2 + \beta^2 \tag{4.23}$$

$$= z^2 - 2z\exp(-\zeta\omega_n T_{sym}) \cos(\omega_n T_{sym}\sqrt{1-\zeta^2}) + \exp(-2\zeta\omega_n T_{sym}). \tag{4.24}$$

Rearranging and equating corresponding terms of $D(z)$ in (4.13) with those of (4.24) highlights the relationship between the gain coefficients and the expressions for α and β. Going through the details, $D(z)$ of (4.13) may be rewritten as

$$D(z) = (z-1)^2 + \gamma_d(z-1) + \gamma_f \tag{4.25}$$

$$= z^2 - 2z + 1 + \gamma_g z - \gamma_d + \gamma_f \tag{4.26}$$

$$= z^2 + z(\gamma_d - 2) + (1 - \gamma_d + \gamma_f). \tag{4.27}$$

Direct comparison of (4.27) with (4.24) clearly indicates that

$$\gamma_d = 2\left[1 - \exp(-\zeta\omega_n T_{sym})\cos(\omega_n T_{sym}\sqrt{1-\zeta^2})\right] \tag{4.28}$$

and

$$\gamma_f = \exp(-2\zeta\omega_n T_{sym}) - 1 + \gamma_d \tag{4.29}$$

$$= 1 - 2\exp(-\zeta\omega_n T_{sym})\cos(\omega_n T_{sym}\sqrt{1-\zeta^2}) + \exp(-2\zeta\omega_n T_{sym}). \tag{4.30}$$

The frequency domain transfer function is directly obtained by substituting $z = \exp(j\omega T_{sym})$ into $H(z)$, i.e.,

$$H(\exp(j\omega T_{sym})) = H(z)\Big|_{z=exp(j\omega T_{sym})}. \tag{4.31}$$

If the loop is tracking, the steady-state phase error variance (loop noise variance), $\sigma^2_{\phi_e}$, is assumed small ($\sigma^2_{\phi_e} \ll 1$) and (4.31) may be interpreted as a continuous-time filter $H_c(j\omega)$ [31, Ch. 7], that is,

$$H_c(j\omega) = H(z)\Big|_{z=exp(j\omega T_{sym})}. \tag{4.32}$$

If, in addition, $H(z)$ is designed as a lowpass filter with a loop bandwidth B_L much smaller than the sampling rate ($B_L \ll 1/T_{sym}$, fulfilled when $\omega_n T_{sym} \ll 1$), then the approximation $z = \exp(j\omega T_{sym}) \approx 1 + j\omega T_{sym}$ holds. Therefore, the ADPLL closely mimics the behavior of its analog equivalent. This result indicates that in order for an ADPLL to approximate an analog PLL, its sampling rate must be high compared to its loop bandwidth [6]. Under such requirements, $H(z)$ may be approximated using

$H_c(s)$, the general second-order analog PLL transfer function.

$$H_c(s) = \frac{2\zeta\omega_n T_{sym} + \omega_n^2}{s^2 + 2\zeta\omega_n T_{sym} + \omega_n^2}. \tag{4.33}$$

$H_c(s)$ is the Laplace-domain transfer function of the general analog PLL employing the same damping and natural frequency as the ADPLL. Equations (4.34) through (4.36) establish the relationships between the digital and analog gain parameters:

$$\gamma_d = 2\zeta\omega_n T_{sym} \tag{4.34}$$

$$\gamma_f = (\omega_n T_{sym})^2 \tag{4.35}$$

$$= \frac{\gamma_d^2}{4\zeta^2}. \tag{4.36}$$

Figure 4.6 plots the ADPLL transfer function versus frequency (normalized by ω_n) for a variety of natural frequencies while maintaining th same sampling frequency in each case. Also shown is the analog PLL equivalent transfer function to provide the theoretical reference for the digital curves.

The ADPLL transfer function closely approximates that of an analog PLL, but some discrepancies exist around the sampling frequency, even though the theoretical limit is half the sampling rate, according to Nyquist's sampling theorem (beyond $f_{sym}/2$, there exists some form of aliasing and the loop behaves erratically). Although not very severe, the differences only affect the tracking range of the ADPLL if it is operated near the $f_{sym}/2$ threshold. Section 4.7 discusses this topic in greater detail.

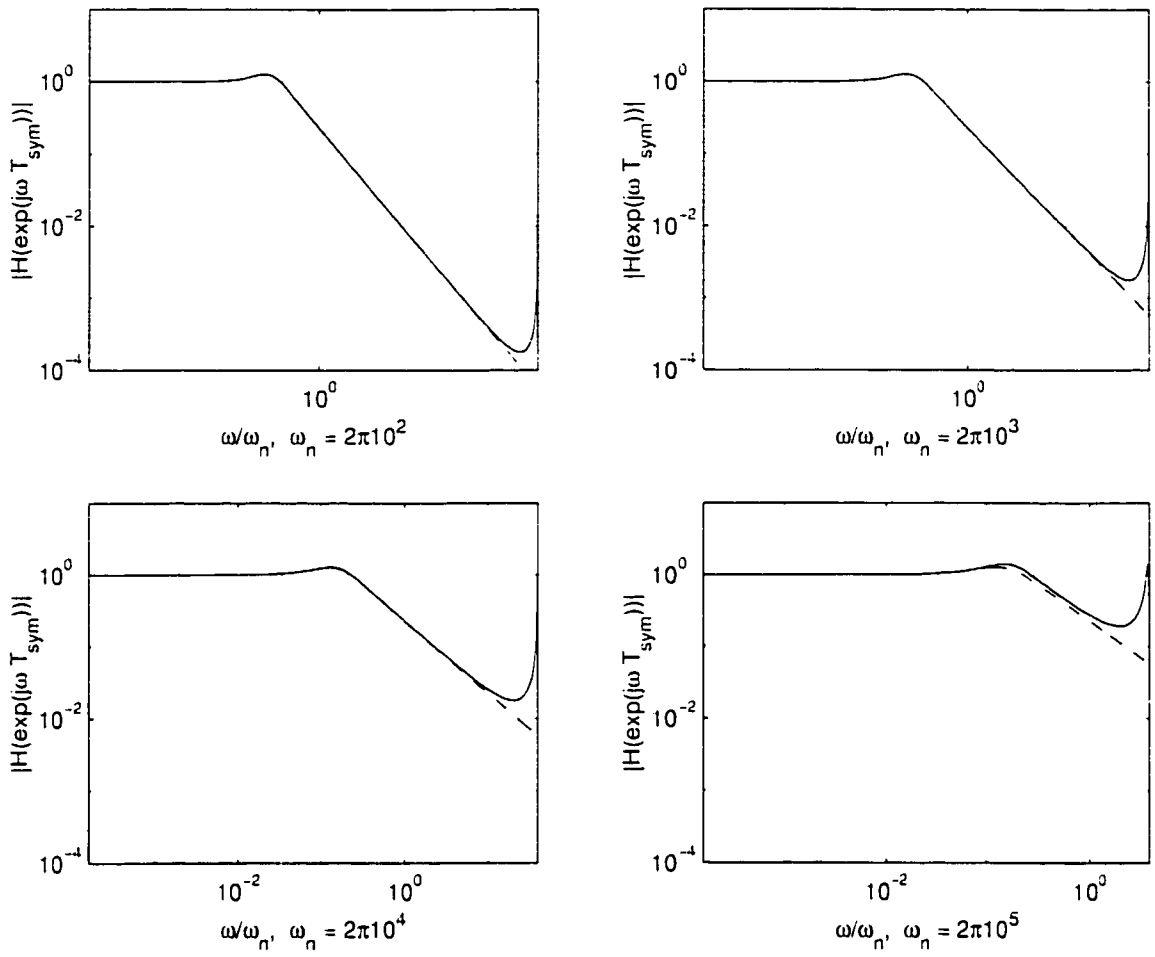

Figure 4.6: ADPLL Transfer Function (Log Scales).

4.5 Loop Noise Variance and Loop Bandwidth

In general, the loop noise variance at the phase detector output is given by the following contour integral,

$$\sigma^2_{\phi_e} = \frac{1}{2\pi j}\oint_{|z|=1} H(z)H(z^{-1})z^{-1}\frac{S_n(z)}{2P_s}\,dz \tag{4.37}$$

or, likewise, by (after transforming the contour integral with $z = exp(j\omega T_{sym})$).

$$\sigma^2_{\phi_e} = \frac{1}{2\pi} T_{sym} \int_{-\pi/T_{sym}}^{\pi/T_{sym}} |H(exp(j\omega T_{sym}))|^2 S_{n_B}(exp(j\omega T_{sym}))\, d\omega \qquad (4.38)$$

where P_s is the average input signal power (equal to E_s/T_{sym}). $S_n(z)$ is the z-transform of the input noise autocorrelation function, whereas $S_{n_B}(exp(j\omega T_{sym}))$ is its Fourier transform normalized by $2E_s$.

The noise entering the loop can be modeled as AWGN since the incoming samples are taken at the symbol rate (perfect symbol-timing is assumed). The independence of the samples follows from the zero-ISI matched filter criterion introduced in chapter 2, where points sampled at the optimum eye openings exhibit no ISI and, consequently, behave as independent random variables. The noise remains Gaussian since the system is linear. The noise samples are uncorrelated with variance $\sigma_n^2 = N_0 W_i$ where N_0 is the one-sided *psd* of the noise and W_i is the bandwidth of the intermediate frequency (IF) filter, limiting the amount of noise entering the loop. Using this information, the loop noise variance can now be expressed as

$$\sigma^2_{\phi_e} = \frac{1}{2\pi j} \oint_{|z|=1} H(z)H(z^{-1})z^{-1} \frac{\sigma_n^2}{2P_s}\, dz \qquad (4.39)$$

$$= \frac{1}{2\pi j} \frac{N_0 W_i}{2P_s} \oint_{|z|=1} H(z)H(z^{-1})z^{-1}\, dz. \qquad (4.40)$$

Defining the ADPLL's one-sided loop bandwidth B_L as

$$\frac{2B_L}{W_i} = \frac{1}{2\pi j} \oint_{|z|=1} H(z)H(z^{-1})z^{-1} dz. \qquad (4.41)$$

$\sigma^2_{\phi_e}$ then degenerates to

$$\sigma^2_{\phi_e} = \frac{N_0}{2P_s}(2B_L) \qquad (4.42)$$

$$= \frac{N_0}{2E_s}(2B_L T_{sym}) \tag{4.43}$$

where the substitution $P_s = E_s/T_{sym}$ was employed.

In an equivalent manner, the $z = exp(j\omega T_{sym})$ version of equations are

$$\sigma^2_{\phi_e} = \frac{1}{2\pi} T_{sym} \int_{-\pi/T_{sym}}^{\pi/T_{sym}} |H(exp(j\omega T_{sym}))|^2 \frac{N_0}{2E_s}\, d\omega \tag{4.44}$$

where

$$S_{n_B}(exp(j\omega T_{sym})) = \frac{N_0}{2E_s} \tag{4.45}$$

was used. The one-sided loop bandwidth B_L is defined as

$$2B_L T_{sym} = \frac{T_{sym}}{2\pi} \int_{-\pi/T_{sym}}^{\pi/T_{sym}} |H(exp(j\omega T_{sym}))|^2\, d\omega \tag{4.46}$$

and yields

$$\sigma^2_{\phi_e} = \frac{N_0}{2E_s}(2B_L T_{sym}) \tag{4.47}$$

which agrees with (4.43) derived earlier using the z-transform technique.

The previous results may also be derived using the equivalent analog transfer function and analog loop bandwidth, as long as $\omega T_{sym} \ll 1$ is satisfied. In such a case, B_L approximately equals the analog loop bandwidth.

$$B_L \approx B_L(analog) \tag{4.48}$$

$$= \frac{1}{2\pi} \int_0^\infty |H_c(j\omega)|^2\, d\omega. \tag{4.49}$$

Figure 4.7 plots the steady-state phase error variance versus the loop bandwidth

normalized to the symbol period. Undoubtedly, a larger loop bandwidth increases the phase error variance. When the ADPLL is known to operate with small frequency and phase offsets (tracking mode), then a lesser B_L suffices, for it sustains a minimal steady-state error variance without losing signal lock.

Figure 4.8 illustrates the steady-state phase error variance versus E_b/N_0 for different values of B_L. Increasing the signal-to-noise ratio reduces the loop noise variance for all cases of B_L considered. In addition, the loop noise variance $\sigma^2_{\phi_e}$ of (4.47) corresponds to the CRLB for carrier trackers [9, Sec. 6.3]. Hence, the algorithm attains the lower theoretical bound under the conditions presented in this chapter. Since the transfer function of section 4.4 was shown to follow the ideal case under the same assumptions exercised in this section, the simulations must agree with the derived variance expression in (4.43) (or (4.47)).

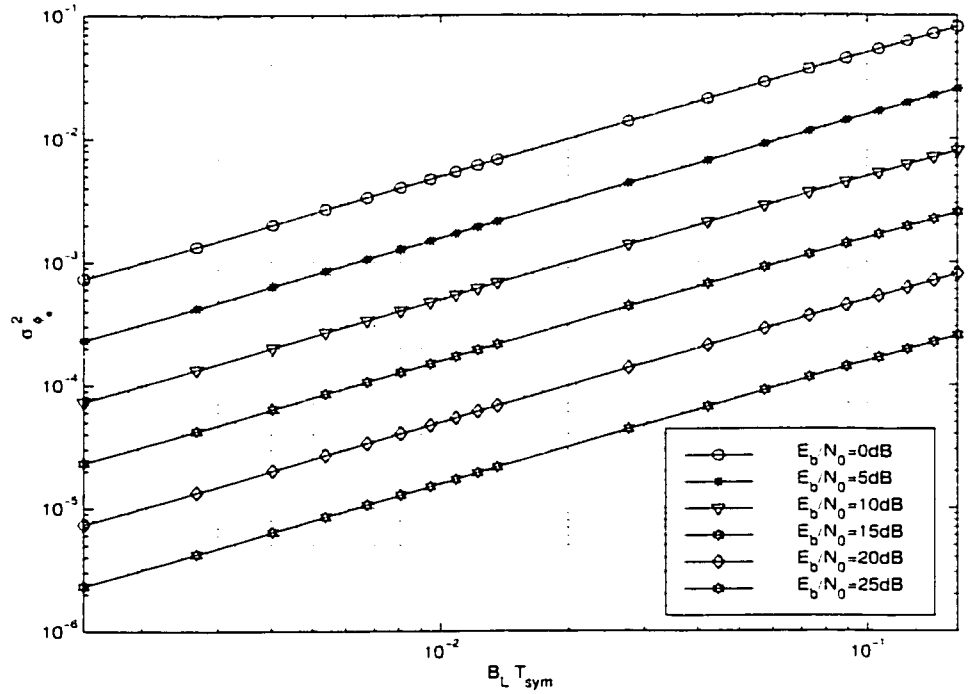

Figure 4.7: Loop Noise Variance Versus Loop Bandwidth (QPSK/4QAM and OQPSK).

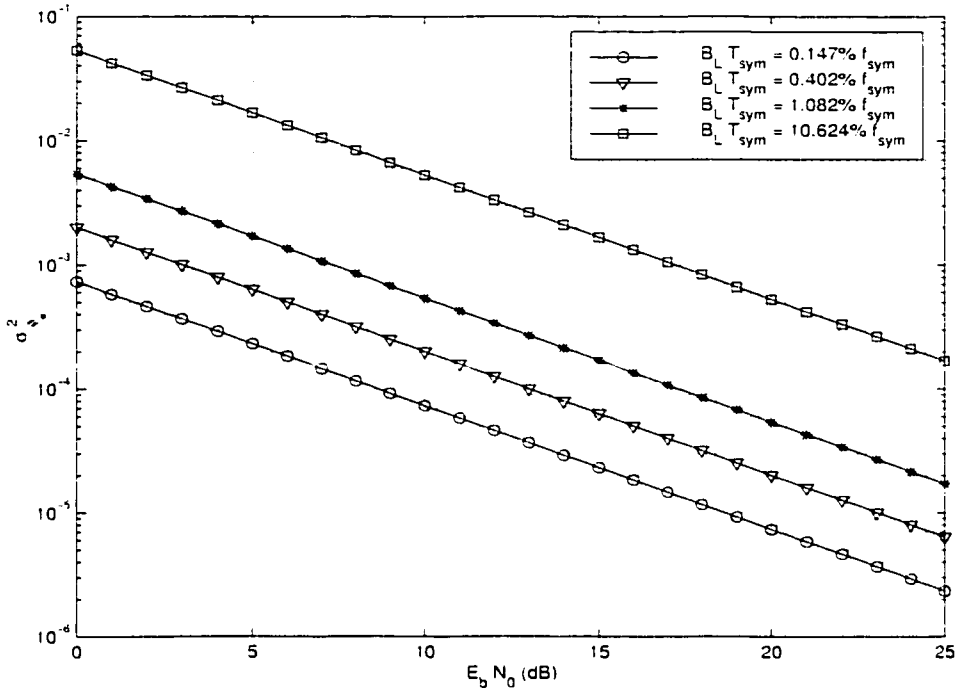

Figure 4.8: Loop Noise Variance Versus E_b/N_0 (QPSK/4QAM and OQPSK).

4.6 Closed-Loop Stability

The ADPLL's stability is assessed in this section using the z-transform analysis technique. For correct loop behavior, the loop filter gains must be chosen such that the poles of the closed-loop transfer function of (4.13) lie inside the unit circle in the z-plane. The magnitude of the poles should measure less than unity, that is,

$$|roots[D(z)]| \quad < \quad 1 \tag{4.50}$$

where $D(z)$ is taken from (4.27). The roots of D(z) equal

$$z \quad = \quad 1 + \frac{-\gamma_d \pm \sqrt{\gamma_d^2 - 4\gamma_f}}{2}. \tag{4.51}$$

Equating their magnitude to be less than unity, we obtain

$$\left| 1 + \frac{-\gamma_d \pm \sqrt{\gamma_d^2 - 4\gamma_f}}{2} \right| < 1. \tag{4.52}$$

The solutions (4.53), (4.54) and (4.55) to the above inequality define the stable region for the loop filter gains:

$$\gamma_f > 0 \tag{4.53}$$

$$\gamma_f > 2\gamma_d - 4 \tag{4.54}$$

$$\gamma_f < \gamma_d . \tag{4.55}$$

Figure 4.9 plots the triangular region of stability bounded by the above three equations. The design curve for $\zeta = 1/\sqrt{2}$ is also shown to verify that proper values may be chosen that satisfy both the stable region condition and the widely accepted damping value of $1/\sqrt{2}$ for a second-order loop.

Minimum noise bandwidth, and, consequently, minimum phase error variance, is achieved for $\zeta = 1/2$. In practice, $\zeta = 1/\sqrt{2}$ is chosen because it provides more choices for the loop gains without severely intensifying the noise variance. In fact, the noise bandwidth increases by 25% at most if $0.25 < \zeta < 1.0$ holds [4, pp. 31-32].

The cross-over point at $\gamma_d = \gamma_f = 2$ determines the maximum allowed gains for which the loop remains stable, given $\zeta = 1/\sqrt{2}$. Therefore, the gain coefficients must satisfy

$$\gamma_d < 2 \tag{4.56}$$

and

$$\gamma_f < 2 \tag{4.57}$$

in addition to $\zeta = 1/\sqrt{2}$.

If the ADPLL is to behave like its analog counterpart, then γ_d and γ_f must be selected small enough to fulfill $\omega T_{sym} \ll 1$. This is indeed possible for $\zeta = 1/\sqrt{2}$.

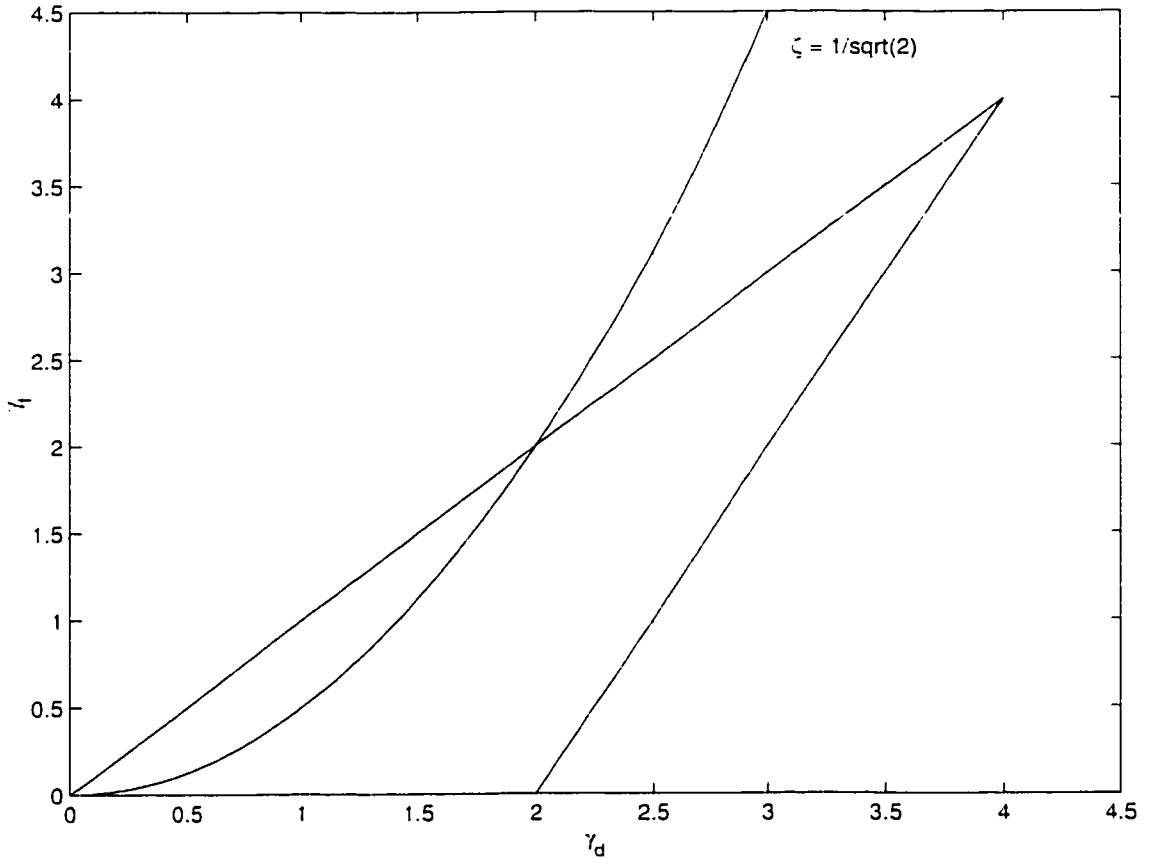

Figure 4.9: Stability Regions for ADPLL Loop Filter Gains.

4.7 Tracking Range

From control theory, the open loop dc gain K_v (obtained by opening the loop and evaluating it at $\omega = 0$) determines the tractable range of frequencies. Applying the limit theorem in the z-transform domain for $z \to 1$, produces

$$K_v = \lim_{z \to 1} [F(z)G(z)] \tag{4.58}$$

$$= \lim_{z \to 1} \left[\frac{\gamma_d (z-1) + \gamma_f}{(z-1)^2} \right] . \tag{4.59}$$

leading to

$$K_v \to \infty . \tag{4.60}$$

Gardner [4, Sec. 2.3] explains that a large open loop dc gain is required if a wide tracking range is desired. Undoubtedly, the ADPLL meets this requirement in (4.60). Hence, the ADPLL exhibits a broad tracking span, limited only by half the sampling rate. However, plots of the ADPLL transfer function exemplify that the theoretical $f_{sym}/2$ limit is not attained, so a discrepancy will exist between the expected and actual results in this case. In our applications, a small frequency offset (less than 1% of f_{sym}) corrupts the received data. The ADPLL's tracking ability is not hindered under these conditions, provided appropriate values for B_L, γ_d and γ_f are enforced.

4.8 Bit-Error-Rate Degradation

BER degradation describes the additional signal-to-noise ratio increase on the system in order to maintain the same BER at the receiver without synchronization errors. The BER degradation translates into a signal-to-noise ratio (E_b/N_0) penalty. To better quantify the E_b/N_0 penalty associated with the ADPLL's variance, some conditions are presented next.

The loop is designed to imitate the behavior of its analog equivalent and operates with perfect symbol-timing epoch. The offsets fall within the loop's bandwidth so the system functions without cycle slips. Contributions to the BER from quantization effects are deferred to a future study. Under these conditions and knowledge of the linearized tracking variance derived in section 4.5, the BER degradation is evaluated. The equations presented for the feedforward estimator in chapter 2 also apply to the

feedback tracker, provided that the linearized ADPLL model is used with its tracking variance, replacing the variance for the feedforward case [9, Sec. 7.4].

Figure 4.10 shows three cases of operating BER (10^{-2}, 10^{-4} and 10^{-6}) for QPSK/4QAM and OQPSK. As the normalized inverse of the phase error variance due to synchronization errors increases, the phase error variance itself decreases causing a corresponding decrease in the BER degradation. Another useful observation is the increase of the BER degradation as the operating BER is decreased (or when the operating noise variance σ_0^2 decreases). This loss is attributed to the increase in synchronization errors at the input of the decision device, which intensify the error variance $\sigma_{\phi_e}^2$ [9, Ch. 7.6]. Refering to (2.111), at higher BERs, the operating noise variance σ_0^2 is very low, so that the increase of $\sigma_{\phi_e}^2$ due to the synchronization errors dominates at these BERs. If synchronization errors occur less frequently, then the E_b/N_0 penalty is also reduced, as illustrated in figure 4.10.

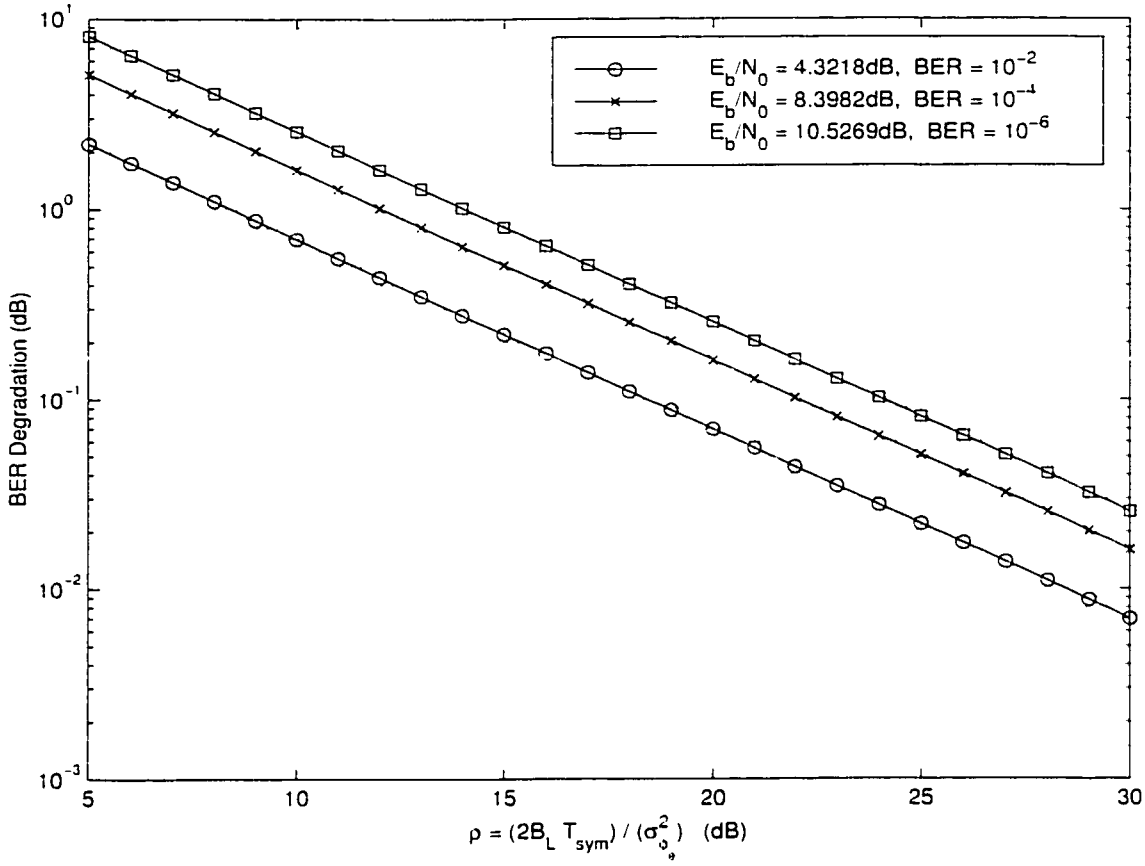

Figure 4.10: BER Degradation (E_b/N_0 penalty) for ADPLL Tracking Loop (QPSK/4QAM and OQPSK).

Chapter 5

Conclusion

This dissertation studied fast, low complexity, all-digital feedforward and feedback carrier recovery techniques applicable to linear modulation schemes (M-PSK, M-QAM and their offset counterparts) in an AGWN, non-multipath PMP burst-mode system. The data-aided feedforward techniques employed oversampling to provide accurate or coarse estimates using a short preamble, whereas the decision-directed FB technique was introduced to track a residual frequency offset following coarse feedforward correction without introducing additional overhead. This chapter highlights the study's salient findings and recommends new avenues for future research which time did not permit to include in this work.

5.1 Summary of Research

The introduction and the first section of chapter 2 discussed the assumptions, the requirements, the signal model and the estimator performance measures for this research.

Chapter 2 then presented the open-loop DA carrier phase offset estimation technique suitable for TDM/TDMA-like burst-mode systems. The scheme was founded

on oversampling a preamble of known data symbols, where multiple samples per symbol were utilized in determining the offset. Its mean and variance were investigated by an approximate analysis for high signal-to-noise ratios. The phase estimate, $\widehat{\theta'_{off}}$, was unbiased for virtually the entire range $[-\pi, \pi]$, indicating that, on the average, it determines the desired parameter. The estimator's variance achieved the CRLB when viewed in terms of the number of equivalent symbols, N/K, rather than the number of samples N. Hence, $\widehat{\theta'_{off}}$ was found to be efficient under this condition, another desired result. Simulations of the *pdf*, the mean and the variance of $\widehat{\theta'_{off}}$ supported the approximate theoretical results, even at low signal-to-noise ratios. BER simulations for QPSK/4QAM and OQPSK compared favorably to the theoretical penalty, with as little as $0.2dB$ to $0.3dB$ loss for a 16-symbol overhead, and $0.4dB$ to $0.6dB$ for a 4-symbol preamble. Oversampling did not severely influence the performance of $\widehat{\theta'_{off}}$. The $\widehat{\theta'_{off}}$ employing a 4-symbol carrier phase recovery overhead and 16 times oversampling was tested in a practical modem for burst-mode QPSK/4QAM and OQPSK using an FPGA test bed. The implementation of $\widehat{\theta'_{off}}$ provided a low complexity, and, thus, low cost, structure with marginal performance degradation, only $0.1dB$ worse than the predicted loss. Accordingly, the phase estimator occupied a small area (228 CLBs in a Xilinx XC4028EX-3 FPGA)while achieving a 40MHz operating frequency. Based on these results, the initial goals for phase recovery have been attained.

Chapter 3 delved into the analysis and simulation of a data-aided autocorrelation-based feedforward frequency offset estimator, of $\widehat{\omega_{off}}$, equally founded on oversampling. The algorithm was generally unbiased for estimation window sizes in excess of 4 QPSK/4QAM or OQPSK symbols. Unfortunately, for increasing window lengths, its variance diverged significantly form the AWGN CRLB of an efficient single-sample-per-symbol frequency estimator. It was recommended to maintain the window length

in the order of 16 symbols. To improve the variance of $\widehat{\omega_{off}}$, the correlation separation L between samples was varied. Increasing L did in effect diminish the variance in an almost linear manner, at the expense of restriction the estimation range in an inversely proportional manner to L. $\widehat{\omega_{off}}$ was implemented practically for a QPSK/4QAM and OQPSK burst-modem using the same FPGA test bed as before. The frequency estimator was designed to provide coarse estimates using a 4-symbol estimation window and a unit symbol correlation separation for the cross-multiplication block. Although more hardware demanding than the phase estimator because of the correlator, the implemented version of $\widehat{\omega_{off}}$ still occupied a small area (484 CLBs in a Xilinx XC4028EX-3 FPGA) and could operate up to 33 MHz. Once again, the initial objectives have been met, this time for frequency estimation.

The fourth chapter developed a DD FB algorithm (ADPLL) for tracking or refining a residual frequency error after coarse feedforward correction. The FB system was studied using the z-transform technique. Since the APDLL was oversampled, it mimicked the behavior of an equivalent analog PLL. For this reason, the ADPLL transfer function closely matched the analog case, up to half the sampling frequency. Because of this equivalence between the analog and digital loops, the ADPLL presented a predictable loop noise variance and BER performance, as good as the one for analog PLLs. The ADPLL demonstrated a wide tracking range limited only by half of the sampling rate. Briefly, the ADPLL performed equally well as its analog equivalent. By its digital nature, the ADPLL is also easily integrable into today's rapidly evolving digital technologies. In addition to all these advantages, the ADPLL operates independently of the proposed FF techniques, so it may be coupled with other FF estimators.

5.2 Topics for Future Research

To conclude this dissertation, below follow some recommendations for future research endeavors.

1. *Study the interaction between carrier recovery and symbol-timing recovery algorithms, specifically, the effects of non-ideal timing epoch.* In general, when studying a recovery technique (e.g. carrier recovery), the other is assumed ideal (e.g. perfect symbol-timing). However, practical systems can never guarantee such conditions, so the interaction between the two, and particularly the effects of non-ideal symbol-timing, should be studied for linear modulation schemes.

2. *Study the effects of quantization on BER and variance performance.* Since carrier recovery algorithms are essentially studied for application in practical systems, quantization is required when targeting a hardware architecture. Therefore, the effects of quantization on the FF and FB estimators' variance and BER performance should be determined (via simulation).

3. *Study the effects of Doppler shifts and multipath fading on the proposed algorithms in conjunction with an equalizer.* It would be beneficial to analyze the effects of these problems since they are commonly encountered in digital mobile systems (Doppler and multipath fading) and wireless local loops, such as BWA (multipath fading). Performance evaluation of the CR techniques with prior or simultaneous equalization of the received data would assess the applicability of this thesis' techniques for channels other than AWGN.

Bibliography

[1] A. Dutta-Roy. "Fixed Wireless Routes for Internet Access." *IEEE Spectrum*, vol. 36, pp. 61–69, September 1999.

[2] R. Morawski, N. Caouras, and T. Le-Ngoc. "Data-Aided Fast Symbol Timing Recovery for TDMA/TDM Point-to-Multipoint Radio Communication Systems (QPSK/OQPSK)." *IEEE CCECE 1999*, May 9-12 1999.

[3] S. Haykin. *Digital Communications*. John Wiley and Sons, New York, 1988.

[4] F. M. Gardner. *Phaselock Techniques*. John Wiley and Sons, New York, 1979.

[5] Y. R. Shayan and T. Le-Ngoc. "All Digital Phase-Locked Loop: Concepts, Design and Applications." *IEEE Proceedings*, vol. 136, Pt. F, pp. 53–56, February 1989.

[6] W. C. Lindsey and C. M. Chie. "A Survey of Digital Phase-Locked Loops." *Proceedings of the IEEE*, vol. 69, pp. 410–431, April 1981.

[7] F. M. Gardner. *Demodulator Reference Recovery Techniques Suited for Digital Implementation*. Final Report: Part I to ESTEC Contract No. 6847/86/NL/DG, 1988.

[8] F. M. Gardner. *Frequency Detectors for Digital Demodulators via Maximum-Likelihood Derivation*. Final Report: Part II to ESTEC Contract No. 8022/88/NL/DG, 1990.

[9] H. Meyr, M. Moeneclaey, and S. A. Fechtel. *Digital Communication Receivers: Synchronization, Channel Estimation, and Signal Processing.* John Wiley and Sons, New York, 1998.

[10] L. E. Franks, "Carrier and Bit Synchronization in Data Communication - A Tutorial Review," *IEEE Transactions on Communications*, vol. COM-28, pp. 1107–1120, August 1980.

[11] M. Srinath, P. Rajasekaran, and R. Viswanathan, *Introduction to Statistical Signal Processing with Applications.* Prentice Hall, New Jersey, 1996.

[12] H. L. V. Trees, *Detection, Estimation, and Linear Modulation Theory, Part I.* John Wiley and Sons, New York, 1968.

[13] J. G. Proakis, *Digital Communications.* McGraw Hill, Inc., New York, 1995.

[14] S. Gardner, "Burst Modem Design Techniques, Part 1," *Communication System Design*, vol. 5, pp. 30–37, July 1999.

[15] S. Gardner, "Burst Modem Design Techniques, Part 2," *Communication System Design*, vol. 5, pp. 37–44, August 1999.

[16] A. J. Viterbi and A. M. Viterbi, "Nonlinear Estimation of PSK-Modulated Carrier Phase with Applications to Burst Digital Transmission," *IEEE Transactions on Information Theory*, vol. IT-29, pp. 543–551, July 1983.

[17] R. D. Gitlin, J. F. Hayes, and S. B. Weinstein, *Data Communications Principles.* Plenum Press, New York, 1992.

[18] M. Morelli and U. Mengali, "Feedforward Frequency Estimation for PSK: a Tutorial Review," *European Transactions on Telecommunications*, vol. 9, pp. 103–116, Mar.-Apr. 1998.

[19] D. C. Rife and R. R. Boorstyn, "Single-Tone Parameter Estimation from Discrete-Time Observations," *IEEE Transactions on Information Theory*, vol. IT-20, pp. 591–598, September 1974.

[20] S. A. Tretter, "Estimating the Frequency of a Noisy Sinusoid by Linear Regression," *IEEE Transactions on Information Theory*, vol. IT-31, pp. 832–835, November 1985.

[21] A. Papoulis, *Probability, Random Variables, and Stochastic Processes*, McGraw-Hill, Inc., New York, 1991.

[22] R. D. Girolamo, "Fast and Efficient Carrier Synchronization for Burst-Mode Communications," Master's thesis, Concordia University, October 1993.

[23] H. Samueli and B. C. Wong, "A VLSI Architecture for a High-Speed All-Digital Quadrature Modulator and Demodulator for Digital Radio Applications," *IEEE Journal on Selected Areas in Communications*, vol. 8, pp. 1512–1519, October 1990.

[24] R. E. Walpole and R. H. Myers, *Probability and Statistics for Engineers and Scientists*, MacMillan Publishing Company, New York, 1972.

[25] J.-M. Muller, *Elementary Functions: Algorithms and Implementation*, Birkhauer, Boston, 1997.

[26] J. E. Volder, "The Cordic Trigonometric Technique," *IRE Transactions on Electronic Computers*, vol. EC-8, pp. 330–334, September 1959.

[27] M. Oerder and H. Meyr, "Digital Filter and Square Timing Recovery," *IEEE Transactions on Communications*, vol. 36, pp. 605–611, May 1988.

[28] C. Bergogne, P. Sehier, and M. Bousquet, "Reduced Complexity Frequency Estimator Applied to Burst Transmission," in *1995 Fourth IEEE International Conference on Universal Personal Communications*, pp. 231–235, Nov. 6-10 1995.

[29] J. A. C. Bingham, *The Theory and Practice of Modem Design*, John Wiley and Sons, NY, 1988.

[30] N. S. Nise, *Control Systems Engineering*, Redwood City, Calif. : Benjamin Cummings Pub. Co., 1995.

[31] A. V. Oppenheim and R. W. Schafer, *Discrete-Time Signal Processing*, Prentice Hall, New Jersey, 1995.

[32] F. Classen, H. Meyr, and P. Sehier, "An All Feedforward Synchronization Unit for Digital Radio," in *VTC93*, pp. 738–741, 1993.

Appendix A

Derivation Details of the Frequency Offset Estimator's Second Moment

To simplify the expression of the frequency variance, we commence with the expression of (3.50).

$$E\left[(\widehat{\omega_{off}}T_{sa})^2\right] = \frac{1}{(L.N)^2}\sum_{n=\ell+L}^{\ell+L+N-1}\sum_{p=\ell+L}^{\ell+L+N-1}E\left[y_n y_p\right] \tag{A.1}$$

where $y_n = \Im\left\{z_n z_{n-L}^*\right\}$. The expanded form of $z_n z_{n-L}^*$ with $\theta'_{off} = 0$ is given by

$$\begin{aligned} z_n z_{n-L}^* = \quad & \cos(\omega_{off}T_{sa}L) \\ & +j\sin(\omega_{off}T_{sa}L) \\ & +\gamma_{In-L}\cos\left(\omega_{off}T_{sa}\left(n-\ell-\frac{N-1}{2}\right)\right) \\ & +j\gamma_{In-L}\sin\left(\omega_{off}T_{sa}\left(n-\ell-\frac{N-1}{2}\right)\right) \\ & -j\gamma_{Qn-L}\cos\left(\omega_{off}T_{sa}\left(n-\ell-\frac{N-1}{2}\right)\right) \end{aligned}$$

$$
\begin{aligned}
&+\hat{\gamma}_{Qn-L}\sin\left(\omega_{off}T_{sa}\left(n-\ell-\frac{N-1}{2}\right)\right)\\
&+\hat{\gamma}_{In}\cos\left(\omega_{off}T_{sa}\left(n-L-\ell-\frac{N-1}{2}\right)\right)\\
&-j\hat{\gamma}_{In}\sin\left(\omega_{off}T_{sa}\left(n-L-\ell-\frac{N-1}{2}\right)\right)\\
&+j\hat{\gamma}_{Qn}\cos\left(\omega_{off}T_{sa}\left(n-L-\ell-\frac{N-1}{2}\right)\right)\\
&+\hat{\gamma}_{Qn}\sin\left(\omega_{off}T_{sa}\left(n-L-\ell-\frac{N-1}{2}\right)\right)\\
&+\hat{\gamma}_{In}\hat{\gamma}_{In-L}\\
&-j\hat{\gamma}_{In}\hat{\gamma}_{Qn-L}\\
&+j\hat{\gamma}_{Qn}\hat{\gamma}_{In-L}\\
&+\hat{\gamma}_{Qn}\hat{\gamma}_{Qn-L}
\end{aligned}
\tag{A.2}
$$

where $H_N(\cdot) = B = 1$ was used because of the approximately constant amplitude assumption of the DA preamble sequence used for estimation.

The expression for y_n immediately follows by taking the imaginary part of (A.2). It is expressed by

$$
\begin{aligned}
y_n \;=\;& \sin(\omega_{off}T_{sa}L)\\
&+\hat{\gamma}_{In-L}\sin\left(\omega_{off}T_{sa}\left(n-\ell-\frac{N-1}{2}\right)\right)\\
&-\hat{\gamma}_{Qn-L}\cos\left(\omega_{off}T_{sa}\left(n-\ell-\frac{N-1}{2}\right)\right)\\
&-\hat{\gamma}_{In}\sin\left(\omega_{off}T_{sa}\left(n-L-\ell-\frac{N-1}{2}\right)\right)\\
&+\hat{\gamma}_{Qn}\cos\left(\omega_{off}T_{sa}\left(n-L-\ell-\frac{N-1}{2}\right)\right)\\
&+\hat{\gamma}_{Qn}\hat{\gamma}_{In-L}\\
&-\hat{\gamma}_{In}\hat{\gamma}_{Qn-L}
\end{aligned}
\tag{A.3}
$$

To alleviate some of the notational burden, let

$$\Omega = \omega_{off} T_{sa} \tag{A.4}$$

The expectation operation in (A.1) may be arranged so that the elements appear in a column format. This will help keep the multiplication clear.

$$E[y_n y_p] = E\left[\begin{pmatrix} \sin(\Omega L) \\ +\gamma_{In-L}\sin\left(\Omega\left(n-\ell-\frac{N-1}{2}\right)\right) \\ -\gamma_{Qn-L}\cos\left(\Omega\left(n-\ell-\frac{N-1}{2}\right)\right) \\ -\gamma_{In}\sin\left(\Omega\left(n-L-\ell-\frac{N-1}{2}\right)\right) \\ +\gamma_{Qn}\cos\left(\Omega\left(n-L-\ell-\frac{N-1}{2}\right)\right) \\ +\gamma_{Qn}\gamma_{In-L} \\ -\gamma_{In}\gamma_{Qn-L} \end{pmatrix} \cdot \begin{pmatrix} \sin(\Omega L) \\ +\gamma_{Ip-L}\sin\left(\Omega\left(p-\ell-\frac{N-1}{2}\right)\right) \\ -\gamma_{Qp-L}\cos\left(\Omega\left(p-\ell-\frac{N-1}{2}\right)\right) \\ -\gamma_{Ip}\sin\left(\Omega\left(p-L-\ell-\frac{N-1}{2}\right)\right) \\ +\gamma_{Qp}\cos\left(\Omega\left(p-L-\ell-\frac{N-1}{2}\right)\right) \\ +\gamma_{Qp}\gamma_{Ip-L} \\ -\gamma_{Ip}\gamma_{Qp-L} \end{pmatrix}\right] \tag{A.5}$$

Multiplying through term by term and taking the expectation, and recalling that the noise terms are zero-mean, produces

$$E[y_n y_p] =$$

$$\sin^2(\Omega L) + R(n-p)\cos(\Omega(n-p))$$

$$
\begin{aligned}
&-R(n-p-L)\cos(\Omega(n-p)) - R(n-p)\cos(\Omega(n-p+L)) \\
&+R(n-p)\cos(\Omega(n-p)) + 2R^2(n-p) \\
&-2R(n-p-L)R(n-p+L)
\end{aligned} \tag{A.6}
$$

where $R(m)$ is the autocorrelation of the noise components for each channel.

If $R(\cdot)$ represents elements from a diagonal covariance matrix with entries σ_v^2, then the resulting second moment of (A.1) is readily obtained as

$$
\begin{aligned}
E\left[(\widehat{\omega_{off}}T_{sa})^2\right] &= \frac{1}{(LN)^2}\left[N^2\sin^2(\Omega L) + N\sigma_v^2\right. \\
&\quad -(N-L)\sigma_v^2\cos(2\Omega L) - (N-L)\sigma_v^2\cos(-2\Omega L) \\
&\quad \left.+N\sigma_v^2 + 2N\sigma_v^4\right]
\end{aligned} \tag{A.7}
$$

Substituting $\cos(2\Omega L) = 1 - 2\sin^2(\Omega L)$ into (A.7) and rearranging terms gives us

$$
E\left[(\widehat{\omega_{off}}T_{sa})^2\right] = \frac{1}{L^2}\left[\left(1+\frac{4\sigma_v^2}{N}\right)\sin^2(\Omega L) + \frac{2L\sigma_v^2}{N^2}\cos(2\Omega L) + \frac{2\sigma_v^4}{N}\right]. \tag{A.8}
$$

If in addition $T_{sa} = T_{sym}$, i.e., $K = 1$, then (A.8) degenerates to the results presented in [28]. Setting $\omega_{off} = 0$ simplifies (A.8) further and achieves the result derived in [32].

In the case where $\omega_{off} = 0$ and $R(\cdot)$ represents elements from a Toeplitz even-symmetric matrix (which occurs in all practical applications employing symmetric pulse-shaping), (A.6) may be rewritten as

$$
\begin{aligned}
E\left[y_n y_p\right] &= 2R(n-p) - R(n-p-L) - R(n-p+L) + 2R^2(n-p) \\
&\quad -2R(n-p-L)R(n-p+L)
\end{aligned} \tag{A.9}
$$

so that after some straightforward manipulations, the second moment given by (A.1)

leads to the following cumbersome form:

$$
\begin{aligned}
E\left[(\widehat{\omega_{off}}T_{sa})^2\right] \;=\; & \frac{1}{(LN)^2}\left\{2\left(NR(0)+2\sum_{m=1}^{N-1}(N-m)R(m)\right)\right. \\
& -2\left(NR(L)+\sum_{m=1}^{N-1}(N-m)\left[R(|m-L|)+R(|m+L|)\right]\right) \\
& +2\left(NR^2(0)+2\sum_{m=1}^{N-1}(N-m)R^2(m)\right) \\
& \left.+2\left[2\left(NR(L)+\sum_{m=1}^{N-1}(N-m)\left[R(|m-L|)+R(|m+L|)\right]\right)\right]^2\right\}.
\end{aligned}
\tag{A.10}
$$

This expression can be evaluated using computer simulations since it cannot be simplified further by hand.